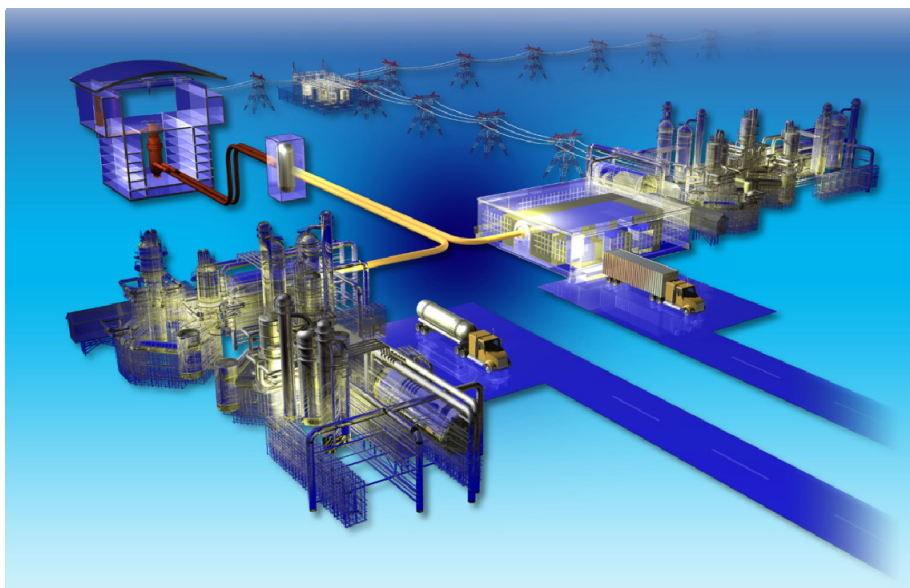


Modeling Degradation in Solid Oxide Electrolysis Cells

Manohar S. Sohal
Anil V. Virkar
Sergey N. Rashkeev
Michael V. Glazoff

September 2010

The INL is a
U.S. Department of Energy
National Laboratory
operated by
Battelle Energy Alliance



DISCLAIMER

This information was prepared as an account of work sponsored by an agency of the U.S. Government. Neither the U.S. Government nor any agency thereof, nor any of their employees, makes any warranty, expressed or implied, or assumes any legal liability or responsibility for the accuracy, completeness, or usefulness, of any information, apparatus, product, or process disclosed, or represents that its use would not infringe privately owned rights. References herein to any specific commercial product, process, or service by trade name, trade mark, manufacturer, or otherwise, does not necessarily constitute or imply its endorsement, recommendation, or favoring by the U.S. Government or any agency thereof. The views and opinions of authors expressed herein do not necessarily state or reflect those of the U.S. Government or any agency thereof.

Modeling Degradation in Solid Oxide Electrolysis Cells

**Manohar S. Sohal
Anil V. Virkar (University of Utah)
Sergey N. Rashkeev
Michael V. Glazoff**

September 2010

**Idaho National Laboratory
Idaho Falls, Idaho 83415**

<http://www.inl.gov>

**Prepared for the
U.S. Department of Energy
Office of Nuclear Energy
Under DOE Idaho Operations Office
Contract DE-AC07-05ID14517**


Next Generation Nuclear Plant

Modeling Degradation in Solid Oxide Electrolysis Cells

INL/EXT-10-19691

September 2010

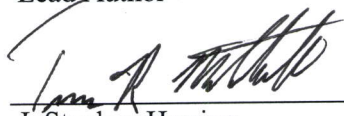
Approved by:



Manohar S. Sohal
Lead Author

Sept. 14, 2010

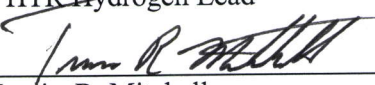
Date

 for J. Stephen Herring

J. Stephen Herring
VHTR Hydrogen Lead

Sept. 14, 2010

Date



Travis R. Mitchell
VHTR TDO Project Manager

Sept. 14, 2010

Date

ABSTRACT

Idaho National Laboratory has an ongoing project to generate hydrogen from steam using solid oxide electrolysis cells (SOECs). To accomplish this, technical and degradation issues associated with the SOECs will need to be addressed. This report covers various approaches being pursued to model degradation issues in SOECs.

An electrochemical model for degradation of SOECs is presented. The model is based on concepts in local thermodynamic equilibrium in systems otherwise in global thermodynamic non-equilibrium. It is shown that electronic conduction through the electrolyte, however small, must be taken into account for determining local oxygen chemical potential, μ_{O_2} , within the electrolyte. The μ_{O_2} within the electrolyte may lie out of bounds in relation to values at the electrodes in the electrolyzer mode. Under certain conditions, high pressures can develop in the electrolyte just near the oxygen electrode/electrolyte interface, leading to oxygen electrode delamination. These predictions are in accordance with the reported literature on the subject. Development of high pressures may be avoided by introducing some electronic conduction in the electrolyte.

By combining equilibrium thermodynamics, non-equilibrium (diffusion) modeling, and first-principles, atomic scale calculations were performed to understand the degradation mechanisms and provide practical recommendations on how to inhibit and/or completely mitigate them.

ACKNOWLEDGEMENTS

This report represents a compilation of the efforts of several researchers at University of Utah and Idaho National Laboratory. It is an edited version of their research. The lead author acknowledges the contribution of these researchers (listed as coauthors of this report).

CONTENTS

ABSTRACT.....	v
ACKNOWLEDGEMENTS.....	vii
ACRONYMS.....	xiii
NOMENCLATURE	xiii
1. INTRODUCTION TO HIGH TEMPERATURE ELECTROLYSIS WITH SOLID OXIDE CELLS.....	1
1.1 Solid Oxide Cell.....	1
2. LOSSES (DEGRADATION) IN A CELL.....	4
2.1 Overview of Polarization Losses	4
2.2 Activation (Charge Transfer) Polarization.....	5
2.3 Concentration (Diffusion) Polarization.....	6
2.4 Ohmic (Resistance) Polarization.....	7
3. NON-EQUILIBRIUM THERMODYNAMICS MODELING OF DEGRADATION IN SOLID OXIDE ELECTROLYSIS CELLS.....	9
3.1 Introduction.....	9
3.1.1 Degradation in SOEC.....	9
3.1.2 Global Nonequilibrium, Local Equilibrium.....	10
3.1.3 Nonequilibrium Thermodynamics, Local Equilibrium and Transport in Predominantly Oxygen Ion Conductors.....	11
3.1.4 Electrochemical Potential of O^{2-} in Predominantly O^{2-} Ion Conductors.....	13
3.1.5 Chemical Potential of Neutral Oxygen and Electric Potential in Predominantly Oxygen Ion Conductors.....	14
3.1.6 True and Apparent Steady States	14
3.2 Analysis of Currents through a Cell.....	15
3.2.1 Ionic and Electronic Currents through the Cell and the Measured Current	15
3.2.2 Equivalent Circuits.....	17
3.2.3 Chemical Potential and Pressure of Oxygen inside the Electrolyte (just near the Electrodes).....	21
3.2.4 Relative Magnitudes of Transport Numbers and the Development of High Oxygen Pressure in the Electrolyte near the Oxygen Electrode	24
3.2.5 Example Calculations	26
3.2.6 SOFC versus SOEC	33
3.2.7 Comparison of the Available Experimental Results from the Literature with the Predictions of the Model	33
3.2.8 Transient Effects	34
3.2.9 Time Required to Attain Steady State and/or the Condition of Criticality	35
3.3 Summary of Thermodynamic Modeling.....	36
4. ATOMIC-SCALE MODELING OF DEGRADATION IN SOLID OXIDE ELECTROLYZED CELLS.....	37
4.1 Introduction.....	37

4.2	Methods of Modeling: Atomic-scale Calculations, Thermodynamics, Phase Equilibria, and Diffusion Modeling	38
4.2.1	First-principles Calculations and Atomic-scale Modeling.....	38
4.2.2	Thermodynamics and Phase Equilibria.....	39
4.2.3	Diffusion Modeling.....	39
4.3	Results.....	40
4.3.1	Diffusion Modeling of Coating for 441 Ferritic Steel to Prevent Electrolyte Cr Poisoning.....	40
4.3.2	Delamination Processes in SOEC	46
5.	MODELING BASED ENGINEERING SOLUTIONS THAT HELP IMPROVE OPERATION OF THE SOECS	51
6.	SUMMARY AND CONCLUSIONS OF ATOMISTIC MODELING.....	54
6.1	Future Work	54
7.	SUMMARY OF DEGRADATION MODELING IN SOEC.....	55
8.	REFERENCES	56

FIGURES

Figure 1.	(a) SOEC; (b) solid oxide fuel cell (SOFC) operating in reverse compared to an SOEC.	2
Figure 2.	Ceramtec solid oxide cell/stack construction; (scanning electron microscopy figure on the right is taken from Reference).	2
Figure 3.	SOFC voltage-current characteristics for a single cell operating at 800°C. ⁶	5
Figure 4.	SEM micrographs from Figure 16 of Mawdsley et al. ¹⁹ showing oxygen electrode delamination along the oxygen electrode/electrolyte interface.	10
Figure 5.	A schematic of a solid oxide electrolyzer cell, when operated in the electrolyzer mode.	16
Figure 6.	An equivalent circuit for the cell in a ‘true’ steady state.	17
Figure 7.	An equivalent circuit for the cell in an ‘apparent’ steady state.	18
Figure 8.	A schematic plot of the measured voltage (which is also the applied voltage, E_A) vs. the measured current density.	20
Figure 9.	Schematic variations of electric potential (ϕ) and oxygen chemical potential (μ_{O_2}) through the electrolyte in the fuel cell mode (true steady state).	23
Figure 10.	Schematic variations of electric potential (ϕ) and oxygen chemical potential (μ_{O_2}) through the electrolyte in the electrolyzer mode.	24
Figure 11.	A schematic variation of oxygen chemical potential in the vicinity of the oxygen electrode/electrolyte interface when high oxygen pressure is developed within the electrolyte.	31
Figure 12.	A schematic showing the locations where the high oxygen pressure builds up. Delamination cracks develop at multiple places and then link up to form a macroscopic delamination crack along the oxygen electrode/electrolyte interface.	32

Figure 13. Chemical composition of 441 stainless steel (left) and tensile strength for rupture in 1000 hours as a function of temperature for different types of steels (right). ⁶⁴	41
Figure 14. Single equilibrium calculations for Ferritic steel 441 at 1073°F (800°C).	41
Figure 15. Mass-fractions of equilibrium phases in steel 441 as a function of temperature.	42
Figure 16. Carbon-isopleths for stainless steel 441, confirming that the equilibrium phase composition of 441 steel at 800°C is body centered cubic (bcc)-matrix, face-centered cubic (fcc)-strengthening precipitates, and a small amount of the Laves phase.	42
Figure 17. Chromium isopleths for steel 441, confirming the results shown in Figures 15 and 16.	43
Figure 18. Concentration profile of Cr computed across the 441/Ni interface.	43
Figure 19. Relaxed structure for a large periodic Ni-Cr-Fe supercell obtained from self-consistent density-functional theory calculations. A Ni (fcc) slab is positioned on top of a Fe (bcc) slab, and a Cr monolayer is located at the Ni-Fe interface.	44
Figure 20. SEM/energy dispersive x-ray spectroscopy (EDS) analysis on E-brite stainless steel (with a relatively high Cr concentration of 27 wt%) with $Mn_{1.5}Co_{1.5}O_4$ protection layer after the contact ASR measurement between the cathode ((La,Sr)CrO ₃) and the interconnect at 800°C in air for about 400 h: (a) SEM cross-section and (b) EDS line scan along line A–A in (a). The E-brite coupon spray-coated with spinel precursor was heat-treated in Ar + 2.75% H ₂ + 3% H ₂ O for 4 h prior to the measurement. ⁶⁹	45
Figure 21. Schematics of the Cr migration mechanism across the interface between $MnCo_2O_4$ spinel (cubic structure) and Cr ₂ O ₃ oxide (hexagonal structure). Co atoms are shown in brown, O in red, Mn in purple, Cr in blue.	45
Figure 22. (a) Bright-field temperature electron microscopy image of the SOFC cathode/electrolyte interface, where LSM grains are in contact with the YSZ electrolyte, and (b) EFTEM image combining Zr, Mn, and La map of the same area as in (a). ⁷⁴	46
Figure 23. SEM image of the electrode (LSM) and electrolyte (YSZ) interface.	47
Figure 24. Atomic-scale models for LSM-YSZ interface: a free YSZ surface (top), a smooth LSM-YSZ interface (bottom). Both interfaces have the (001) orientation. Oxygen atoms are shown in red, Zr in small light blue balls, La in big cyan balls, and Mn in purple.	47
Figure 25. Schematics for substitutional Mn, Sr, and La impurity defects in subsurface area of YSZ near the LSM-YSZ interface. Sr atoms are shown in green.	48
Figure 26. Equilibrium pressure of O ₂ gas on top of the YSZ electrolyte at $T = 800^\circ\text{C}$ as a function of O ₂ formation energy; black points correspond to different impurities positioned in the YSZ subsurface region below the surface (left). Schematics of the formation of peroxy O-O bonds at the surface (precursors of O ₂ molecules) caused by substitutional Mn impurities in the subsurface region (right).	49
Figure 27. The cerium-oxygen phase diagram.	52
Figure 28. EDX-line scans of zirconia-ceria-fracture interface of 4-micron-thick CGO barrier layer sample. The origin of the x-axis is located at the zirconia-ceria interface, which is defined as the location where the amount of Zr equals Ce. ⁷⁷	52
Figure 29. Schematics of substitutional La defect on top of CeO ₂ surface. Ce atoms are shown in gray, O in red, and La in blue.	53

TABLES

Table 1. Commonly used materials in SOFC/SOEC. ³	3
Table 2. Estimation of oxygen pressure within the electrolyte just near the oxygen electrode (anode)/electrolyte interface, $p_{O_2}^a$, for various values of cell area specific electronic resistance, R_e . The applied voltage is $E_A = 1.5$ V.....	29

ACRONYMS

ASR	area-specific resistance
CGO	cerium-gadolinium oxide
EDS	energy dispersive x-ray spectroscopy
GUESS	Gaussians Used for Embedded System Studies
GDC	gadolinia-doped ceria
INL	Idaho National Laboratory
KMC	Kinetic Monte Carlo
LSCF	lanthanum strontium cobalt iron oxide ($\text{La}(\text{Co,Fe})\text{O}_3$)
LSF	strontium-doped lanthanum ferrite
LSM	strontium-doped lanthanum manganite (LaMnO_3)
MD	molecular dynamics
Ni-YSZ	nickel-yttria stabilized zirconia
SEM	scanning electron microscopy
SOEC	solid oxide electrolysis cell
SOFC	solid oxide fuel cell
TEM	transmission electron microscopy
TPB	triple-phase boundary
VASP	Vienna Atomic Simulation Program
YSZ	yttria-stabilized zirconia

NOMENCLATURE

r_i^c	Area specific ionic charge transfer (polarization) resistance at the cathode (steam- H_2 electrode)/electrolyte interface (Ωcm^2)
r_i^a	Area specific ionic charge transfer (polarization) resistance at the anode (oxygen electrode)/electrolyte interface (Ωcm^2)
r_e^c	Area specific electronic charge transfer (direct electron transfer) resistance at the cathode (steam- H_2 electrode)/electrolyte interface (Ωcm^2)
r_e^a	Area specific electronic charge transfer (direct electron transfer) resistance at the anode (oxygen electrode)/electrolyte interface (Ωcm^2)
r_i^{el}	Area specific ionic resistance of the electrolyte (Ωcm^2)
r_e^{el}	Area specific electronic resistance of the electrolyte (Ωcm^2)

$R_i = r_i^c + r_i^{el} + r_i^a$	Area specific ionic resistance of the cell (Ωcm^2)
$R_e = r_e^c + r_e^{el} + r_e^a$	Area specific electronic resistance of the cell (Ωcm^2)
$j_{O^{2-}}$	Flux of oxygen ions ($\text{molcm}^{-2}\text{s}^{-1}$)
j_e	Flux of electrons ($\text{molcm}^{-2}\text{s}^{-1}$)
$I_{O^{2-}}(\vec{r}, t)$	Oxygen ion current density as a function of position and time (Acm^{-2})
$I_i = I_{O^{2-}}$	Ionic (oxygen) current density (Acm^{-2})
I_e	Electronic current density (Acm^{-2})
I	Load current (density) (Acm^{-2})
\vec{r}	Position vector (cm)
t	Time (s)
$t_i = \frac{R_e}{(R_i + R_e)}$	Ionic transport number of the cell including interfaces
F	Faraday constant (Cmol^{-1})
R	Gas constant ($\text{Jdeg}^{-1}\text{mol}^{-1}$)
T	Temperature (deg Kelvin)
E_N	Nernst voltage (V)
$E^a = \frac{(\mu_{O_2}^{Ox} - \mu_{O_2}^a)}{4F}$	Nernst potential across electrolyte/oxygen electrode interface (V)
$E^{el} = \frac{(\mu_{O_2}^a - \mu_{O_2}^c)}{4F}$	Nernst potential across the electrolyte (excluding interfaces) (V)
$E^c = \frac{(\mu_{O_2}^c - \mu_{O_2}^{St-H_2})}{4F}$	Nernst potential across electrolyte/steam-H ₂ electrode (V)
E_A	Applied voltage (V)
$p_{O_2}^{St-H_2}$	Oxygen partial pressure in the gas phase at the steam-H ₂ electrode (atm. or Pa)
$p_{O_2}^{Ox}$	Oxygen partial pressure in the gas phase at the oxygen electrode (atm. or Pa)
$p_{O_2}^a$	Oxygen pressure in the electrolyte just near the oxygen electrode (anode)/electrolyte interface (atm. or Pa)

$p_{O_2}^c$	Oxygen pressure in the electrolyte just near the steam-H ₂ electrode (cathode)/electrolyte interface (atm. or Pa)
z_i	Valence of species i .
μ_i	Chemical potential of species i (Jmol ⁻¹)
$\mu_{O_2}^{Ox}$	Chemical potential of oxygen at the oxygen electrode (gas phase) (Jmol ⁻¹)
$\mu_{O_2}^{St-H_2}$	Chemical potential of oxygen at the steam-H ₂ electrode (gas phase) (Jmol ⁻¹)
$\mu_{O_2}^a$	Chemical potential of oxygen in the electrolyte near the oxygen electrode/electrolyte interface (Jmol ⁻¹)
$\mu_{O_2}^c$	Chemical potential of oxygen in the electrolyte near the steam-H ₂ electrode/electrolyte interface (Jmol ⁻¹)
$\tilde{\mu}_i$	Electrochemical potential of species i (Jmol ⁻¹)
$\sigma_{O^{2-}}$	Oxygen ion conductivity (Scm ⁻¹)
σ_e	Electronic conductivity (Scm ⁻¹)
Φ	Electrostatic potential (V)
$\varphi = -\frac{\tilde{\mu}_e}{F} = -\frac{\mu_e}{F} + \Phi$	Electric potential (reduced negative electrochemical potential of electrons) (V)

Modeling Degradation in Solid Oxide Electrolysis Cells

1. INTRODUCTION TO HIGH TEMPERATURE ELECTROLYSIS WITH SOLID OXIDE CELLS

Idaho National Laboratory (INL) is performing high temperature electrolysis research to generate hydrogen using solid oxide electrolysis cells (SOECs). This concept produces hydrogen using the heat and electricity generated by a high temperature nuclear reactor. The $\sim 900^{\circ}\text{C}$ primary helium coolant uses about 85% of the thermal energy output of the reactor to drive a gas-turbine Brayton power cycle, which provides the electrical energy required for the high temperature electrolysis process. The remaining 20% of the reactor thermal energy is used to generate steam at about 850°C . The combination of a high-efficiency power cycle and the direct utilization of nuclear process heat yields a high overall thermal-to-hydrogen conversion efficiency of 50% or higher.

The objective of the project is to address the technical and scale-up issues associated with the implementation of SOEC technology for hydrogen production from steam. The project includes a broad range of activities, including small bench-scale experiments to study SOEC degradation, computational fluid dynamic modeling, and system modeling. Some of the issues related to solid oxide cells include identification and evaluation of cell performance degradation parameters and processes, cell degradation modeling, integrity, and reliability of the SOEC stacks.

A mixture of steam and hydrogen is fed to the electrolytic cells where the oxygen migrates through the solid-state electrolyte as O^{\ominus} ions because of the imposed voltage. The cell voltage is about 0.3 V lower than that required in conventional electrolyzers because of the high operating temperature. In addition, electrolytic reaction kinetics are much faster than in room-temperature electrolyzers, thus avoiding polarization losses. The mixture exiting the cells, about 25 vol% steam and 75 vol% hydrogen, enters a separator where the two components are separated either by condensation of the steam or diffusion of the hydrogen. A fraction of the produced hydrogen is recycled and mixed with additional steam and some of the hydrogen is mixed with additional steam to achieve the required inlet mixture composition. It is then reheated and returned to the solid oxide cells. The remaining steam can be removed from the hydrogen product stream through condensation. Like the hydrogen stream, the oxygen stream exiting the cells has a temperature of about 830°C , which can be effectively used as needed.

1.1 Solid Oxide Cell

A solid oxide cell is a key component of the electrolysis system. It consists of three main components: an electrolyte and two electrodes (Figure 1 and Figure 2). The electrolyte is a ceramic membrane that can conduct ions and is sandwiched between two porous electrodes that can conduct electrons: the steam/hydrogen electrode (or anode in fuel cell mode) and the air/oxygen electrode (or cathode in the fuel cell mode). In the fuel cell mode, oxygen molecules dissociate at the oxygen electrode and combine with electrons coming from external electric power source to form oxygen ions. The oxygen ions conduct through the electrolyte and migrate towards the hydrogen electrode. The fuel (hydrogen or natural gas) is fed to the anode and reacts with the oxygen ions to form water and CO_2 . If the fuel cell is operated in the electrolysis mode, the names and function of the electrode get reversed as shown in Figure 1.

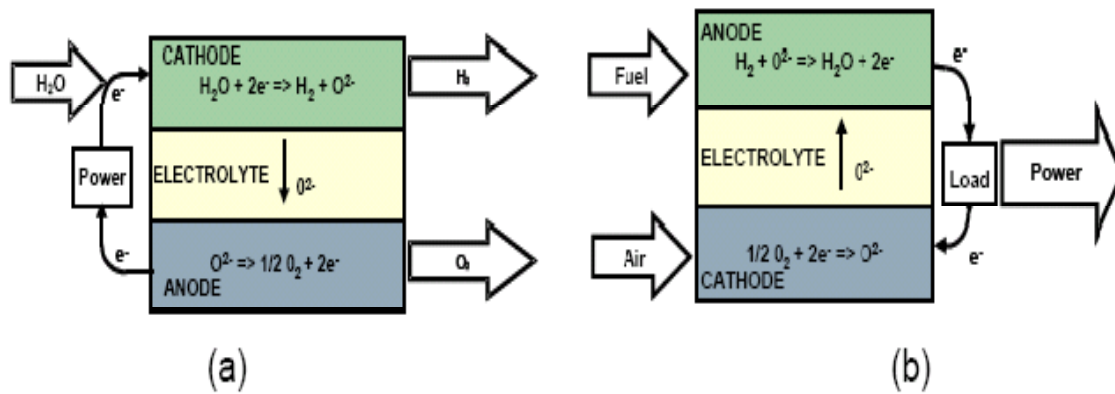


Figure 1. (a) SOEC; (b) solid oxide fuel cell (SOFC) operating in reverse compared to an SOEC.¹

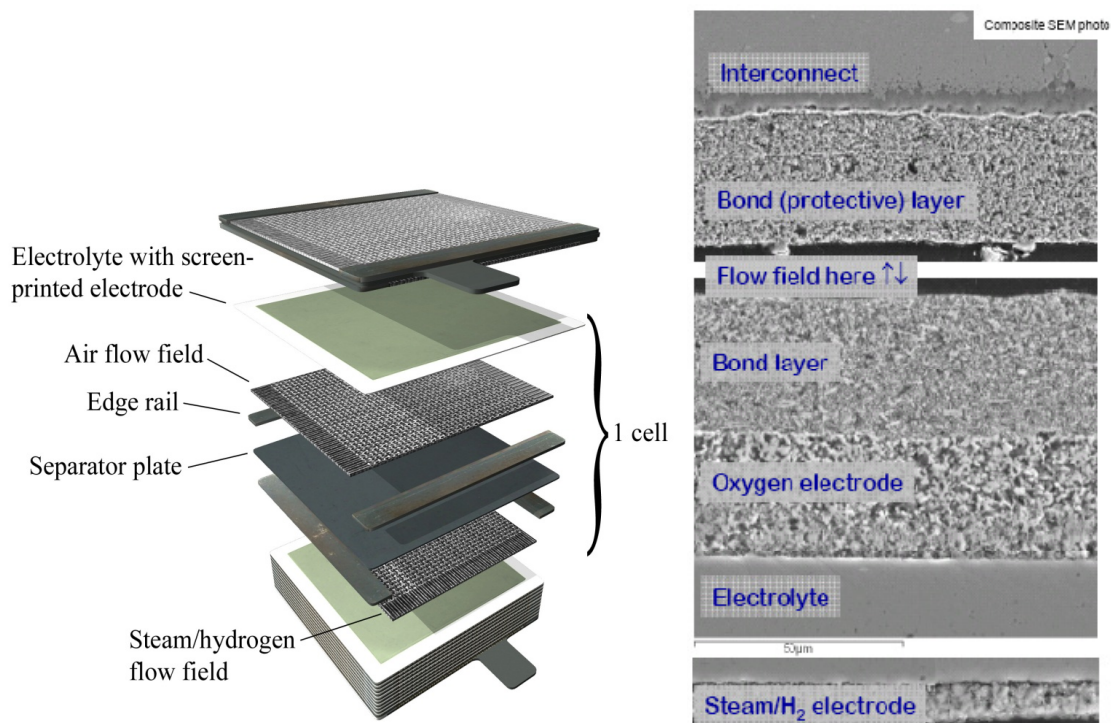


Figure 2. Ceramtec solid oxide cell/stack construction; (scanning electron microscopy figure on the right is taken from Reference 2).

The most common materials currently used for the solid oxide cells are listed in Table 1.³ The electrolyte is a dense gas-tight ceramic layer, usually made from yttria-stabilized zirconia (YSZ) with yttria content of 8 mol% to fully stabilize the electrolyte composition. The performance of the electrolyte depends on how well it can conduct oxide ions (O^{2-}). The thinner the electrolyte, the higher its ion conductivity and the lower the cell's ohmic resistance. In an electrolyte supported cell, the electrolyte thickness is large (150–250 μm), which leads to relatively high ionic resistance. Therefore, if the mechanical strength can be provided by the steam/ H_2 electrode, the electrolyte thickness can be reduced by a factor of 10 or so.

Table 1. Commonly used materials in SOFC/SOEC.³

Component	Material	Acronym
Steam/hydrogen electrode	Ni - Y _x Zr _{1-x} O _{2-x/2} (nickel-YSZ)	Ni-YSZ
Electrolyte	Y _x Zr _{1-x} O _{2-x/2} (YSZ)	YSZ
Air/oxygen electrode	Sr _x La _{1-x} MnO _{3-δ} + Y _x Zr _{1-x} O _{2-x/2} (doped lanthanum manganite)	LSM-YSZ
Interconnect	Chromium based alloys/ceramics or stainless steel	SS

The most common anode material for SOFC is a porous cermet (**ceramic-metal**) made from Ni and YSZ. Electronically-conductive, gas-tight interconnect plates connect the individual cells to form a stack. The ionic conductivity of ceramics is highly dependent on the ceramic temperature. Thus, high operating temperatures are required to obtain sufficient overall conductivity in the solid oxide cell. YSZ exhibits acceptable conductivity in the 700–1,100°C temperature range, but if thermal cycling occurs, such as at start-up, the high operating temperature results in large thermal stresses in the cell components. Stresses can also be caused by large thermal gradients generated by the uneven distribution of electrochemical reaction sites. Finally, fabrication of the cell components also requires high temperatures that can cause detrimental residual stresses within the cell components. Guan et al.¹ performed studies for reversible solid oxide cells that were tested in both fuel cell and electrolysis modes. They selected YSZ (8 mol% Y₂O₃ doped zirconia) as electrolyte material. Selected oxygen electrodes were strontium-doped lanthanum manganite (LSM), strontium-doped lanthanum ferrite (LSF), and lanthanum strontium cobalt iron oxide (LSCF). They used samaria-doped ceria (interlayer for LSF and LSCF). LSCFs have increased ionic conductivity and may reduce degradation rate in electrolysis mode. For hydrogen electrode, Ni-YSZ was selected with varying volume fraction of Ni (40–80%).

In the fuel cell mode, the oxygen electrode is fed with air while the hydrogen electrode is fed with hydrogen or natural gas. Thus, the properties of the oxygen electrode should be such that it provides a component for oxygen gas to be easily reduced and similarly, the function of the hydrogen electrode is to oxidize the fuel gas. At the oxygen electrode, where electrons are supplied via the external electrical power, oxygen molecules are reduced to oxygen ions. The oxygen ions are conducted through the electrolyte to the hydrogen electrode. At the hydrogen electrode, oxygen ions oxidize the fuel gas which forms water and carbon dioxide, while the resulting free electrons are transported via the external circuit back to the oxygen electrode. The solid oxide electrolyte separates the reduction and oxidation reactions. Thus, in the electrolysis mode, the electrical energy is used to split hydrogen from steam. The electrolysis process is the reverse of the fuel cell process.

2. LOSSES (DEGRADATION) IN A CELL

2.1 Overview of Polarization Losses

The polarization losses/degradation definitions described in this chapter are strictly written for a SOFC. Appropriate care should be applied when applying the same fundamentals for a SOEC.

When a fuel cell is not connected to an external load, there is no current flow and the maximum reversible cell voltage or open circuit voltage can be calculated by the equilibrium Nernst potential, V_{Nerst} , for the specific electrochemical reaction system. The, V_{Nerst} is calculated using the partial pressure of the chemical species at the cell inlet or outlet. However, it is more appropriate to calculate an average of the inlet and outlet values, V_{Nerst}^i and V_{Nerst}^o , where superscripts i and o represent inlet and outlet locations as shown in the following equations:

$$V_{Nerst} = \frac{1}{2} (V_{Nerst}^i + V_{Nerst}^o) \quad (2-1)$$

$$V_{Nerst}^i = -\frac{\Delta G^0}{n_e F} - \frac{RT}{n_e F} \ln \left(\frac{p_{H_2O}^i}{p_{H_2}^i \sqrt{p_{O_2}^i}} \right) \quad (2-2)$$

$$V_{Nerst}^o = -\frac{\Delta G^0}{n_e F} - \frac{RT}{n_e F} \ln \left(\frac{p_{H_2O}^o}{p_{H_2}^o \sqrt{p_{O_2}^o}} \right) \quad (2-3)$$

where ΔG^0 is the change in Gibbs free energy at standard conditions and equals $-RT \ln[K(T)]$, R is the universal gas constant, T is the cell temperature, K is the equilibrium constant, n_e is the number of electrons participating in the electrochemical reaction, F is the Faraday's constant, and p is the partial pressure of respective species.

When a fuel cell starts supplying electric current to an external load, its operating voltage drops because of irreversibilities associated with internal resistances. The difference between the maximum reversible cell voltage or open circuit voltage (V_{OCV}) and the operating cell voltage (V_{open}) is termed polarization loss (η). Cell performance depends on the overall cell reaction and the type of reactants at the electrodes and the reaction product(s). A detailed description of polarization losses is given by Ivers-Tiffée and Virkar⁴ and Akkaya.⁵ The total polarization loss of an operating cell consists of three dominant parts: activation (or charge transfer) polarization (η_{act}), concentration (or diffusion) polarization which includes chemical reaction polarization (η_{conc}), and ohmic resistance polarization (η_{ohm}) as in

$$\eta = \eta_{act} + \eta_{conc} + \eta_{ohm} \quad (2-4)$$

The current efficiency can be stated as the percent of current passing through an electrolytic cell (or electrode) that accomplishes the desired chemical reaction compared to the ideal case. For example, in the hydrogen fuel cell, ideally every hydrogen (H_2) molecule would react to produce two electrons that would contribute to the current flow. The inefficiencies arise from reactions other than the intended one taking place at the electrodes, or the side reactions consuming the current. Some hydrogen for instance, may go through the electrolyte and not react at all, or the hydrogen does react but the resulting current is driven through the electrolyte (not the electrode) and never contributes to the current flow.

The voltage efficiency is defined as the net voltage (cell equilibrium voltage minus the irreversible losses) divided by the maximum voltage. The irreversible voltage losses are attributed to polarization losses that primarily originate from three sources: activation, concentration, and ohmic polarizations.

Thus, the net cell voltage is the open circuit voltage, minus the various polarization losses, and can be written as

$$V_{\text{cell}} = V_{\text{open}} - (V_{\text{act}} + V_{\text{conc}} + V_{\text{ohm}}) = V_{\text{Nernst}} - V_{\text{loss}}. \quad (2-5)$$

Figure 3, developed by Windisch et al.,⁶ shows the relative magnitude of various polarization losses in a SOFC. It shows that activation losses are the dominant mode of three types of polarization losses. It also shows the upper limit of current density for the fuel cell to operate.

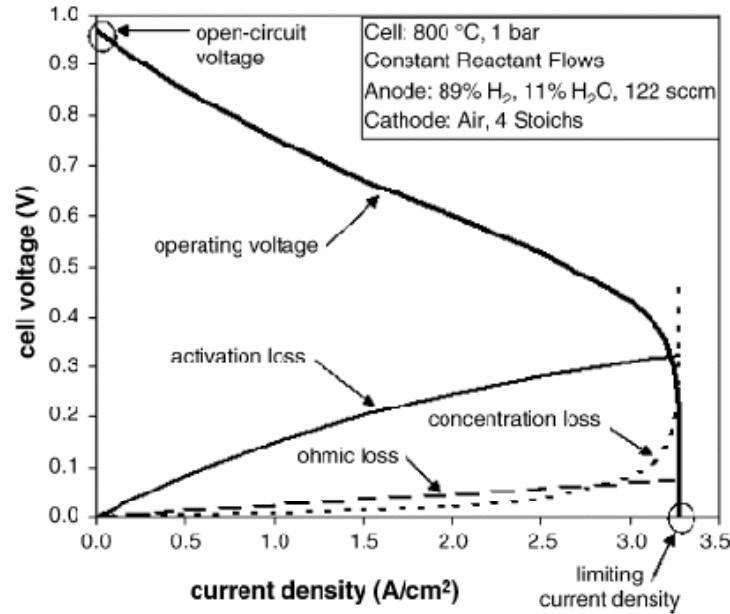


Figure 3. SOFC voltage-current characteristics for a single cell operating at 800°C.⁶

The overpotentials can be determined by the several models available in the literature, for example Virkar.⁷ However, the concentration overpotentials are different between the SOEC and SOFC modes because of the different gas transport mechanisms in the porous electrodes. Ni et al.⁸ showed that concentration overpotentials are the sole factor responsible for the different current–voltage (i–V) characteristics between the SOEC and SOFC modes. Their analytical model shows the difference between SOECs and SOFCs to be the differences in the gas transport mechanisms of the two different modes. The selection of an electrode support can greatly affect the overall performance of a reversible solid oxide cell. A hydrogen-electrode (fuel cell anode) support is favorable to the SOFC mode while an oxygen-electrode (electrolysis anode) support is favorable to the SOEC mode. Therefore, the details of both SOEC and SOFC operating conditions should be carefully considered in their design. If a specified solid oxide cell is mainly used for hydrogen generation, an oxygen-electrode (electrolysis anode) supported cell is recommended.

2.2 Activation (Charge Transfer) Polarization

Electrochemical reactions at the electrodes involve charge transfer, by which a neutral species is converted into an ion or an ion is converted into a neutral species. The electrodes may conduct either electrons or ions or both. Losses incurred during ionic and electronic transfer are sometimes called activation losses. The electrode reaction rate is a function of operating conditions and electrode materials. The reactions can result in adsorption, electron transfer, or desorption. The activation energy can be reduced by the presence of a catalyst. The activation polarization is nonlinear, dominant at low current

density, and related to a physical or electrical barrier at the electrolyte-electrode interfaces. At the anode and the cathode (in a fuel cell mode), the reactants diffuse to the reaction sites where the activation polarization must be overcome before the reduction and oxidation reactions take place. The activation potential is generally the largest of the three polarizations at low and medium temperatures. Catalysts are often used to overcome the activation potential and enable the reaction to proceed faster. At higher temperatures ($>800^{\circ}\text{C}$) in fuel cells, the activation potential is lower and generally does not need a catalyst. The charge double layer is caused by the accumulation of ions and electrons on or near an electrode-electrolyte interface. This layer stores energy like a capacitor, which is often considered to be one reason for the occurrence of the activation polarization.

The activation polarization is estimated by the Tafel equation, which shows a straight line relationship between over-potential and the log of current density. The current density or exchange current density is the flow of electrons to and from the electrolyte. Semi-empirical correlations are used to calculate polarization. However, their accuracy is questionable over a wide range of operating conditions. The Butler-Volmer (B-V) equation is therefore used to calculate current density as

$$i = i_0 \left[\exp\left(\frac{\beta n_e F V_{act}}{RT}\right) - \exp\left(\frac{(1-\beta) n_e F V_{act}}{RT}\right) \right] \quad (2-6)$$

where i is current density, i_0 is the exchange current density, and β is transfer coefficient. The exchange current density, i_0 , is the forward and reverse electrode reaction rate at equilibrium potential. The transfer coefficient, β , is defined as the fraction of activation polarization that affects the activation energy barrier and thus the rate of electrochemical transformation. It is assumed to be ~ 0.5 for fuel cell mode, but values in the range 0.3–0.6 have been used to match the experimental data. The exchange current density depends on cell materials, construction, and operating temperature, but in many studies it is taken to be a constant. Noren and Hoffman⁹ have given two approximations to solve the B-V equation. When the activation loss is large (>200 mV), the first term in the B-V Equation 2-6 is much larger than the second one, which can then be neglected. The simplified equation is the high-field approximation called Tafel equation, and is valid for $i/i_0 > 4$. For $i/i_0 < 1$, higher order nonlinear terms are neglected and a low-field approximation, also called linear current-potential equation, is achieved. Considering the shape of the B-V equation (hyperbolic sine function) and considering the reduction charge transfer coefficient to be equal to the oxidation charge transfer coefficient (for both cathode and anode), the activation loss can be calculated as

$$V_{act} \cong \frac{RT}{\alpha_1 F} \sinh^{-1} \left(\frac{i}{2i_0} \right) \quad (2-7)$$

Noren and Hoffman⁹ have shown that the B-V equation and hyperbolic sine approximation are nearly identical and match well with experimental data obtained by Pacific Northwest National Laboratory. It is critical for this current density to be as high as possible because it is easier to keep a process going than to start it from scratch. Many methods are known and others are being investigated that can reduce activation polarization, such as raising cell temperature, doping the electrode with effective catalysts, increasing the surface area of the electrode by making it rougher, increasing reactant concentration, and increasing the pressure.

2.3 Concentration (Diffusion) Polarization

When the electrode reactions are not supplied with sufficient reactants or the reaction products do not move away fast enough, the loss in cell performance is called concentration polarization. A reduced supply of reactants will slow down the reaction. Chemical reaction polarization has the same effect as

concentration polarization, but is the result of limiting reactions for producing or removing reactants or products. The diffusion loss and the chemical reaction loss are sometimes collectively called mass transport polarization.

The concentration polarization dominates at high current density. It is related to diffusion of reactants and products, and is often referred to as a mass transport loss because the reduction of reactant concentration is the result of a failure to transport sufficient reactant to the electrode surface. For higher current density, the flow rate of reactants required for the electrochemical reactions should also increase. Eventually, the rate of ionic transport through the cell cannot keep up with the rate at which the reactants are consumed. The concentration of reactants at the reaction sites begins to drop and thus, the voltage drops. At the oxygen electrode, as oxygen is being used (typically from an air supply), a reduction in the concentration of oxygen in the region of the electrode occurs. This change in concentration causes a drop in the partial pressure of the oxygen; the magnitude of the drop depends on the current flow in the fuel cell. Other factors of the pressure drop are the physical characteristics of the fuel cell, such as how well the air supply circulates to replenish the oxygen. Similarly, a drop in gas pressure occurs at the steam/hydrogen electrode as hydrogen is used and current is generated. As with the cathode, the rate of this drop will depend on the characteristics of the fuel cell, such as the gas supply system. The gas supply system will consist of cell flow channels and fluid resistance, which will impact flow distribution.

The following equation for concentration loss can be developed by considering that at an electrode, fuel gas pressure change results in voltage drop:

$$\eta_{\text{conc}} = \frac{RT}{nF} \ln(P_2/P_1) \quad (2-8)$$

where R is gas constant, T is temperature, F is Faraday's constant, n is the number of electrons involved in the transfer, P_1 is pressure when the current density is zero, and P_2 is pressure at any current density.

This equation can be transformed into another useful relationship by considering that the current density of the fuel cell will be constrained by how fast the fuel can be supplied to the electrode. If i_L is the limiting current density that corresponds to this maximum rate of fuel usage, and assuming that the pressure will fall linearly down to zero at the current density i , then pressure P_2 , at any current density i , would be $P_2 = P_1 (1 - i/i_L)$. By substituting this relation into Equation 2-8, the result is Nernst equation.

$$\Delta V = - \frac{RT}{nF} \ln (1 - i/i_L) \quad (2-9)$$

Equation 2-9 gives voltage change caused by mass transport losses, (a negative sign indicates a voltage drop in a SOFC mode). The mass transport voltage drop for the entire cell at either of the electrodes at the current density (i) can reach the limiting current density (i_L) causing the entire cell voltage to drop to zero. For this statement to be true, the actual value of the term denoted as “ RT/nF ” (which will vary with different fuel cell reactants) must be larger than the theoretical value.

2.4 Ohmic (Resistance) Polarization

Ohmic (resistance) polarization is caused by the electrical resistance encountered in transportation of ions and electrons through the electrolyte, electrodes, and current collectors. Ohmic (resistance) polarization should be separated from other polarization phenomena. When current flows through a cell, the resulting drop in voltage from the open circuit voltage (V_{open}) is defined as the cell polarization or overpotential at the specific current density.

Unlike the activation and concentration polarization, the ohmic polarization is a linear function of the cell current and increases over the entire range of current. The ohmic polarization refers to the voltage drop caused by the resistance to the flow of electrons and ions through the cell, which is fairly constant in a given cell. Typically, the ohmic polarization is caused by the electrolyte, the cell interconnectors, or bipolar plates. In the equation $V_{\text{ohm}} = i * r$, the current is often expressed as current density (amps per unit

area, such as mA/cm²). Therefore, corresponding resistance of a SOFC is the cell resistance normalized by its area (kΩ·cm²), and is called area-specific resistance (ASR). From the cell polarization and corresponding current density, an ASR can be defined as

$$\text{ASR} = (E - V)/i \quad (2-10)$$

where E can be either open circuit voltage potential (E_{OCV}) or the ideal Nernst potential (E_{N}), depending on whether one wants to (a) remove loss effects because of reactant leakage and variable reactant mixture supply and if one is focused on the cell material performance, or (2) focus on total cell performance (cell material and seals).¹⁰ The important factor to remember about various polarization components is that they are not independent of each other.

3. NON-EQUILIBRIUM THERMODYNAMICS MODELING OF DEGRADATION IN SOLID OXIDE ELECTROLYSIS CELLS

(A. V. Virkar, University of Utah)

There are not many studies in the published literature addressing degradation and related issues in SOECs. As thinner electrolytes with higher ionic conductivity are developed, the overall cell polarization losses are dominated by the electrochemical losses at the electrodes. Even though the solid oxide cells have several differences while operating in power generating (fuel cell) and electrolysis modes, the degradation mechanisms in the two cases may have some similarities. Therefore, the knowledge of degradation mechanisms in SOFCs is being used to model the degradation in the SOECs.

Recently, Virkar⁷ developed an over-potential model for a typical planar SOFC stack comprising several cells connected in series. He also gave the following argument in favor of developing a fundamental understanding of the degradation. In a stack, cell-to-cell characteristics should be as uniform as possible so that, at a given operating current, the voltage across each cell is essentially the same. If, because of some structural/fabrication flaws, the cells are not identical, the resistance and voltage drop will vary from cell-to-cell. In such a case, the remainder of the cells in the stack will drive the cell with higher resistance. In an extreme case, for the stack to continue operating, the voltage across a cell with higher resistance can even become negative, which can eventually lead to cell failure and increased local temperatures. This phenomenon can spread to adjacent cells as a domino effect. However, interpretation solely based on visual observations, without a sound theoretical basis for all the phenomena occurring in a cell, may be misleading. In a cell, observations are the aftermath result of some other critical damage to the cell that has already taken place. So the visual observation alone may not be able to show the “root cause” of the problem. Some of the likely reasons of cell degradation include small initial compositional inhomogeneities resulting in large changes in properties, the formation of local hot spots leading to local changes in microstructures and material properties, electrode delamination caused by thermal cycling/rapid heating, reaction between electrode and electrolyte forming a high resistance layer, fuel and/or oxidant maldistribution, nonuniform oxidation of the interconnect, degradation of the seals, etc. In a normal SOFC, the (oxygen) ionic current is in a direction opposite to that of electronic current. However, if a cell has degraded to cause negative voltage, the direction of electron flow will reverse and both ionic and electronic currents will flow in the same direction. Virkar⁷ has developed a degradation model based on the premise that a cell with higher resistance compared to the rest of the cells in the stack and operating under a negative voltage will be prone to degradation. Planar stacks are more likely to undergo such a degradation mechanism than tubular stacks. Therefore, the ability to measure voltage across each (planar) cell could help in preventing catastrophic failure by either performing preventive maintenance or shorting the bad cell. A similar degradation model of a SOEC can also offer some insight into the cell degradation phenomenon during the electrolysis mode. Thus, the main objective of this work is to propose a fundamental mechanism of degradation of SOEC, which explains the observed delamination of the oxygen electrode.

3.1 Introduction

3.1.1 Degradation in SOEC

Considerable work has been reported on the use of SOEC for electrolysis of H₂O for hydrogen generation.^{1,11,12,13,14,15,16,17,18,19,20,21,22,23,24,25,26} Typical SOEC consists of an oxygen ion conducting a solid electrolyte such as YSZ sandwiched between two electrodes; steam-H₂ electrode (which is the cathode in SOEC) made typically of nickel + YSZ oxygen electrode (which is the anode in SOEC) made typically of an electron (hole) conducting perovskite such as Sr-doped LaMnO₃ (LSM) mixed with YSZ. The cell is typically operated over a temperature range from 800 to 900°C. Water vapor containing a sufficient

amount of hydrogen to prevent oxidation of Ni is circulated past the steam-H₂ electrode. Externally applied DC voltage greater than the decomposition potential of H₂O is applied across the cell such that H₂O is decomposed at the steam-H₂ electrode forming hydrogen with oxygen transported (as ions) through the electrolyte towards the oxygen electrode and electrons transporting in the external circuit. The viability of SOEC for hydrogen generation as a practical system, however, has not been demonstrated in long-term testing since SOEC cells do degrade over time, and it is known that the degradation rate is typically greater than SOFCs, which often are identical (or similar) cells but operated in the power generation mode. One mode of failure in SOECs, has been reported to be the occurrence of delamination of the oxygen electrode.^{1,16,17,18,19} As an example of the morphology of oxygen electrode delamination in SOEC, Figure 4 shows a scanning electron microscope (SEM) micrograph of a delaminated oxygen electrode.

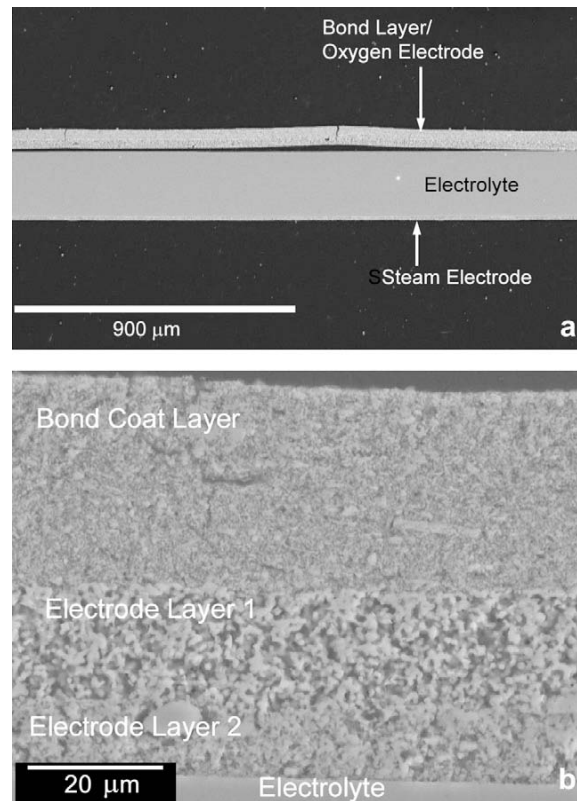


Figure 4. SEM micrographs from Figure 16 of Mawdsley et al.¹⁹ showing oxygen electrode delamination along the oxygen electrode/electrolyte interface.

3.1.2 Global Nonequilibrium, Local Equilibrium

The mechanism is based on the very fundamentals of non-equilibrium thermodynamics and transport theory. The approach used in this manuscript is similar to the one used previously by the author for studies on transport through predominantly ionic conductors and degradation of solid oxide fuel cell stacks.^{7,27} The approach is based on the incorporation of the local equilibrium criterion into the transport equations.^{7,27,28} Much of the work on transport is based on linear, no equilibrium thermodynamics. All reported work on transport through solid electrolytes and mixed ionic electronic conductors is based on either explicit or implicit assumption of local equilibrium, even though the implications of this very important assumption are rarely addressed. Recent non-equilibrium molecular dynamics simulations in several systems have shown that local equilibrium applies to a vast majority of the systems that are in global thermodynamic non-equilibrium.^{29,30,31} An important consequence of the existence of local

equilibrium in solid electrolytes is that electronic conduction cannot be assumed to be identically zero, even in a predominantly ionic conductor.²⁷ This is a subtle but very important point. Yet in many studies, contradictory assumptions of the simultaneous existence of local equilibrium (often tacitly made or even apparently unknowingly made) and purely ionic conduction (no electronic transport) are made.³²

In studies in the general area of non-equilibrium thermodynamics, the concept of local equilibrium has been the cornerstone of many advances and has been extensively discussed in the literature. The general conclusion of this enormous body of work on non-equilibrium thermodynamics is that local equilibrium is almost always valid, even in cases involving nonlinear, non-equilibrium thermodynamics. In fact, the few (possible) cases in which local equilibrium may be violated are very rare and not encountered in cases involving transport of matter by diffusion. Thus, insofar as transport is concerned, there appear to be no reported cases in which local equilibrium is violated. A possible violation of local equilibrium is synonymous with inability to uniquely assign a temperature to a point in the system.²⁸ The rapidity in which local equilibrium is typically achieved can be understood by an example of a quantity of a gas. Suppose molecules are assigned some arbitrary initial velocities that do not fit the Maxwell distribution. Molecular dynamics calculations show that within a few collisions the distribution becomes Maxwellian – and results in a locally well-defined temperature.²⁸ Similar reasoning can be applied to solids with atoms treated as linear harmonic oscillators. All known transport studies assume that there is a well defined temperature at a point in the system at a given time, whether it is fixed in time (steady state) or varies with time (transient state). Thus, all transport studies assume local equilibrium.

The basic concept of local equilibrium, extensively discussed in textbooks on irreversible thermodynamics, is that even in systems not in global equilibrium Gibbsian laws of thermodynamics apply to microscopic volumes suitably chosen.²⁸ This is the criterion of local equilibrium in an otherwise global no equilibrium. In such cases, all extensive thermodynamic functions are replaced by their local densities.²⁸ This formulation dates back to the 1930s with the classic papers by Onsager. The implications of local equilibrium in predominantly oxygen ion conductors in a globally no equilibrium state, which forms the basis for the proposed electrode delamination model, is discussed below.

3.1.3 Nonequilibrium Thermodynamics, Local Equilibrium and Transport in Predominantly Oxygen Ion Conductors

An oxygen ion conductor with cation sublattice is considered virtually immobile. In an oxygen ion conductor, the existence of local equilibrium with respect to oxygen is described by^{33,34}



which leads to

$$\frac{1}{2} \mu_{O_2}(\vec{r}, t) + 2\mu_e(\vec{r}, t) = \mu_{O^{2-}}(\vec{r}, t) \quad (3-2)$$

or

$$\frac{1}{2} \mu_{O_2}(\vec{r}, t) + 2\tilde{\mu}_e(\vec{r}, t) = \tilde{\mu}_{O^{2-}}(\vec{r}, t) \quad (3-3)$$

where $\mu_i(\vec{r}, t)$'s are the local (function of position) chemical potentials at time t , and $\tilde{\mu}_i(\vec{r}, t)$'s are the local electrochemical potentials given by $\tilde{\mu}_i(\vec{r}, t) = \mu_i(\vec{r}, t) + z_i F \Phi(\vec{r})$ for species i where z_i is the valence (including sign), F is the Faraday constant, and $\Phi(\vec{r})$ is the local electrostatic potential. There

is no time dependence in $\Phi(\vec{r})$ since only cases wherein in the externally applied voltage is fixed are being considered. In such a case, the local $\Phi(\vec{r})$ is instantaneously established (which assumes cations are virtually immobile, anions exhibit rapid transport, and no interfacial space charges develop in response to applied voltage). If space charge develops, the electrostatic potential may exhibit time dependence as the double layer capacitance builds up. The \vec{r} in $\Phi(\vec{r})$ denotes the position vector. Local equilibrium also implies^{33,33}

$$\frac{1}{2}\delta\mu_{O_2}(\vec{r},t) + 2\delta\tilde{\mu}_e(\vec{r},t) = \delta\tilde{\mu}_{O^{2-}}(\vec{r},t) \quad (3-4)$$

where δX is a differential variation in X .

In a typical oxygen ion conductor, the ionic current density is given by^{33,33}

$$I_{O^{2-}}(\vec{r},t) = -\frac{\sigma_{O^{2-}}(\vec{r},t)}{(-2)F} \nabla \tilde{\mu}_{O^{2-}}(\vec{r},t) = \frac{\sigma_{O^{2-}}(\vec{r},t)}{2F} \nabla \tilde{\mu}_{O^{2-}}(\vec{r},t) \quad (3-5)$$

where $\sigma_{O^{2-}}(\vec{r},t)$ is the oxygen ion conductivity at \vec{r} and time, t . If the material is predominantly an oxygen ion conductor, then $\sigma_{O^{2-}}(\vec{r},t) \gg \sigma_e(\vec{r},t)$, where $\sigma_e(\vec{r},t)$ is the electronic conductivity at \vec{r} and time, t . Note that the electrical current (which is the rate of transport of electrical charge, Coulombs, per unit time) due to oxygen ions, $I_{O^{2-}}(\vec{r},t)$ is in the opposite direction to the flux of oxygen ions, $j_{O^{2-}}(\vec{r},t)$, as oxygen ions are negatively charged. The same is the case with negatively charged electrons.

This report quantitatively examines only the ‘true’ steady state. A brief description of an ‘apparent’^a steady state and its significance is also presented. It is understood that local equilibrium is equally applicable in the vast majority of no equilibrium cases involving transient states. In a ‘true’ or an ‘apparent’ steady state in a predominantly oxygen ion conductor, $I_{O^{2-}}(\vec{r},t)$, $\sigma_{O^{2-}}(\vec{r},t)$, $\mu_{O^{2-}}(\vec{r},t)$ are nearly constant, independent of time, for given fixed externally applied conditions, such as a fixed applied voltage and results in a fixed total measured current. Also, in most such cases, $\sigma_{O^{2-}}(\vec{r},t)$, is a constant and may be given by $\sigma_{O^{2-}}$. Thus, the time dependence will be dropped from now on, except when the discussion explicitly concerns time dependence. The \vec{r} will also be dropped in some places, but it is still understood that reference is being made to the evaluation of relevant properties at some position, \vec{r} . Some discussion of ‘transient’ states will be presented later.

a. The meaning and significance of an ‘apparent’ steady state is discussed later.

3.1.4 Electrochemical Potential of O^{2-} in Predominantly O^{2-} Ion Conductors

Assuming ionic conductivity to be independent of position and invariant with time (steady state), the $\tilde{\mu}_{O^{2-}}$ (for a one dimensional problem) is a linear function of position. The electrochemical potential of oxygen ions is given by^{33,34}

$$\tilde{\mu}_{O^{2-}} = \mu_{O^{2-}} - 2F\Phi \quad (3-6)$$

The chemical potential of ions is not measurable, although it is a useful concept for formulations of transport problems. Often, it is assumed that the chemical potential of oxygen ions in the electrolyte, $\mu_{O^{2-}}$, is constant independent of position. This is because the concentration of oxygen vacancies is much smaller than the concentration of oxygen ions in the vast majority of materials of interest, and thus, effectively, oxygen ion concentration is essentially fixed. For this reason, it is commonly assumed that $\mu_{O^{2-}}$ is independent of position. This leads to a linear variation of Φ with position or $\nabla\Phi = \text{constant}$ (one dimensional case) for a fixed applied voltage. An important point to note, however, is that Φ is also not experimentally measurable. What one experimentally measures using an inert metallic probe and a voltmeter is φ given by³⁵

$$\varphi = -\frac{\mu_e}{F} + \Phi. \quad (3-7)$$

The φ , electric potential, is effectively negative of the reduced electrochemical potential of electrons given in units of volts.³⁵ In metals which have high free electron concentration (given here as number of free electrons per unit volume), the φ and Φ (or more accurately the differences $\Delta\varphi(\vec{r}, \vec{r}_o)$ and $\Delta\Phi(\vec{r}, \vec{r}_o)$ between two positions \vec{r} and \vec{r}_o) are treated as the same. In materials with very low electron concentration, however, it is important to recognize the distinction between φ and Φ .³⁵ Using the local equilibrium concept, the electrochemical potential of oxygen ions is also given as

$$\tilde{\mu}_{O^{2-}} = \mu_{O^{2-}} - 2F\Phi = \frac{1}{2}\mu_{O_2} - 2F\varphi \quad (3-8)$$

where both μ_{O_2} and φ are the experimentally measureable potentials. That is, the definition of $\tilde{\mu}_{O^{2-}}$ can be given in terms of experimentally nonmeasurable potentials ($\mu_{O^{2-}}, \Phi$) or experimentally measurable potentials (μ_{O_2}, φ). It can also be shown that electrochemical potential of oxygen ions, $\tilde{\mu}_{O^{2-}}$, is in fact deducible from various experimental measurements, and thus is a measurable parameter. This is true of all ionic species. Thus, although the two definitions of $\tilde{\mu}_{O^{2-}}$ are equivalent (in terms of $\mu_{O^{2-}}$ and Φ , or in terms of μ_{O_2} and φ), from an experimental standpoint, the one in terms of measurable potentials is more useful. Much of the literature, however, is based on descriptions in terms immeasurable ionic chemical potentials and electrostatic potential.

3.1.5 Chemical Potential of Neutral Oxygen and Electric Potential in Predominantly Oxygen Ion Conductors

It is now assumed that electron and hole concentrations are very small, which is typical of an oxygen ion conductor with negligible electronic conductivity such as YSZ. Suppose, for example, the electron concentration is $\sim 2 \times 10^{10} \text{ cm}^{-3}$ at 800°C , then for an assumed electron field mobility of $\sim 0.05 \text{ cm}^2 \text{ Volt}^{-1} \text{ s}^{-1}$, the electronic conductivity of YSZ would be $\sim 10^{-10} \text{ Scm}^{-1}$, an exceptionally small value. Over a wide range of oxygen partial pressures, the oxygen vacancy concentration is constant (extrinsic region), say $\sim 10^{21} \text{ cm}^{-3}$, which is much larger than the electron concentration. The corresponding oxygen ion conductivity may be on the order of 10^{-2} to 10^{-1} Scm^{-1} , which is orders of magnitude larger than the electronic conductivity. Thus, the material is a predominantly ionic conductor with ion transport numbers of nearly unity.

The electron concentration, however, is a function of the local oxygen partial pressure, and thus is generally position-dependent. For example, the dependence may be of the type $n(\vec{r}) \sim (p_{O_2}(\vec{r}))^{-1/4}$, typical of many oxides.³⁶ Electron concentration may thus exhibit large relative changes subject to changes in the local oxygen partial pressure. Yet, the material may still be an essentially ionic conductor. For example, even if the electron concentration locally increases to 10^{14} cm^{-3} , the ionic transport number remains close to unity. Assuming the dilute solution approximation for electrons, then $\mu_e(\vec{r}) \propto RT \ln n(\vec{r})$ or $\mu_e(\vec{r}) \propto -RT \ln p_{O_2}(\vec{r})$ or $\mu_e(\vec{r}) \propto -\mu_{O_2}(\vec{r})$ or $\tilde{\mu}_e(\vec{r}) = -F\phi(\vec{r}) \propto -\mu_{O_2}(\vec{r})$ or $\phi(\vec{r}) \propto \mu_{O_2}(\vec{r})$.

This means, by changing $\mu_{O_2}(\vec{r})$ locally, the local $\phi(\vec{r})$ will change proportionately. Alternatively, if changing $\phi(\vec{r})$ locally, the $\mu_{O_2}(\vec{r})$ will change proportionately. The latter aspect is the one relevant to degradation. The preceding discussion suggests that all those factors which locally increase $\phi(\vec{r})$, will also locally increase $\mu_{O_2}(\vec{r})$. Finally, this means

$$p_{O_2}(\vec{r}) \propto \exp\left[\frac{4F\phi(\vec{r})}{RT}\right] \quad (3-9)$$

which is routinely used but mainly for measurements made at *electrodes*, and that modest changes in $\phi(\vec{r})$ may locally change $p_{O_2}(\vec{r})$ orders of magnitude, possibly leading to mechanical cracking. In most studies, one often investigates ϕ (dependent variable) as a function of $\mu_{O_2}(\vec{r})$ or $p_{O_2}(\vec{r})$ (independent variable). Here, $\phi(\vec{r})$ is treated as the independent variable and $\mu_{O_2}(\vec{r})$ or $p_{O_2}(\vec{r})$ as the dependent variable.

3.1.6 True and Apparent Steady States

Much of this manuscript deals with true steady states. However, there are many situations in which the steady state is in fact not a true steady state, but rather an apparent steady state. Consider for example a case wherein the externally measured voltage and current are essentially constant (independent of time). Since the electrolyte is a predominantly ionic conductor, it means at any position, \vec{r} , the electrochemical potential of oxygen ions, $\tilde{\mu}_{O_2-}(\vec{r})$, is also independent of time. Since, $\tilde{\mu}_{O_2-}(\vec{r}) = \mu_{O_2-}(\vec{r}) - 2F\Phi(\vec{r})$ it is also clear (and commonly understood to be so) that $\mu_{O_2-}(\vec{r})$ and $\Phi(\vec{r})$ are both independent of time

(for a fixed applied voltage). An immediate and apparently obvious (and often incorrect) conclusion is that steady state is indeed established. However, note that local equilibrium is valid and the material is a predominantly ionic conductor. Thus, the electron concentration is rather small. No guarantee exists that the electron concentration remains constant, however. Any slight changes in composition that may occur locally do not affect $\mu_{O^{2-}}(\vec{r})$ or $\Phi(\vec{r})$ or $\tilde{\mu}_{O^{2-}}(\vec{r})$, but can affect $\mu_e(\vec{r})$ (and $\phi(\vec{r})$) and thus also affect $\mu_{O_2}(\vec{r})$. That is, the local Fermi level, $\mu_e(\vec{r}, t)$, may depend on both position and time, even when an apparent steady state is established, wherein the establishment of the steady state is judged on the basis of measured stationary voltage and measured stationary current. Note now that oxygen ion electrochemical potential is given by

$$\tilde{\mu}_{O^{2-}}(\vec{r}) = \mu_{O^{2-}}(\vec{r}) - 2F\Phi(\vec{r}) = \mu_{O^{2-}}(\vec{r}) - 2\mu_e(\vec{r}, t) - 2F\Phi(\vec{r}) + 2\mu_e(\vec{r}, t) = \frac{1}{2}\mu_{O_2}(\vec{r}, t) - 2F\phi(\vec{r}, t) \quad (3-10)$$

This is a very significant result. It states that even when $\tilde{\mu}_{O^{2-}}(\vec{r})$, $\mu_{O^{2-}}(\vec{r})$, and $\Phi(\vec{r})$ are nearly independent of time, $\mu_{O_2}(\vec{r}, t)$ and $\phi(\vec{r}, t) = -\frac{\mu_e(\vec{r}, t)}{F} + \Phi(\vec{r})$ may indeed be time dependent. This represents an apparent steady state – not a true steady state. $\mu_{O^{2-}}(\vec{r})$ and $\Phi(\vec{r})$ are not experimentally measureable, but $\mu_{O_2}(\vec{r}, t)$ and $\phi(\vec{r}, t)$ are experimentally measurable. Thus, even in an apparent steady state, the measurable thermodynamic parameters, $\mu_{O_2}(\vec{r}, t)$ and $\phi(\vec{r}, t)$, may exhibit time dependence, even when the externally measured voltage and current are virtually independent of time. This is an apparent steady state – not a true steady state.

Returning to the local equilibrium involving oxygen ions, electrons, and oxygen, note that

$$\mu_{O^{2-}}(\vec{r}) = \frac{1}{2}\mu_{O_2}(\vec{r}, t) + 2\mu_e(\vec{r}, t) \quad (3-11)$$

is the same as Equation 3-2. In a typical oxygen ion conductor at a given temperature, $\mu_{O^{2-}}$ is essentially fixed. Any changes that occur in the local chemical potential of electrons (Fermi level), $\mu_e(\vec{r}, t)$, affect the local chemical potential of oxygen, $\mu_{O_2}(\vec{r}, t)$ and thus affect the local oxygen pressure, $p_{O_2}(\vec{r}, t)$.

All those factors which lower the $\mu_e(\vec{r}, t)$ will raise $\mu_{O_2}(\vec{r}, t)$ and raise $p_{O_2}(\vec{r}, t)$. Under some situations, this may lead to degradation. This is the fundamental basis for the oxygen electrode delamination mechanism discussed in this manuscript.

3.2 Analysis of Currents through a Cell

3.2.1 Ionic and Electronic Currents through the Cell and the Measured Current

The typical materials of an SOEC are as follows: (1) Electrolyte: YSZ, a predominantly oxygen ion conductor. Typical composition is 8 mol% Y_2O_3 to 92 mol% ZrO_2 ; (2) electrode exposed to predominantly water vapor and H_2 , the steam- H_2 electrode: $Ni + YSZ$; (3) electrode exposed to predominantly oxygen, the oxygen electrode: typical composition is $LSM + YSZ$. Many other materials may be used for the various components. Thus, in what follows the terminology used will be generic; steam- H_2 electrode, oxygen electrode, and electrolyte.

In the fuel cell mode, the oxygen electrode is the cathode and the steam-H₂ electrode is the anode. In the electrolyzer mode, however, the oxygen electrode is the anode and the steam-H₂ electrode is the cathode. Since the focus of this manuscript is on the electrolyzer, the oxygen electrode is nominally the anode and the steam-H₂ electrode is nominally the cathode.

The electrode reactions in the electrolyzer mode are as follows:

At the steam-H₂ electrode:



O²⁻ ions transport through the electrolyte to the oxygen electrode.

At the oxygen electrode:



The 2e' transport in the external circuit from the oxygen electrode to the steam-H₂ electrode.

The overall reaction is



An important point is that the above reaction can also be written simply as isothermal compression of oxygen from $p_{\text{O}_2}^{\text{St-H}_2}$ at the steam-H₂ electrode to $p_{\text{O}_2}^{\text{Ox}}$ at the oxygen electrode. Since it is compression, it represents work done on the system. Figure 5 shows a schematic of the cell. The steam-H₂ electrode is exposed to a mixture of H₂ and H₂O (with very low oxygen partial pressure) and the oxygen electrode is exposed to a mixture of O₂ and H₂O, in practice essentially pure oxygen (negligible hydrogen partial pressure).

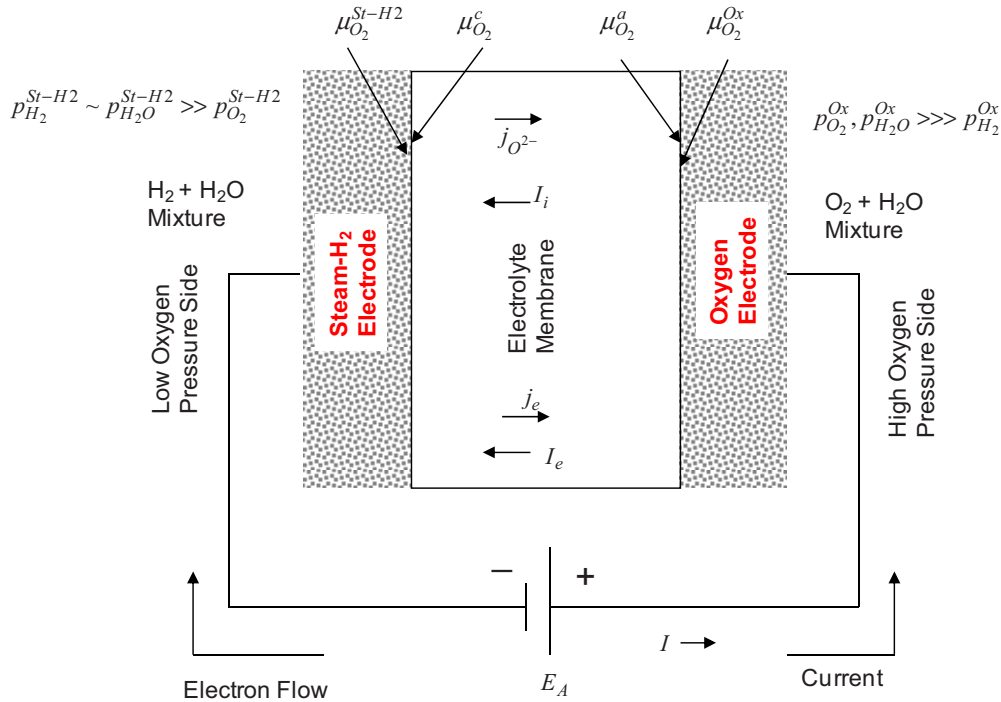


Figure 5. A schematic of a solid oxide electrolyzer cell, when operated in the electrolyzer mode.

3.2.2 Equivalent Circuits

Figure 6 is an equivalent circuit for the electrolyzer cell in a true steady state with an externally applied voltage source, E_A ^b. In Figure 6, r_i^c and r_i^a are respectively the area specific ion charge transfer resistances at the steam-H₂ electrode/electrolyte interface and the oxygen electrode/electrolyte interface. As-defined, these only refer to the physically sharp electrolyte/electrode interfaces and do not include the porous electrode contributions to the overall electrode reactions²⁷. This is because one must then include simultaneous and parallel transport through both the solid (ions and electrons/holes) and the porous (gas) regions of the electrodes. The resistances, r_i^c and r_i^a are effectively polarization resistances (excluding the porous electrodes) and may be described using Butler-Volmer type of phenomenological models. The r_e^c and r_e^a are area specific resistances for direct electron transfer across the steam-H₂ electrode/electrolyte interface and oxygen electrode/electrolyte interface, respectively. In the semiconductor terminology, the r_e^c and r_e^a are area specific contact resistances (non-ohmic contact). Finally, r_i^{el} and r_e^{el} are respectively the ionic and electronic area specific resistances of the electrolyte, given in terms of the respective conductivities and the electrolyte thickness. Note that r_e^c , r_e^a and r_e^{el} may be very large, but are not mathematically infinite.

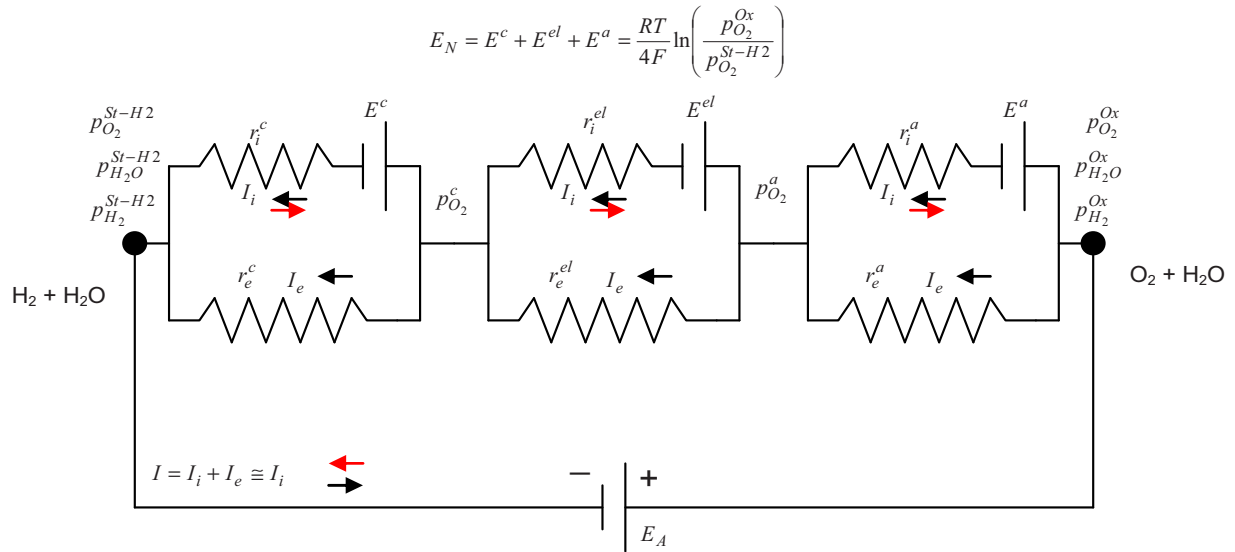


Figure 6. An equivalent circuit for the cell in a ‘true’ steady state.

Figure 7 is an equivalent circuit for the electrolyzer cell in an apparent steady state. The apparent steady state is characterized by a nearly constant voltage across the cell and a nearly constant externally measured current. Since E_A is fixed, the voltage across the cell is fixed. However, the electronic current through the electrolyte, which is much smaller than the ionic current, may vary with position and time.

b. It is assumed here that the internal resistance of the external source with voltage E_A is negligible. It can be easily included in the analysis.

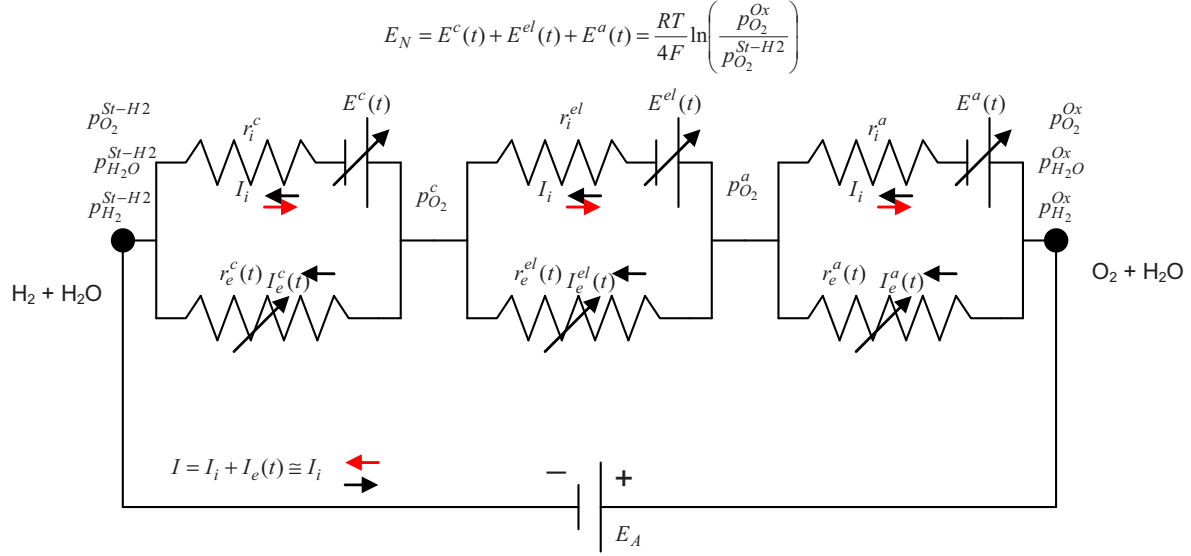


Figure 7. An equivalent circuit for the cell in an ‘apparent’ steady state.

This effectively reflects as time dependent individual internal Nernst potentials (with their sum still being a constant, E_N) and also time-dependent local electric potential, $\phi(\vec{r}, t)$ (with $\phi^{Ox} - \phi^{Steam-H2}$ fixed and equal to the applied voltage E_A). The following discussion is restricted to the true steady state depicted in Figure 7.

The applied voltage E_A is in the opposite direction to the Nernst voltage E_N created by differing oxygen partial pressures at the two electrodes; that is, the positive of the cell is connected to the positive of the external source and the negative of the cell is connected to the negative of the external source. When $E_A < E_N$, the cell does work on the external source (charging the externally connected battery). This is the fuel cell mode. When $E_A > E_N$, the external source does work on the cell. This is the electrolyzer mode. The Nernst voltage generated by differing oxygen partial pressures at the two electrodes is given by

$$E_N = \frac{RT}{4F} \ln \left(\frac{p_{O_2}^{Ox}}{p_{O_2}^{St-H2}} \right) \quad (3-15)$$

Note that $p_{O_2}^{St-H2} \ll p_{O_2}^{Ox}$, therefore, as given $E_N > 0$ and $E_A > 0$. The Nernst potential can also be given in terms of the EMFs across the two interfaces and the bulk electrolyte by

$$E_N = E^a + E^{el} + E^c = \frac{RT}{4F} \ln \left(\frac{p_{O_2}^{Ox}}{p_{O_2}^a} \right) + \frac{RT}{4F} \ln \left(\frac{p_{O_2}^a}{p_{O_2}^c} \right) + \frac{RT}{4F} \ln \left(\frac{p_{O_2}^c}{p_{O_2}^{St-H2}} \right) = \frac{RT}{4F} \ln \left(\frac{p_{O_2}^{Ox}}{p_{O_2}^{St-H2}} \right) \quad (3-16)$$

In terms of the chemical potentials of oxygen, Equation 3-16 may also be given as

$$E_N = E^a + E^{el} + E^c = \frac{(\mu_{O_2}^{Ox} - \mu_{O_2}^a)}{4F} + \frac{(\mu_{O_2}^a - \mu_{O_2}^c)}{4F} + \frac{(\mu_{O_2}^c - \mu_{O_2}^{St-H2})}{4F} = \frac{(\mu_{O_2}^{Ox} - \mu_{O_2}^{St-H2})}{4F} \quad (3-17)$$

Relationships between ionic and electronic current densities, internal EMFs, and electric potentials, ϕ 's are given by (by solving the circuit given in Figure 6)

$$I_e r_e^c = -E^c + I_i r_i^c = \phi^{Steam-H_2} - \phi^c < 0 \quad (3-18)$$

$$I_e r_e^{el} = -E^{el} + I_i r_i^{el} = \phi^c - \phi^a < 0 \quad (3-19)$$

and

$$I_e r_e^a = -E^a + I_i r_i^a = \phi^a - \phi^{Ox} < 0 \quad (3-20)$$

The electronic area specific resistances, r_e^c and/or r_e^a and/or r_e^{el} are expected to be much larger than the ionic resistance for a typical electrolyzer cell. That is, r_e^c and/or r_e^{el} and/or $r_e^a \gg r_i^c, r_i^{el}, r_i^a$. Let us write

$$R_i = r_i^c + r_i^{el} + r_i^a \quad (3-21)$$

and

$$R_e = r_e^c + r_e^{el} + r_e^a. \quad (3-22)$$

These represent area specific ionic and electronic resistances of the cell, which include electrolyte/electrode interfaces. Now, $R_e \gg R_i$. However, the electronic resistances cannot be mathematically infinite and thus cannot be dropped out of the analysis (and cannot be dropped out of the equivalent circuit) since this will violate local equilibrium and the chemical potential of oxygen will be indeterminate.^{27,37} That is, R_e is very large, but cannot be set to infinity *a-priori*. Note that the magnitude

of the slope of V-I curve is $\frac{R_i R_e}{(R_i + R_e)} \approx R_i$. Thus, the R_e is not reflected in typical experimental measurements, such as the voltage – current density plots or impedance spectra.

Figure 8 shows a schematic plot of voltage, E_A , and current, I . The externally measured current is $I = I_i + I_e$. The point corresponding to $E_A = E_N$ strictly represents $I_i = 0$. The externally measured current, I , is mathematically zero when the applied voltage is given by $E_A = \frac{E_N R_e}{(R_i + R_e)}$. If $R_e \gg R_i$, then the current is negligible when $E_A \approx E_N$ and nearly corresponds to zero of the x-axis in Figure 4. Thus, when $E_A = E_N$, strictly the measured current is $I = I_e$. Over the entire range of the applied voltage across the cell, which is E_A , the net electronic current has the same sign in both modes of operation (SOFC and SOEC) since $E_A > 0$ has been selected. The sign of the ionic current, I_i , however, depends upon the relative magnitudes of E_A and E_N .^c The positive direction of the current

c. In the SOFC *stack* degradation model described previously,⁷ the direction of the ionic current is always fixed. When cell imbalance occurs in a SOFC stack, the electronic current switches sign. Fundamental requirement for degradation to occur is that ionic and electronic currents through the electrolyte are in the same direction, regardless of the mode of operation, SOFC or SOEC.²⁷ In SOFC, this occurs in a stack as a result of cell imbalance.⁷ In the electrolyzer degradation model examined in this manuscript, this condition occurs even in a single cell.

axis corresponds to $E_A < \frac{E_N R_e}{(R_i + R_e)} \approx E_N$, and the negative direction of the current axis corresponds to

$E_A > \frac{E_N R_e}{(R_i + R_e)} \approx E_N$. When the cell is operated in the fuel cell mode, the ionic and the electronic

currents through the cell are in opposite directions. When the cell is operated in the electrolyzer mode, the ionic and the electronic currents through the cell are in the same direction. In predominantly oxygen ion conductors, the electronic current is small in magnitude, yet it has a significant effect on chemical potentials.²⁷

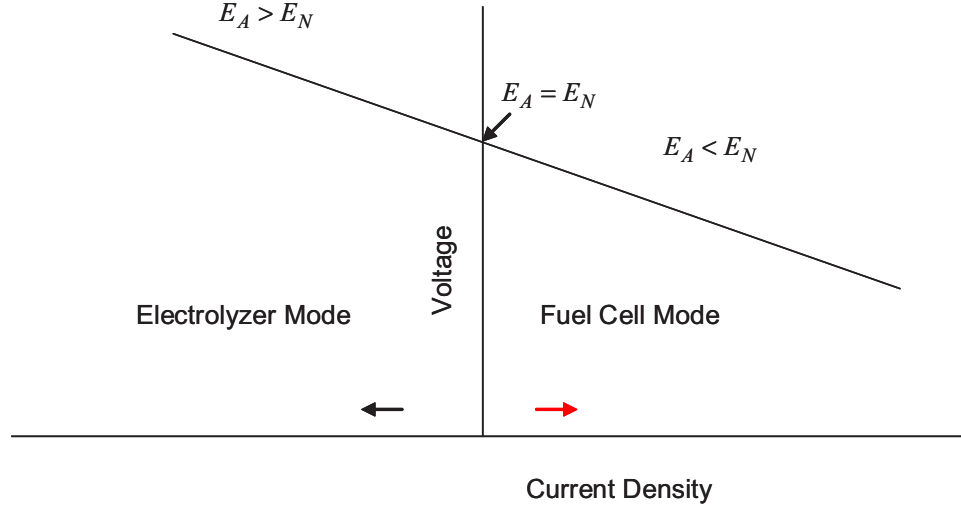


Figure 8. A schematic plot of the measured voltage (which is also the applied voltage, E_A) vs. the measured current density.

Note that

$$\varphi^{Ox} - \varphi^{St-H2} = \varphi^{Ox} - \varphi^a + \varphi^a - \varphi^c + \varphi^c - \varphi^{St-H2} > 0 \quad (3-23)$$

is the measured voltage across the cell (which is also E_A). For all cases considered in this report,

$$E_A = \varphi^{Ox} - \varphi^{St-H2} > 0.$$

From the equivalent circuit in Figure 6, note that

$$I_e (r_e^c + r_e^{el} + r_e^a) + E_A = I_e R_e + E_A = 0 \quad (3-24)$$

and

$$I_i (r_i^c + r_i^{el} + r_i^a) - E_N + E_A = I_i R_i - E_N + E_A = 0 \quad (3-25)$$

Thus,

$$I_e = -\frac{E_A}{(r_e^c + r_e^{el} + r_e^a)} = -\frac{E_A}{R_e} < 0 \quad (3-26)$$

and

$$I_i = -\frac{(E_A - E_N)}{(r_i^c + r_i^{el} + r_i^a)} = -\frac{(E_A - E_N)}{R_i} < 0 \quad (3-27)$$

as long as H₂O decomposition is achieved, that is as long as $(E_A - E_N) > 0$, the measured current (in the external circuit) is $I = I_i + I_e \approx I_i$. Thus, as defined, the measured current, $I < 0$ in the electrolyzer mode and $I > 0$ in the fuel cell mode.

Since the electrolyte is a predominantly ionic conductor, $R_e \gg R_i$, it also means $|I_i| \gg |I_e|$ for most situations (except when $E_A \approx E_N$). The externally measured current (density) is thus $I = I_i + I_e \approx I_i$ for most cases (that is, as long as the applied voltage, E_A , is sufficiently different from the Nernst voltage, E_N).

3.2.3 Chemical Potential and Pressure of Oxygen inside the Electrolyte (just near the Electrodes)

From Equations 3-15 through 3-27, the chemical potentials of oxygen *in the electrolyte*, just near the electrode/electrolyte interfaces, are given by Virkar.^{7,27}

$$\mu_{O_2}^c = \mu_{O_2}^{St-H_2} + 4F \left\{ \frac{E_A r_e^c}{R_e} - \frac{(E_A - E_N) r_i^c}{R_i} \right\} = \mu_{O_2}^{St-H_2} + 4F \left\{ \left(\phi^c - \phi^{St-H_2} \right) - \frac{(E_A - E_N) r_i^c}{R_i} \right\} \quad (3-28)$$

inside the *electrolyte*, just near the steam-H₂ electrode, and

$$\mu_{O_2}^a = \mu_{O_2}^{Ox} - 4F \left\{ \frac{E_A r_e^a}{R_e} - \frac{(E_A - E_N) r_i^a}{R_i} \right\} = \mu_{O_2}^{Ox} - 4F \left\{ \left(\phi^{Ox} - \phi^a \right) - \frac{(E_A - E_N) r_i^a}{R_i} \right\} \quad (3-29)$$

inside the *electrolyte*, just near the oxygen electrode.

The corresponding oxygen partial pressures *in the electrolyte*, just near the electrode/electrolyte interfaces, are given by

$$p_{O_2}^c = p_{O_2}^{St-H_2} \exp \left[\frac{4F}{RT} \left\{ \frac{E_A r_e^c}{R_e} - \frac{(E_A - E_N) r_i^c}{R_i} \right\} \right] = p_{O_2}^{St-H_2} \exp \left[\frac{4F}{RT} \left\{ \left(\phi^c - \phi^{St-H_2} \right) - \frac{(E_A - E_N) r_i^c}{R_i} \right\} \right] \quad (3-30)$$

inside the *electrolyte*, just near the steam-H₂ electrode, and

$$p_{O_2}^a = p_{O_2}^{Ox} \exp \left[-\frac{4F}{RT} \left\{ \frac{E_A r_e^a}{R_e} - \frac{(E_A - E_N) r_i^a}{R_i} \right\} \right] = p_{O_2}^{Ox} \exp \left[-\frac{4F}{RT} \left\{ \left(\phi^{Ox} - \phi^a \right) - \frac{(E_A - E_N) r_i^a}{R_i} \right\} \right] \quad (3-31)$$

inside the *electrolyte*, just near the oxygen electrode.

Note that the μ_{O_2} 's (and the p_{O_2} 's) are described in terms of measureable transport parameters (r_i^c , r_i^a , and R_i); Nernst voltage, E_N ; applied voltage, E_A ; electric potentials at the two electrodes, ϕ^{St-H2} and ϕ^{Ox} ; and in principle measureable electric potentials in the electrolyte just near the electrolyte/electrode interfaces, ϕ^c and ϕ^a .^{7,27} All discussion here assume a true steady state in which electronic and ionic current densities are uniform through all three segments of the equivalent circuit, that is $\vec{\nabla} \cdot \vec{I}_i = 0$ and $\vec{\nabla} \cdot \vec{I}_e = 0$. Thus, a true steady state must *always* have $\phi^{Ox} > \phi^a > \phi^c > \phi^{St-H2}$ (for the case, $\phi^{Ox} > \phi^{St-H2}$, selected here, that is for $E_A > 0$).²⁷ The spatial variation of oxygen partial pressure *within the electrolyte*, however, depends upon the relative values of transport parameters and the magnitude of the applied voltage E_A in relation to the Nernst voltage E_N . Now consider two cases.

3.2.3.1 SOFC Mode – Applied Voltage < Nernst Voltage

In this case, the cell operates in a fuel cell mode and $I_i > 0$.^d Thus, no electrolysis occurs. Rather, electrical power is generated by the electrochemical oxidation of hydrogen, with the power density given by $\left| (\phi^{Ox} - \phi^{St-H2}) I \right|$. Oxygen ions thus transport from the oxygen electrode through the electrolyte to the steam-H₂ electrode. The oxygen partial pressures *within the electrolyte* just near the electrodes are given by

$$p_{O_2}^c = p_{O_2}^{St-H2} \exp \left[\frac{4F}{RT} \left\{ (\phi^c - \phi^{St-H2}) + \frac{(E_N - E_A)r_i^c}{R_i} \right\} \right] > p_{O_2}^{St-H2} \quad (3-32)$$

and

$$p_{O_2}^a = p_{O_2}^{Ox} \exp \left[-\frac{4F}{RT} \left\{ (\phi^{Ox} - \phi^a) + \frac{(E_N - E_A)r_i^a}{R_i} \right\} \right] < p_{O_2}^{Ox} \quad (3-33)$$

Now, $\phi^c - \phi^{St-H2} > 0$, $\phi^{Ox} - \phi^a > 0$ and $E_N - E_A > 0$. Thus, the signs of the terms in the curly brackets in Equations 3-32 and 3-33 are positive. Also, therefore, for this case (single cell only – not necessarily an unbalanced cell in a stack in which the terminal voltage across an unbalanced cell may switch sign⁷) must have $\mu_{O_2}^{St-H2} < \mu_{O_2}^c < \mu_{O_2}^a < \mu_{O_2}^{Ox}$ and thus $p_{O_2}^{St-H2} < p_{O_2}^c < p_{O_2}^a < p_{O_2}^{Ox}$.⁷ Figure 9 shows a schematic of the variation of ϕ and μ_{O_2} through the cell (electrolyte). That is, in such a case the p_{O_2} within the electrolyte is mathematically bounded by the values in the gas phase at the electrodes (bounded by $p_{O_2}^{St-H2}$, $p_{O_2}^{Ox}$), and high pressures do not develop. Thus, no degradation (of the type discussed here) should occur.

d. In the earlier work on solid oxide fuel cells, the author had used a different convention; the oxygen electrode was on the left side and the fuel electrode was on the right side, for which the current was in the opposite direction; that is in the earlier work we had set $I_i < 0$ in the fuel cell mode since the oxygen electrode (cathode) was the left electrode.^{7,27}

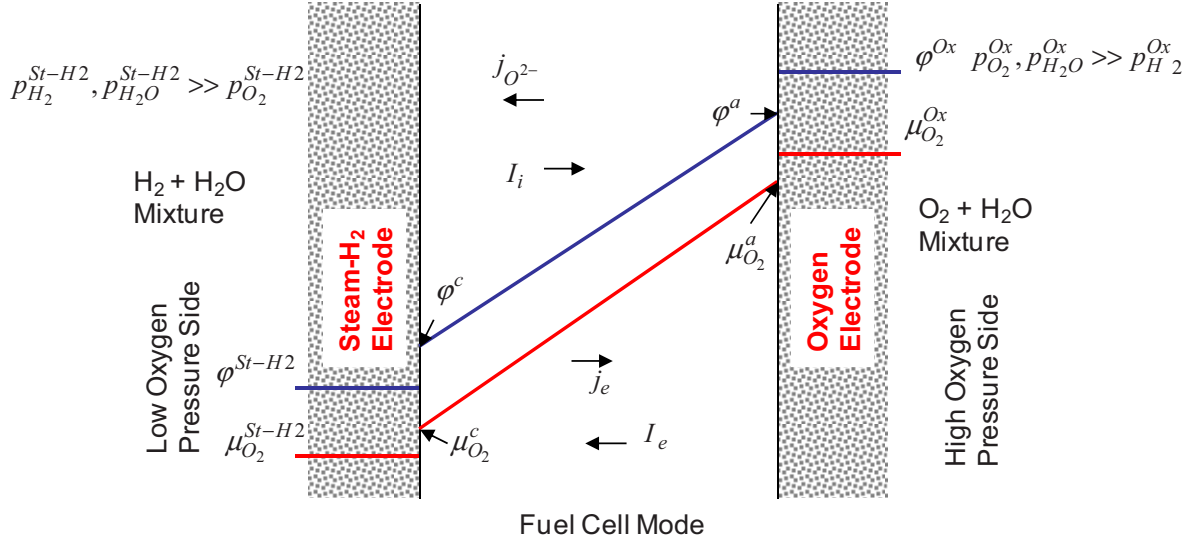


Figure 9. Schematic variations of electric potential (ϕ) and oxygen chemical potential (μ_{O_2}) through the electrolyte in the fuel cell mode (true steady state).

3.2.3.2 SOEC Mode – Applied Voltage > Nernst Voltage

This is the electrolyzer mode. The oxygen partial pressures are

$$p_{O_2}^c = p_{O_2}^{St-H2} \exp \left[\frac{4F}{RT} \left\{ (\phi^c - \phi^{St-H2}) - \frac{(E_A - E_N)r_i^c}{R_i} \right\} \right] \quad (3-34)$$

and

$$p_{O_2}^a = p_{O_2}^{Ox} \exp \left[-\frac{4F}{RT} \left\{ (\phi^{Ox} - \phi^a) - \frac{(E_A - E_N)r_i^a}{R_i} \right\} \right] \quad (3-35)$$

which are the same equations as Equations 3-31 and 3-32. Now $\phi^c - \phi^{St-H2} > 0$, $\phi^{Ox} - \phi^a > 0$, however, $E_A - E_N > 0$. Thus, whether $p_{O_2}^c$ is greater than or smaller than $p_{O_2}^{St-H2}$ will depend upon the sign of the exponent (terms in the curly brackets in Equation 3-34); and whether $p_{O_2}^a$ is greater than or smaller than $p_{O_2}^{Ox}$ will depend upon the sign of the exponent (terms in the curly brackets in Equation 3-35). That is, depending upon the relative magnitudes of the various transport parameters, according to Equations 3-34 and 3-35, it is possible that $\mu_{O_2}^c (p_{O_2}^c)$ may decrease below $\mu_{O_2}^{St-H2} (p_{O_2}^{St-H2})$ and/or $\mu_{O_2}^a (p_{O_2}^a)$ may increase above $\mu_{O_2}^{Ox} (p_{O_2}^{Ox})$. Thus, in the electrolyzer mode, the $\mu_{O_2} (p_{O_2})$ within the electrolyte need not be mathematically bounded by values at the electrodes (by values in the gas phases).²⁷

Note, if $\left\{ \left(\varphi^c - \varphi^{St-H2} \right) - \frac{(E_A - E_N)r_i^c}{R_i} \right\} < 0$, then $\mu_{O_2}^c < \mu_{O_2}^{St-H2}$ ($p_{O_2}^c < p_{O_2}^{St-H2}$) and if $\left\{ \left(\varphi^{Ox} - \varphi^a \right) - \frac{(E_A - E_N)r_i^a}{R_i} \right\} < 0$, then $\mu_{O_2}^a > \mu_{O_2}^{Ox}$ ($p_{O_2}^a > p_{O_2}^{Ox}$). Depending upon the transport parameters and the operating conditions, either one, both or none of the situations may occur.

Figure 10 shows a schematic wherein the $\mu_{O_2}^a > \mu_{O_2}^{Ox}$ ($p_{O_2}^a > p_{O_2}^{Ox}$). Recall that in the electrolyzer mode, the steam-H₂ electrode (low oxygen partial pressure) is the cathode and the oxygen electrode (high oxygen pressure) is the anode. If the $\mu_{O_2}^c$ ($p_{O_2}^c$) decreases to a value below the thermodynamic stability of YSZ with respect to metals (Y, Zr), local electrolyte decomposition is possible. If the $\mu_{O_2}^a$ ($p_{O_2}^a$) increases to too high a value, electrode delamination (along oxygen electrode/electrolyte interface) is possible.

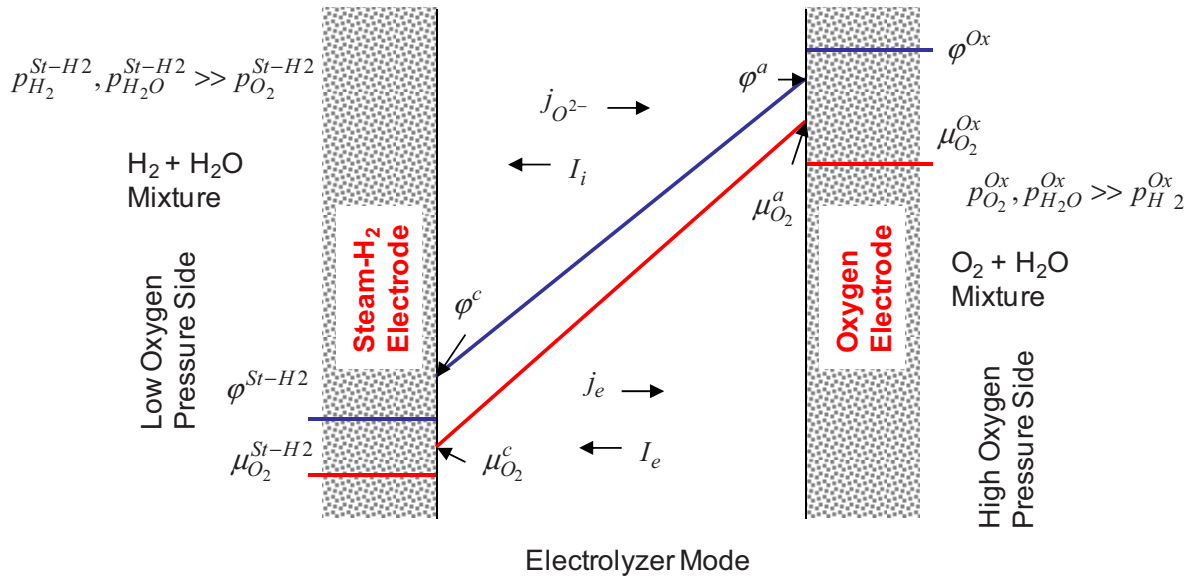


Figure 10. Schematic variations of electric potential (φ) and oxygen chemical potential (μ_{O_2}) through the electrolyte in the electrolyzer mode.

3.2.4 Relative Magnitudes of Transport Numbers and the Development of High Oxygen Pressure in the Electrolyte near the Oxygen Electrode

The $p_{O_2}^{Ox}$ is on the order of 1 atm in the electrolyzer mode. While no definite information is available concerning above what internal pressures delamination is likely (along the oxygen electrode/electrolyte interface), let us assume that delamination will occur if $p_{O_2}^a$ exceeds 100 atm. Fracture mechanical analysis of brittle materials shows that this value of internal pressure at a subsurface defect (e.g., a pore) in the electrolyte just near the electrolyte/electrode interface is generally sufficient to cause significant enhancement in stress because of stress concentration and free surface effects to cause local cracking.³⁸ This suggests that at a typical temperature of electrolysis of 800°C, for values of

$$\left\{ \frac{E_A r_e^a}{R_e} - \frac{(E_A - E_N) r_i^a}{R_i} \right\} < -0.106 \text{ V} \quad (3-36)$$

(corresponding to $p_{O_2}^a = 100 \text{ atm.}$) delamination may occur along the oxygen electrode/electrolyte interface. Actually, high pressure develops in the electrolyte just near the oxygen electrode. The electrolyte/electrode interface is essentially the weak link. Thus, delamination occurs along the oxygen electrode/electrolyte interface.

This is quite a remarkable result since it shows that delamination may readily occur at the oxygen electrode/electrolyte interface at an applied voltage beyond a certain value. Equation 3-36 allows one to estimate what should be the magnitudes of transport parameters so that delamination does not occur. Note

that if $\left\{ \frac{E_A r_e^a}{R_e} - \frac{(E_A - E_N) r_i^a}{R_i} \right\}$ never becomes negative, delamination will not occur because then the

pressure just inside the electrolyte will be lower than $p_{O_2}^{Ox}$. This refers to the values of applied voltage greater than the Nernst voltage; that is $E_A > E_N$. The preceding discussion thus shows that if

$$\left\{ \frac{E_A r_e^a}{R_e} - \frac{(E_A - E_N) r_i^a}{R_i} \right\} \geq 0 \quad (3-37)$$

or if

$$\frac{\left(\frac{r_e^a}{R_e} \right)}{\left(\frac{r_i^a}{R_i} \right)} = \frac{r_e^a R_i}{r_i^a R_e} = \frac{\left(\frac{r_e^a}{r_e^c + r_e^{el} + r_e^a} \right)}{\left(\frac{r_i^a}{r_i^c + r_i^{el} + r_i^a} \right)} \geq \frac{E_A - E_N}{E_A} \quad (3-38)$$

or if

$$E_A < \frac{E_N}{\left(1 - \frac{r_e^a R_i}{r_i^a R_e} \right)} \quad (3-39)$$

delamination will not occur, which means that a *relatively* high value of r_e^a and a *relatively* low value of R_e are preferred. Note that $\frac{r_e^a}{R_e} < 1$ and $\frac{r_i^a}{R_i} < 1$.

How best to achieve this? The following discussion is presented assuming the electrolyte is YSZ. It is well known that YSZ has a very low electronic conductivity at 800°C; in fact, it is virtually immeasurable. Thus, R_e is very high and it must be lowered to prevent high pressure buildup. If the YSZ electrolyte is doped with ceria (or some other oxide capable of creating some electronic conduction in YSZ) it will lower the r_e^{el} by introducing electronic conduction in YSZ and this should lower R_e . If a

small amount of CeO₂ is added to YSZ, it virtually does not change its oxygen ion concentration. Thus, it also does not appreciably change $\mu_{O^{2-}}(\vec{r})$. However, a small amount of CeO₂ will change electron concentration orders of magnitude (but still in the dilute solution limit), and thus will increase the local Fermi level, $\mu_e(\vec{r})$. Referring now to Equation 3-12, note that an increase in $\mu_e(\vec{r})$ is compensated for by a corresponding decrease in $\mu_{O_2}(\vec{r})$ (and thus also a decrease in $p_{O_2}(\vec{r})$) to maintain local equilibrium. This is the role of CeO₂ as an additive to the electrolyte in lowering internal pressure and thus lowering the propensity for oxygen electrode delamination.

If a thin (may be a micron or even a fraction of a micron) layer of YSZ (or some other oxygen ion conductor with a very low electronic conductivity) is now deposited on the electrolyte (on the oxygen electrode side), it will drastically increase r_e^a . In this manner, it may be possible to achieve

$$\frac{r_e^a}{R_e} = \frac{r_e^a}{r_e^a + r_e^{el} + r_e^c} \text{ close to one if } r_e^a \gg r_e^{el}, r_e^c. \text{ It is also preferred that } \frac{r_i^a}{R_i} \text{ be as small as possible.}$$

That is, the charge transfer resistance or the polarization resistance at the oxygen electrode/electrolyte interface should be as small as possible, while the electronic resistance at the oxygen electrode/electrolyte interface should be as large as possible.

Finally, it may also be desirable to have a somewhat higher electrolyte resistance, r_i^{el} . This is an interesting result because it suggests that making too thin a YSZ electrolyte may actually slightly increase propensity to electrode delamination. Naturally, the electrolyte cannot be too thick because the performance will be compromised and may also increase tendency for electrode delamination related to operating conditions as is discussed later. Thus, the main focus should be on lowering the charge transfer (polarization) resistance at the perovskite anode (oxygen electrode)/electrolyte interface, and increasing the electronic resistance at the same interface. Materials such as LSCF developed for SOFC oxygen electrode (cathode) may be ideal for the electrolyzer oxygen electrode (anode). However, one needs to make sure that the polarization resistance is low for the $O^{2-} \rightarrow \frac{1}{2}O_2 + 2e^-$ (oxidation) reaction, which is opposite to the SOFC cathode reaction (opposite to the oxygen reduction reaction). A point to note is that it is not at all obvious that the polarization resistance would be the same in both directions (oxidation vs. reduction) and may need to be separately determined.

3.2.5 Example Calculations

Sample calculations are given below that demonstrate the profound role of electronic conduction through the electrolyte/cell on the magnitude of oxygen pressure generated in the electrolyte just near the anode (oxygen electrode)/electrolyte interface in the electrolyzer mode (that is in the electrolyte near the oxygen electrode/electrolyte interface). No parametric data are available on the YSZ-based system to the author's knowledge.^e However, earlier work from the author's group (Lim and Virkar³⁹) gives some information on the various transport parameters for a gadolinia-doped ceria (GDC)-based cell tested as a fuel cell. Thus, these values are used for illustrative calculations in what follows.

e. Note that we need r_e^a , r_i^a , R_e and R_i for estimating the parameter $\frac{r_e^a R_i}{r_i^a R_e}$, which are not known for LSM/YSZ/Ni or any other YSZ-based system. The only data available are from Lim and Virkar³⁹ for a GDC-based system.

3.2.5.1 Development of High Pressures in the Electrolyte just near the Oxygen Electrode/Electrolyte Interface

Experimental work on GDC electrolyte, anode-supported fuel cells showed that the area specific resistances for both ion transfer and electron transfer across the Ni/Ni+GDC interface are negligible.³⁹ In the electrolyzer mode, Ni + GDC would be the cathode. Assuming the same parameters in the electrolyzer mode, area specific ionic and electronic resistances will be, $r_i^c \approx 0$ and $r_e^c \approx 0$. The area specific ionic and electronic resistances at the $\text{La}_{0.8}\text{Sr}_{0.2}\text{CoO}_3$ (LSC) + GDC/GDC interface in the SOFC mode were measured as $0.3 \Omega\text{cm}^2$ and $1.5 \Omega\text{cm}^2$, respectively.³⁹ If the same values can be assumed in the electrolyzer mode, this would mean $r_i^a \approx 0.3 \Omega\text{cm}^2$ and $r_e^a \approx 1.5 \Omega\text{cm}^2$. The ionic area specific resistance of the electrolyte was estimated as $r_i^{el} \approx 0.09 \Omega\text{cm}^2$.³⁹ The cell area specific ionic resistance is thus $R_i = 0.3 + 0.09 + 0.00 = 0.39 \Omega\text{cm}^2$. The above values are used in the following calculations. Another necessary parameter is the electronic resistance of the electrolyte. This will be treated as a floating parameter that will be varied over a wide range. For the purposes of illustration, the electronic area specific resistance of the electrolyte is varied between, $r_e^{el} = 0 \Omega\text{cm}^2$ and $r_e^{el} = 20 \Omega\text{cm}^2$ in the following calculations.^f For a 10-micron-thick electrolyte, this corresponds to an electronic resistivity as high as $2 \times 10^4 \Omega\text{cm}$ (corresponding to $r_e^{el} = 20 \Omega\text{cm}^2$). This means the R_e^g is varied between $1.5 \Omega\text{cm}^2$ and $21.5 \Omega\text{cm}^2$. Low values of electrolyte electronic resistance, r_e^{el} , in practice can be achieved by adding a small amount of a transition metal oxide or an oxide with cation exhibiting multiple valence states; e.g. CeO_2 to the electrolyte. The temperature is selected as 800°C . The oxygen partial pressures at the electrodes are selected as follows: $p_{\text{O}_2}^{\text{St-H}_2} = 10^{-20}$ atm and $p_{\text{O}_2}^{\text{Ox}} = 1$ atm. These correspond to a Nernst voltage of $E_N = 1.0645$ V. The applied voltage for this calculation is set at $E_A = 1.5$ V. Thus, the corresponding $\frac{E_A - E_N}{E_A}$ ratio is 0.2903. The corresponding ionic current density is estimated as $I_i = -\frac{(E_A - E_N)}{R_i} = -1.117 \text{ Acm}^{-2}$. This value is a measure of the electrolysis current (which corresponds to the hydrogen generation rate). Efficiency of electrolysis is defined as $\frac{I_i}{I} \times 100$. Since the membrane has some electronic conductivity, the process is not 100% Faradaic. This value is different from the ionic transference number of the cell, which is given by $t_i = \frac{R_e}{(R_i + R_e)}$. Finally, another measure of the efficiency of electrolysis is $I_i / (2FE_A I)$ in units of moles of H_2 produced per Joule of electrical energy supplied. These values are also listed in Table 1.

f. Note that even though the lowest value of r_e^{el} chosen is $0 \Omega\text{cm}^2$, this corresponds to total cell electronic resistance R_e of $1.5 \Omega\text{cm}^2$. That is, even in this case, the cell is a predominantly ionic conductor.

g. Note that the cell area specific ionic resistance, R_i , is $0.39 \Omega\text{cm}^2$, which is much smaller than the cell electronic area specific resistance, R_e . Thus, typical measurements by techniques such as impedance spectroscopy or voltage vs. current plots will reflect a somewhat smaller value than $\sim 0.39 \Omega\text{cm}^2$.

Using Equation 3-31, the $p_{O_2}^a$ is estimated for the various values of r_e^{el} selected (and given as a function of $\frac{r_e^a R_i}{r_i^a R_e}$). The ionic transference number for the cell, given by $t_i = \frac{R_e}{(R_i + R_e)}$ is also estimated. Table 1 lists the results of calculations. As the electronic resistance of the electrolyte, r_e^{el} , is varied between zero and $20 \Omega\text{cm}^2$, the cell *electronic resistance* varies between $1.5 \Omega\text{cm}^2$ and $21.5 \Omega\text{cm}^2$, the corresponding $\frac{r_e^a R_i}{r_i^a R_e}$ varies between 1.3 and 0.091 (the corresponding measured cell area specific resistance from voltage vs. current curves varies between $\sim 0.31 \Omega\text{cm}^2$ and $\sim 0.383 \Omega\text{cm}^2$), and the corresponding $p_{O_2}^a$ varies between $\sim 8.45 \times 10^{-17}$ atm. (for $\frac{r_e^a R_i}{r_i^a R_e} = 1.3 > \frac{E_A - E_N}{E_A} = 0.2903$) and $\sim 2.3 \times 10^4$ atm. (for $\frac{r_e^a R_i}{r_i^a R_e} = 0.091 < \frac{E_A - E_N}{E_A} = 0.2903$).

This is a remarkable result which shows that changes in electronic conduction characteristics of the cell, which make modest changes in the overall cell resistance as would be measured from voltage vs. current density plots or impedance spectra ($\sim 0.383 \Omega\text{cm}^2$ to $\sim 0.31 \Omega\text{cm}^2$), can change the pressure generated in the electrolyte just near the oxygen electrode/electrolyte interface by several orders of magnitude. There is no conceivable way that the cell/material can withstand such high internally generated pressures. The conclusion is that under such conditions (high electronic resistance of the electrolyte), delamination along the oxygen electrode/electrolyte interface is imminent and cannot be avoided. In fact, it may be reasonably be expected that delamination will occur above some value of internal pressure ($p_{O_2}^a$) which is much lower than this value, perhaps say 100 atm. Details of the nature of the interface, defects present, electrode microstructure, and general mechanical properties will determine the pressure above which delamination will occur.^h *The key conclusion is that no matter what the mechanical properties are, high enough pressures will most certainly be developed to cause oxygen electrode delamination at values of electronic resistance sufficiently high.* Indeed, experimental results in several studies have shown that delamination often occurs along the oxygen electrode/electrolyte interface in the electrolyzer mode.^{1,16,17,18,19}

This is an additionally remarkable result, as it suggests that the intuitively obvious approach of trying to develop an electrolyte material with the highest possible ionic transference number may in fact be counterproductive from the standpoint of stability. Table 1 shows that delamination is likely for $R_e \geq 9.5 \Omega\text{cm}^2$ for this set of calculations. For a 10-micron-thick electrolyte, this corresponds to $\rho_{el} = 8 \times 10^3 \Omega\text{cm}$ or $\sigma_{el} = 1.25 \times 10^{-4} \text{Scm}^{-1}$, which also means delamination is likely for a 10-micron-thick electrolyte with electronic conductivity less than $1.25 \times 10^{-4} \text{Scm}^{-1}$. Note that in YSZ, the electronic conductivity is much lower than $1.25 \times 10^{-4} \text{Scm}^{-1}$ at 800°C . Thus, electrode delamination is highly likely at 800°C with YSZ as the electrolyte for the operating parameters selected in these calculations. Thus, a small amount of electronic conduction through the electrolyte is actually beneficial.

h. Some defects are almost always present. Note, however, degradation by delamination is expected even if no defects are present, since the cohesive strength of most materials is about 10% of the Young's elastic modulus (which is typically $\sim 10^5$ atm). Thus, internally generated pressures on the order of 10^4 atm. (or greater) will cause cracking (delamination), regardless of the presence of any defects (which are always present).

Table 2. Estimation of oxygen pressure within the electrolyte just near the oxygen electrode (anode)/electrolyte interface, $p_{O_2}^a$, for various values of cell area specific electronic resistance, R_e . The applied voltage is $E_A = 1.5$ V.

r_e^{el} ($\Omega \text{ cm}^2$)	R_e ($\Omega \text{ cm}^2$)	R_i ($\Omega \text{ cm}^2$)	$\frac{r_e^a R_i}{r_i^a R_e}$	$\frac{E_A - E_N}{E_A}$	t_i	I_i (A cm^{-2})	I_e (A cm^{-2})	I (A cm^{-2})	$\frac{I_i}{I} \times 100 \left(\frac{I_i}{2FIE_A} \right)$ (Mols/Joule)	$p_{O_2}^a$ (atm)	Likelihood of Delamination
0	1.50	0.39	1.3	0.2903	0.793	-1.117	-1.0	-2.117	52.8% (1.83×10^{-6})	8.45×10^{-17}	No Delamination
1	2.50	0.39	0.78	0.2903	0.865	-1.117	-0.6	-1.717	65% (2.248×10^{-6})	4.64×10^{-4}	No Delamination
2	3.50	0.39	0.55	0.2903	0.899	-1.117	-0.43	-1.547	72.2% (2.49×10^{-6})	2.67×10^{-5}	No Delamination
5	6.50	0.39	0.3	0.2903	0.943	-1.117	-0.23	-1.347	82.9% (2.86×10^{-6})	1.44	No Delamination
6	7.50	0.39	0.26	0.2903	0.95	-1.117	-0.2	-1.317	84.8% (2.93×10^{-6})	8.63	Delamination Possible
8	9.50	0.39	0.205	0.2903	0.96	-1.117	-0.158	-1.275	87.6% (3.027×10^{-6})	104.6	Delamination Highly Likely
20	21.50	0.39	0.091	0.2903	0.982	-1.117	-0.07	-1.187	94.1% (3.251×10^{-6})	2.3×10^4	Delamination Imminent

The illustrative calculations given here suggest that one should be able to achieve a reasonably high ionic transference number for the membrane while also ensuring stability against delamination and cell degradation. For example, for the values selected here, an r_e^{el} of $\sim 5 \text{ } \Omega\text{cm}^2$ leads to a cell transference number of ~ 0.943 (which means electrolysis efficiency defined here as $\frac{I_i}{I} \times 100$ of 82.9%) and the corresponding $p_{O_2}^a$ is only $\sim 1.44 \text{ atm}$, and should not lead to degradation. Calculations given here are for illustrative purposes only. It is a straightforward matter to recognize that significant optimization of parameters is possible which will not only allow the attainment of a high overall ionic transport number (high electrolysis efficiency), but will also ensure that high internal pressures are not developed under normal electrolyzer operating conditions, thus preventing electrode delamination/degradation. If all relevant parameters are known (which can be experimentally measured), Equations 3-30 and 3-31 may be used to design membranes that will not degrade.

The preceding discussion is given in terms of the required cell transport parameter, namely $\frac{r_e^a R_i}{r_i^a R_e}$, which must be greater than a given operating conditions parameter, namely $\frac{E_A - E_N}{E_A}$, so that oxygen electrode delamination does not occur. This means that if a given set of operating conditions are selected, namely E_N and E_A , then those cells (materials and microstructures, for example) for which $\frac{r_e^a R_i}{r_i^a R_e}$ satisfies the required criteria will not degrade, while those that do not satisfy the required criteria will likely degrade. Alternatively, for a given set of cells, there will be a critical value of $\frac{E_A - E_N}{E_A}$ describing the operating conditions, which should not be exceeded. That is, for a given cell, one must have $\frac{E_A - E_N}{E_A} \leq \frac{r_e^a R_i}{r_i^a R_e}$ or $E_A < \frac{E_N}{\left(1 - \frac{r_e^a R_i}{r_i^a R_e}\right)}$ to prevent oxygen electrode delamination. Since $R_i = r_i^c + r_i^{el} + r_i^a$ and $R_e = r_e^c + r_e^{el} + r_e^a$, multiple options exist to select the various transport parameters such that the delamination of oxygen electrode may be prevented.

An important consequence of non-equilibrium thermodynamics is the occurrence of abrupt changes in potentials (chemical and/or electrical) across interfaces.^{7,27,30,40} If the interface is modeled as a thin transition region—perhaps a few nanometers or even a fraction of a nanometer—all changes in the transition region are naturally continuous. However, on a microscopic scale (or even at a submicroscopic scale), smooth changes occur in regions adjacent to the interfaces and sharp changes occur through the interfaces, as has also been shown by non-equilibrium molecular dynamics simulations.^{30,40} Thus, the existence of a very high $\mu_{O_2}(\vec{r})$, which is $\mu_{O_2}^a$ (or $p_{O_2}(\vec{r})$, which is $p_{O_2}^a$) in the electrolyte just near the oxygen electrode; and low $\mu_{O_2}(\vec{r} + \vec{\delta r})$, which is $\mu_{O_2}^{Ox}$ (or $p_{O_2}(\vec{r} + \vec{\delta r})$, which is $p_{O_2}^{Ox} \sim 1 \text{ atm.}$) in the oxygen electrode, just across the electrolyte/electrode interface, is perfectly reasonable. Here, $\vec{\delta r}$ is the interface thickness.

Figure 11 shows a schematic of the abrupt change in oxygen pressure across an interface. The interface thickness is expected to be very small—perhaps on the order of a nanometer. The high pressure formed just inside the electrolyte links up with the near surface defects causing delamination. As soon as a delamination crack is formed, pressure within the crack rapidly reduces to that close to the $p_{O_2}^{Ox}$.

The initiation of delamination cracks can occur at multiple places, and they link up to form a macroscopic crack leading to electrode delamination. Figure 12 shows possible locations at the electrolyte/electrolyte interface where high pressure may build up leading to delamination. The kinetics of this growth process, however, depends on the net flux of oxygen depositing in the crack, which depends upon the current and the various transport parameters and the operating conditions, as described in earlier work on related topics.^{38,41} Also, if some interdiffusion occurs between the electrolyte and the oxygen electrode, it may alter local transport properties. Under such conditions, it is possible that the initiation of delamination may occur inside the electrolyte some distance from the interface.³⁸

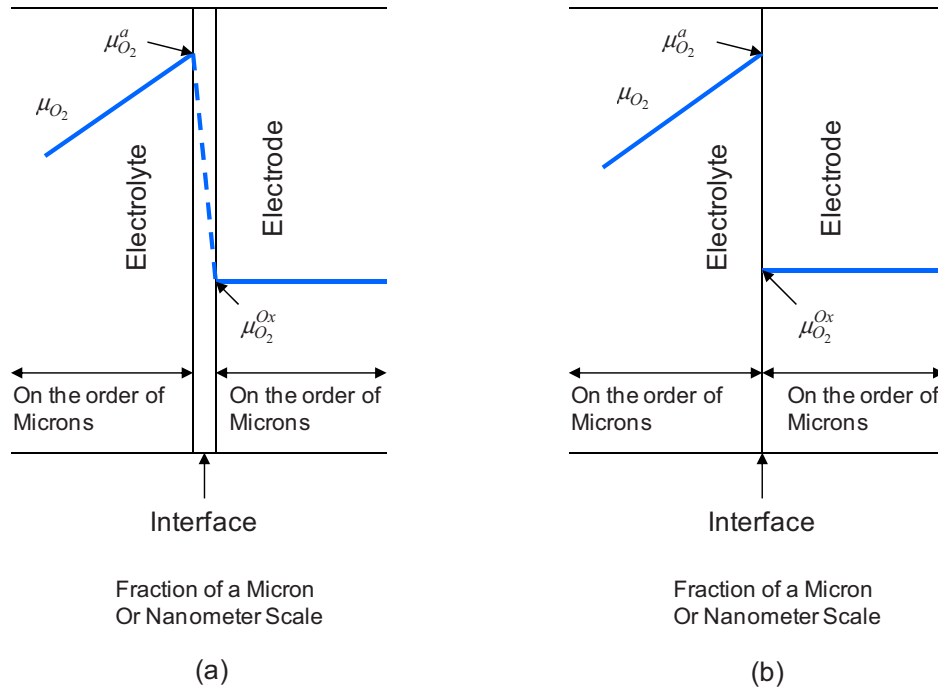


Figure 11. A schematic variation of oxygen chemical potential in the vicinity of the oxygen electrode/electrolyte interface when high oxygen pressure is developed within the electrolyte.

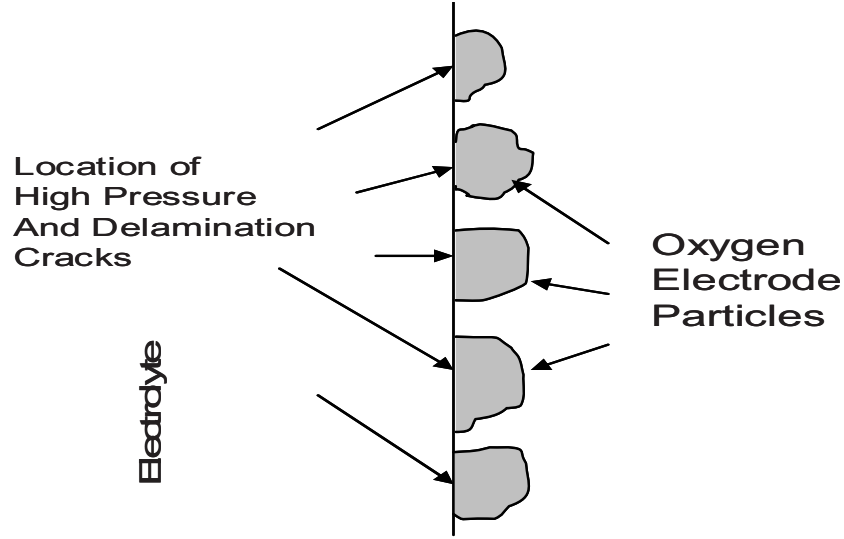


Figure 12. A schematic showing the locations where the high oxygen pressure builds up. Delamination cracks develop at multiple places and then link up to form a macroscopic delamination crack along the oxygen electrode/electrolyte interface.

3.2.5.2 Development of Low Oxygen Pressure within the Electrolyte just near the Steam-H₂ Electrode/Electrolyte Interface

The other possibility for degradation is local electrolyte decomposition if the $p_{O_2}^c$ drops below the decomposition pressure for zirconia. At 1073K, the standard free energy of formation of ZrO₂ is - 894.6 kJ/mol.⁴² This corresponds to an equilibrium oxygen partial pressure of $\sim 2.8 \times 10^{-44}$ atm. Thus, to ensure that decomposition does not occur, $p_{O_2}^c$ must be above this value. The expected value of oxygen partial pressure in the hydrogen being formed at the steam-H₂ electrode is assumed to be 10^{-20} atm or $p_{O_2}^{St-H_2} \sim 10^{-20}$ atm. From Equation 3-30, note that

$$\frac{RT}{4F} \ln \left(\frac{p_{O_2}^{St-H_2}}{p_{O_2}^c} \right) = -\frac{E_A r_e^c}{R_e} + \frac{(E_A - E_N) r_i^c}{R_i} \quad (3-40)$$

Decomposition will occur at the steam-H₂ electrode/electrolyte (YSZ) interface (into the electrolyte), provided the above exceeds 1.25 V at 800°C. Thus, to prevent decomposition, it must have

$$E_A \left(\frac{r_i^c}{R_i} - \frac{r_e^c}{R_e} \right) - \frac{E_N r_i^c}{R_i} = (E_A - E_N) \left(\frac{r_i^c}{R_i} \right) - E_A \left(\frac{r_e^c}{R_e} \right) \leq 1.25 \text{ V} \quad (3-41)$$

If the electrolyte is other than YSZ, Equation 3-41 will be modified according to the corresponding free energy of formation of the oxide. Equation 3-41 shows that $\frac{r_i^c}{R_i}$ should be as small as possible and

$\frac{r_e^c}{R_e}$ should be as large as possible. This means the polarization resistance for the oxygen reduction

reaction (at the steam-H₂ electrode should be as low as possible, and the electronic resistance at the steam-H₂ electrode/electrolyte interface should be as large as possible. The relative magnitudes of the voltage values show, however, that in general, delamination at the oxygen electrode is the likely mode of degradation rather than decomposition at the steam-H₂ electrode/electrolyte interface. This is in accord with the observations in several studies.

3.2.6 SOFC versus SOEC

As shown previously and discussed here, degradation of a single SOFC by delamination is not expected, but that of a single SOEC is possible.²⁷ In an SOFC stack, if a cell imbalance occurs, it is possible to have both ionic and electronic currents in the same direction, which can cause electrode delamination/failure.^{7,27} In this context, degradation of the electrolyzer (SOEC) is much more likely than that of a fuel cell (SOFC) since the ionic and the electronic currents through the cell are *always* in the same direction in the electrolyzer mode. In SOFC, degradation caused by internally generated high pressures occurs because of cell imbalance in a stack.⁷ In SOFC, it has been observed that delamination occurs along the electrolyte/fuel electrode interface.⁴³ Since the partial pressure of oxygen in the Ni + YSZ fuel electrode in SOFC is $\sim 10^{-20}$ atm; a large increase in μ_{O_2} is therefore necessary for delamination to occur. By contrast, in SOEC, a relatively modest increase in relation to adjacent gas phase partial pressure of oxygen is required for delamination to occur along the oxygen electrode/electrolyte interface. For this reason, degradation by delamination of the positive (oxygen) electrode is more likely in electrolyzers as compared to the delamination of the negative (fuel) electrode in unbalanced fuel cells in a stack. Indeed, it has been reported that the result of degradation of SOEC is often delamination of the oxygen electrode.^{1,16,17,18,19} Additionally, possible cell imbalance in an SOEC stack may further exacerbate the situation concerning delamination/failure.^{7,43}

3.2.7 Comparison of the Available Experimental Results from the Literature with the Predictions of the Model

Several studies have shown that oxygen electrode delamination occurs in solid oxide electrolyzers under certain operating conditions.^{1,16,17,18,19} There also are some reports of relatively stable operation for several hundred hours.^{44,45,46} The objective of the following discussion is to determine if there were significant differences among the various reported studies in the context of the model described here. Quantitative comparison of the model with the published literature is not possible since the required information on the various transport parameters (r_e^a , r_i^a , R_e , and R_i) is not available. Some information, however, is available, which allows for a qualitative comparison.

Hauch et al.⁴⁴ observed stable performance and no delamination was observed. In their work, the temperature was typically 850°C and in some tests as high as 950°C. At higher temperatures, the electronic conductivity of YSZ is expected to be higher, which would tend to mitigate high pressure generation. The long term test at 850°C was conducted in their work at a current density of -0.5 Acm⁻².

The corresponding E_N and E_A were 0.855 V and 1.14 V. Thus the corresponding $\frac{E_A - E_N}{E_N}$ was 0.25.

An increase in the overall cell resistance was noted in most tests. The various contributions to the cell resistance were obtained by deconvolution of impedance spectra. These authors attributed increase in resistance to the degradation of the steam-H₂ electrode. In the studies by Brisse et al.⁴⁵ tests were conducted at 800 and 900°C. The long-term test (160 h) was conducted at 800°C under an applied voltage of 1.05 V. The corresponding E_N was 0.78 V and the ratio $\frac{E_A - E_N}{E_N}$ was 0.14. In both of these

studies, the ratio $\frac{E_A - E_N}{E_N}$ was lower than used in the calculations presented here (0.2903). While no information is available on $\frac{r_e^a R_i}{r_i^a R_e}$ in either of these tests, lower values of $\frac{E_A - E_N}{E_N}$ are consistent with relatively benign electrolysis conditions, especially the long term test for which $\frac{E_A - E_N}{E_N}$ was 0.14. Thus, the observation that no delamination of the oxygen electrode occurred in their studies, appears to be consistent with the low $\frac{E_A - E_N}{E_N}$ ratio in these studies, indicating relatively benign electrolytic conditions. In another study Doenitz et al.⁴⁶ tested cells at 995°C at a cell voltage E_A of 1.07 V, a Nernst voltage E_N of 0.83 V, and the ratio $\frac{E_A - E_N}{E_N}$ of 0.22. No delamination was reported. In all of their studies, it is thus the expectation that the operating parameter $\frac{E_A - E_N}{E_N}$ was less than $\frac{r_e^a R_i}{r_i^a R_e}$. That is, the conditions were rather benign and no delamination was observed.

In studies conducted by O'Brien et al.¹⁸, by contrast, delamination of the oxygen electrode was observed at the conclusion of the 1000 h test. Throughout the test, increase in cell resistance was observed (from initial $\sim 0.6 \Omega\text{cm}^2$ to $\sim 1.3 \Omega\text{cm}^2$ after 1000 h). The current density at which the test was conducted was not given in the paper. However, the test data given in their¹⁸ Figures 8 and 9 show that $\frac{E_A - E_N}{E_N}$ values may have been more than 0.35 and as high as 0.4. This means electrolysis conditions used in the work by O'Brien et al.¹⁸ were far more severe than used in the studies by Hauch et al.⁴⁴ and Brisse et al.⁴⁵ In the studies by O'Brien et al.,¹⁸ the cells were thick, electrolyte supported. Higher applied voltage, E_A , was probably needed to obtain a reasonable electrolysis current because of the large electrolyte thickness, effectively increasing $\frac{E_A - E_N}{E_N}$ and thus increasing propensity for oxygen electrode delamination. Thus, the observation that oxygen electrode delamination occurred is in accord with the mechanism described here.

In the work by Guan et al.,¹ significant delamination of the oxygen electrode was also observed with LSM + YSZ as the oxygen electrode. The cell voltage E_A was 1.3 V, the Nernst voltage E_N was 0.855 with the corresponding $\frac{E_A - E_N}{E_N}$ of 0.34. Again, comparison with the calculations given here shows that test conditions were rather severe, and the observed electrode delamination is consistent with the predictions of the mechanism presented here.

3.2.8 Transient Effects

This section describes the possible role of transient effects in the context of the proposed model. The preceding analysis assumes the existence of a true steady state. Often, the actual state may be an apparent steady state and in some cases even a clear transient state may exist, as judged on the basis of the time dependence of the externally measured parameters (current and voltage). That is, if a clear transient state exists, then the experimentally measurable parameters such as voltage and current will exhibit time

dependence. A number of phenomena such as electrode microstructure changes, interconnect oxidation, seal degradation, etc., will likely occur over time. For example, it has been observed that many changes such as chromium migration from the interconnect into the electrodes occurs over time. Such changes will alter the transport parameters such as r_e^a , r_i^a , R_e , and R_i , thus altering the tendency for electrode delamination by the mechanism described here. That is, many transient effects will conspire to produce conditions leading to $\frac{E_A - E_N}{E_A} > \frac{r_e^a R_i}{r_i^a R_e}$ and eventually creating conditions ripe for delamination.

If an apparent steady state exists, however, no detectable changes in the measured voltage and current may be observed. That is, the system will appear to have reached a steady state. However, if one independently measures $\phi(\vec{r}, t)$ within the electrolyte, such as by embedded probes,³⁹ one should be able to observe that it changes with time, even when the measured voltage and current do not change with time. Also, when an apparent steady state exists, the $\phi(\vec{r}, t)$ within the electrolyte need not be bounded by values at the electrodes (ϕ^I and ϕ^{II}). Indeed, studies on YSZ-based solid oxide fuel cells have shown that under certain testing conditions, $\phi(\vec{r}, t)$ is often not bounded by values at the electrodes.⁴⁷ In an apparent steady state, Equations 3-18, 3-19, and 3-20 respectively become

$$I_e^c(t)r_e^c(t) = -E^c(t) + I_i r_i^c = \phi^I - \phi^c(t) = \Delta\phi^{I,c}(t) \quad (3-42)$$

$$I_e^{el}(t)r_e^{el}(t) = -E^{el}(t) + I_i r_i^{el} = \phi^c(t) - \phi^a(t) = \Delta\phi^{c,a}(t) \quad (3-43)$$

and

$$I_e^a(t)r_e^a(t) = -E^a(t) + I_i r_i^a = \phi^a(t) - \phi^{II} = \Delta\phi^{a,II}(t) \quad (3-44)$$

such that the sum of the three $\Delta\phi$'s still corresponds to the measured (fixed) voltage across the cell, namely

$$\Delta\phi^{I,c}(t) + \Delta\phi^{c,a}(t) + \Delta\phi^{a,II}(t) = \phi^I - \phi^{II} = -E_A = V \quad (3-45)$$

since

$$V = -E_A = \phi^I - \phi^{II} \quad (3-46)$$

is independent of time, and the measured current, which is essentially I_i , is also nearly independent of time, consistent with an apparent steady state. This case is depicted in Figure 7.

3.2.9 Time Required to Attain Steady State and/or the Condition of Criticality

All of the analysis given in this manuscript is based on the assumption of a true steady state. Within the typical experimental time frame, a true steady state may not be easily attained. An important factor concerns the time required to attain the true steady state, or at least the time required to reach the condition of criticality (as judged on the basis of critical pressure generated to reach a steady state). This time depends on transport parameters and other parameters related to deviations from stoichiometry. These are not known for any system to a reasonable level of accuracy. Nevertheless, the general approach necessary to solve the relevant differential equations has been previously described for a couple of cases.^{7,38,41} The general conclusion is that the greater the overall electronic conductivity, the faster are the kinetics of achieving the steady state.⁴¹ However, as described here, by a suitable choice of transport parameters, it is possible to achieve the final steady state which is subcritical, that is, it does not lead to

degradation. If the electronic conductivity is very low, greater time is required to attain steady state. This will reflect as a larger incubation time before significant degradation may become experimentally detectable (such as increase in the overall resistance). The incubation time depends in a complicated way on a number of transport parameters.^{38,41} However, critical condition may be reached long before the steady state is reached, leading to failure. Thus, from the standpoint of long-term stability, it is preferable to introduce some electronic conductivity so that steady state corresponding to subcritical condition is reached and high pressures are not generated.

3.3 Summary of Thermodynamic Modeling

Based on the model for oxygen electrode delamination in SOECs presented in this report, the following are summary statements that describe essential features of the model, its predictions, and implications concerning the design of robust SOECs.

The model shows that degradation/failure of a SOEC will primarily manifest as delamination along the oxygen electrode/electrolyte interface. Oxygen electrode delamination occurs as a result of the formation of high internal oxygen pressure within the electrolyte, just near the oxygen electrode/electrolyte interface.

The higher the electronic conductivity of the electrolyte (cell), the lower is the tendency for the formation of high internal pressures. Preliminary calculations show that modest changes in electronic conduction can cause orders of magnitude changes in oxygen pressure, $p_{O_2}^a$. Thus, the present analysis shows that a small amount of electronic conduction through the electrolyte is actually preferred from the standpoint of stability. This is a significant result as it suggests that an oxygen ion conductor of the highest possible ionic transport number (negligible electronic transport number) may be more prone to degradation (oxygen electrode delamination) and thus is not the desired material as an electrolyte. In this context, YSZ may not be the ideal material as electrolyte for SOEC, especially at 800°C and lower temperatures.

The addition of a small amount of a transition metal oxide or other oxides with cations exhibiting multiple valence states, such as ceria, to the electrolyte should increase its electronic conductivity and decrease the tendency for the delamination of oxygen electrode. It should be possible to suitably tailor electronic transport through the cell to minimize tendency for high pressure buildup and simultaneously ensure a relatively high ionic transport number for the cell and thus a high electrolyzer efficiency. This can be achieved by depositing a very thin layer of a purely oxygen ion conductor with a high electronic resistance on the base electrolyte on the oxygen electrode side.

The overall propensity for oxygen electrode delamination can be described by a parameter given in terms

of the various transport parameters, namely, $\frac{r_e^a R_i}{r_i^a R_e}$. The higher the $\frac{r_e^a R_i}{r_i^a R_e}$, the smaller is the propensity

for oxygen electrode delamination. In terms of the operating parameters, delamination should not occur as

long as $\frac{E_A - E_N}{E_A} < \frac{r_e^a R_i}{r_i^a R_e}$. Alternatively, the applied voltage must satisfy the following condition,

namely $E_A < \frac{E_N}{\left(1 - \frac{r_e^a R_i}{r_i^a R_e}\right)}$, to prevent oxygen electrode delamination. Experimental methods can be

devised in principle to measure the required cell parameters, namely r_e^a , r_i^a , R_i and R_e ; and identify safe operating regime for SOECs.

4. ATOMIC-SCALE MODELING OF DEGRADATION IN SOLID OXIDE ELECTROLYZED CELLS

(by Sergey N. Rashkeev and Michael V. Glazoff, INL)

4.1 Introduction

To achieve robust SOEC performance targets (current density, tolerable degradation rate, and desired lifetime—about 20,000 hours—for efficient commercial producing large quantities of hydrogen by SOEC stacks), the existing SOEC technology needs to be improved.⁴⁸ Meanwhile, the integrated laboratory-scale test performed at the INL facility showed that a significant degradation of the SOEC stacks occurs over the first 1000 hours.⁴⁹

In order to improve the SOEC technology, one of the most important issue was to understand the degradation mechanisms of the SOEC devices and to find a way to mitigate (and/or significantly slow down) the physical and chemical processes that cause the degradation.

Post-test examination by Ceramatec showed that the hydrogen electrode appeared to be in good condition. The oxygen electrode does show delamination in operation and an apparent foreign layer deposited at the electrolyte interface. Post-test examination by the Argonne National Laboratory showed that the O₂-electrode delaminated from the electrolyte near the edge. One possible reason for this delamination is excessive pressure buildup with high O₂ flow in the over-sintered region. According to results obtained at the Massachusetts Institute of Technology, the electrochemical reactions have been recognized as one of the prevalent causes of their degradation. Specifically, two important degradation mechanisms were examined: (1) transport of Cr containing species from steel interconnects into the oxygen electrode and LSC bond layers in SOECs, and (2) cation segregation and phase separation in the bond layer. Two workshops were organized by INL to discuss possible causes of degradation in a SOEC stack (October 27, 2008, and August 9, 2010). It was generally agreed that the following are major degradation issues relating to SOECs:

- Delamination of the O₂-electrode and bond layer on the steam/O₂-electrode side
- Contaminants (Ni, Cr, Si, etc.) on reaction sites
- Loss of electrical/ionic conductivity of electrolyte.

Research aimed at gaining fundamental understanding of different factors affecting degradation of SOEC devices is presented below. On the basis of this understanding, different possible improvements to the existing SOEC technology are proposed that would help achieving the desirable performance targets for these devices as well as predict and rational design of other high lifetime SOEC devices based on different materials. Heuristic methods are insufficient for fundamental studies of degradation processes in SOEC systems and devices that are initiated and developed at different length scales (including atomic, nano, and micro). A unique combination of different modeling and computational approaches and computer codes is needed to address such a multiscale, interdisciplinary problem. This work applied most contemporary achievements in different scientific areas including computational thermodynamics, diffusion modeling in multicomponent systems, and atomic and electronic structure calculation methods. An effort (based on the modeling) was also initiated to systematically develop SOEC systems with high stability against degradation and to apply this knowledge to real-life devices.

The research work was concentrated around several main problems, namely:

1. Thermodynamic and diffusion modeling for steels (including ferritic 441 steel) used for SOEC interconnects.
2. Atomic-scale mechanisms of Cr poisoning and its mitigation/inhibition by using coating layers.
3. Understanding atomic mechanism of oxygen delamination and studying different ways for its mitigation.
4. Identifying modeling based engineering solutions that will help improve operation of the SOEC devices up to the point when they will become economically feasible.

4.2 Methods of Modeling: Atomic-scale Calculations, Thermodynamics, Phase Equilibria, and Diffusion Modeling

SOEC materials (electrodes, electrolyte, steel interconnects, etc.) have to function in a very aggressive environment: at temperatures up to 850°C, in corrosive oxygen, hydrogen, and water vapor atmosphere in the presence of electric fields. It is critical to make sure that materials used for the SOEC devices (in this case, porous LSM) anode, nickel-zirconia cermet cathode, YSZ electrolyte, and ferritic steel interconnects) as well as their surfaces and interfaces do not undergo phase transformations or diffusion related changes of chemical composition resulting in their degradation and loss of functionality.

The problem of material degradation in SOEC systems cannot be resolved successfully without a fundamental understanding of atomic and nanoscale defects, phase equilibria, complex diffusion-induced processes, and electrochemical phenomena. One of the goals was to understand, and consequently control, a number of degradation issues associated with phase decomposition and diffusion-induced phase transformations in SOEC. For that goal, two novel advanced modeling tools were used: Thermo-Calc and DICTRA. A brief description of all of the used modeling approaches and their role in understanding the SOEC materials and devices is described below.

4.2.1 First-principles Calculations and Atomic-scale Modeling

Degradation processes in materials systems typically start with individual atomic-scale defects that are formed, interact with each other, and form different defects, instabilities, and imperfections at larger length scale, etc. Therefore, any serious study of degradation processes in materials and devices should start with atomic-scale investigations of point (localized in all the three dimensions) defects. Calculations of defects and defect processes in materials have to account accurately for several physical phenomena such as trapping of electronic charge, mechanisms of defect formation, defect induced relaxation, photo-induced excitations and formation of transient species.

Three models are usually used in calculations. In the periodic model a fragment of a material (supercell) is selected and translated periodically in three dimensions. In a molecular cluster model a finite fragment of material (cluster) is used to model the defect and its nearest environment. Both schemes have their pros and cons. The third (embedded cluster) model attempts to combine the advantages of both of them. In this case a defect with its nearest environment is considered using a high-level theory (usually *ab initio* methods). At the same time, the effect of the remaining part of the system is taken into account using a less accurate method, e.g., classical interatomic potential. One of such schemes has been pioneered at University College of London and is now implemented is a computer code GUESS (Gaussians Used for Embedded System Studies).⁵⁰

Using first-principles, self-consistent, density-functional based electronic structure calculations, the formation energies and migration barriers were calculated for several different defects in solid solutions corresponding to the materials and interfaces used in SOECs. In particular, the role of different point defects (vacancies, single impurities, interstitials, etc.) in degradation of bulk materials and interfaces was

investigated. Future plans are to investigate the role of extended defects (voids, dislocation cores, etc.) in the processes of transport and trapping of different atoms at interfaces (e.g., at the anode-electrolyte interface). Some calculations were performed for large clusters using the Gaussian 09 codes.⁵¹ Most of the calculations were performed for large periodic supercells (using plane waves and pseudopotentials implemented in the Vienna Atomic Simulation Program [VASP]) codes.^{52,53,54} The most recent version of the VASP codes (VASP.5.2) has a significant number of different useful options such as hybrid density functionals and the GW approximation method for excited electronic states, which provide an opportunity to perform very accurate and reliable calculations for different defects. Values calculated from first-principles for parameterization the Kinetic Monte Carlo (KMC) codes will be used for calculating different transport coefficients. Some molecular dynamics (MD) modeling using the LAMMPS codes developed at the Sandia National Laboratory will also be used if necessary.

All the tools for performing electronic structure calculations and atomic-scale simulations are available at INL. The codes are implemented at the massive parallel clusters (helios and icestorm) at the INL High Performance Computer Center. They were already successfully used for modeling the SOEC related materials and interfaces.

4.2.2 Thermodynamics and Phase Equilibria

One mechanism of the SOEC degradation might be related to a simple phase decomposition of the materials used for the SOEC electrodes, electrolyte, and interconnects (especially at different interfaces) because of the lack of thermodynamic stability at the operating conditions. This statement could be verified if systematic modeling (performed in a close collaboration with experimental work) were conducted on the construction of phase diagram isotherms and isopleths for all materials of interest. Self-consistent modeling of thermodynamic properties and phase equilibria of materials was conducted using the Thermo-Calc code—an equilibrium thermodynamics tool specifically developed for such applications. It is based on the classical thermodynamics of heterogeneous equilibria^{55,56,57} and was realized in Sweden.^{56,58} In order to make this program work, it is also necessary to provide it with thermodynamic and/or existing experimental phase equilibria data. These data come in the form of different proprietary and public databases. In those cases when the necessary information is absent, it needs to be generated using first-principles atomistic simulations.⁵⁹

Thermo-Calc calculations are based on the principle of finding a global equilibrium among all possible competing phases at given conditions. The connection between phase diagrams and thermodynamic properties of materials is established via the principle of Gibbs' tangent plane construction: when it circumvents the “cups” of thermodynamic potentials of competing phases, the project of the traces of figurative points where the plane has actually touched the potential surfaces onto the “T-x” plane, represents the corresponding phase diagram.

The type of material degradation processes considered above is associated with complete loss of thermodynamic stability of materials, e.g., when the coefficients of chemical, mechanical, and thermal stability become equal to zero. An example of such phase transformation is spinodal decomposition.⁶⁰ In this case, no external forces are required to cause material degradation. However, this is not the only mechanism that could be operable in an SOEC. Other mechanisms might include diffusion-induced phase transformations, when the diffusion of a certain chemical element into (or out of) material may result in phase transformations and material degradation.

4.2.3 Diffusion Modeling

Problems of this type could be handled with a computational tool called DICTRA (Diffusion-Controlled Transformations). This is a sister software of the thermodynamic program “Thermo-Calc;” it was also developed at KTH (Royal Institute of Technology, Stockholm, Sweden) under the guidance of Prof.

Mats Hillert. This software was used, in application to the SOEC material degradation problem, to select a suitable coating material for the 441 ferritic steel interconnects, which may otherwise poison electrodes, electrolyte, and bond layer materials by gaseous chromium species released from stainless steel materials at 800°C in the presence of water vapor.

Dictra code operates in the following way.⁶¹ After each diffusion step, the equilibrium corresponding to the new average composition is calculated at every spatial point inside the considered system, and the corresponding equilibrium calculations are made anew using the Thermo-Calc software.⁶² This procedure ensures that all composition and phase-fraction profiles are updated. The diffusion step is then repeated with the new composition profiles in the matrix, and so on. It should be understood that the dispersed particles will affect the diffusivity through the material; this problem could be treated separately if necessary.⁶³

It is very important to mention that Dictra works in tandem with Thermo-Calc: under the assumption of local equilibrium at every step, it computes the chemical potential gradients (second derivatives of the Gibbs potential) and makes a one-time step forward. Consequently, it needs data on equilibrium thermodynamics of systems under consideration, as well as the corresponding atomic mobilities. For steels, both types of databases are readily available and were acquired along with the computational tools. However, for oxides and perovskites (the use of these materials is critically important for the SOEC functionality), any mobility databases are absent and need to be developed. This should be done using first-principles atomistic calculations and atomic-scale modeling. In particular, the diffusivity matrix should be constructed by combined efforts of searching the existing literature on oxides and perovskites as well as by performing atomic-scale modeling (MD and KMC) for these ceramics. Kinetic modeling will also help to optimize the materials and coatings by minimizing all the undesirable transport processes (e.g., Cr transport from steel interconnects) in the SOEC systems.

Combined atomic scale, thermodynamic, and kinetic modeling will eventually provide practical recommendations on how to modify the SOEC multicomponent systems to minimize Cr transport, oxygen delamination, and other undesirable processes, thus increasing the lifetime of SOEC devices and making it possible to use them in industrial and/or commercial applications.

INL has started to operate several powerful tools (Thermo-Calc, Dictra, VASP, GUESS, Gaussian, LAMMPS, etc.).

4.3 Results

4.3.1 Diffusion Modeling of Coating for 441 Ferritic Steel to Prevent Electrolyte Cr Poisoning

Different types of steels are conveniently compared at the plot shown in Figure 13. Ferritic stainless steels (400 series), have chromium as their major alloying element and are typically low in carbon content. Ductility and formability are less than while corrosion resistance of 441 is similar to austenitic grades. Typically, such materials find widespread applications for automotive exhaust systems, catalytic converters, chimney liners, etc.⁶⁴

Composition

	1.4509 DIN (441) Specification*	Typical AK Steel 441
	%	%
Carbon	0.03 max	0.012
Manganese	1.00 max	0.30
Phosphorus	0.04 max	0.023
Sulfur	0.015 max	0.001
Silicon	1.00 max	0.35
Chromium	17.5-18.5	18.0
Columbium	9xC + 0.3 to 1.00	0.45
Titanium	0.1-0.6	0.17

*Believed to be accurate DIN specifications for 1.4509.

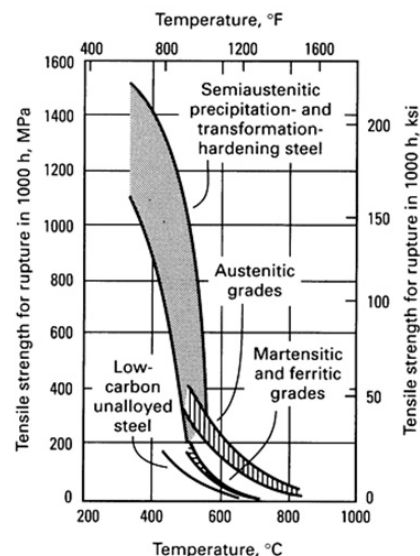


Figure 13. Chemical composition of 441 stainless steel (left) and tensile strength for rupture in 1000 hours as a function of temperature for different types of steels (right).⁶⁴

Several candidate materials were considered as suitable coatings for 441 stainless steel, including nickel, copper, and some spinel materials.^{65,66,67,68,69} In order to study the diffusion resistance of a coating material to the penetration of chromium, it was necessary to characterize the phase composition of the 441 stainless steel first. This was done by Thermo-Calc codes using single-point phase equilibrium calculation (Figure 14), assessment of the relative volume fractions of different phases (Figure 15), and property diagrams called isopleths (corresponding to the case when the concentration of only one component of the alloy changes while all of the others concentrations are kept constant, as shown in Figures 16 and 17).

C	5.4930E-04	1.2000E-04	4.2771E-06	-1.1029E+05	SER
CR	1.9033E-01	1.8000E-01	4.2955E-03	-4.8624E+04	SER
FE	7.9465E-01	8.0718E-01	4.1519E-03	-4.8927E+04	SER
MN	3.0023E-03	3.0000E-03	8.3227E-06	-1.0435E+05	SER
NB	2.6630E-03	4.5000E-03	2.5417E-06	-1.1493E+05	SER
SI	6.8515E-03	3.5000E-03	2.7136E-10	-1.9652E+05	SER
TI	1.9521E-03	1.7000E-03	2.1290E-07	-1.3706E+05	SER
BCC_A2#1	STATUS ENTERED		Driving force 0.0000E+00		
Number of moles 9.9425E-01, Mass 5.4637E+01					
Mass fractions:					
FE 8.09586E-01	MN 3.01879E-03	C 1.64494E-07			
CR 1.81055E-01	NB 1.76487E-03				
SI 3.33400E-03	TI 1.24073E-03				
FCC_A1#2	STATUS ENTERED		Driving force 0.0000E+00		
Number of moles 1.1886E-03, Mass 4.8312E-02					
Mass fractions:					
NB 4.73046E-01	CR 1.28221E-04	SI 3.72108E-13			
TI 3.90449E-01	MN 7.47507E-08				
C 1.36376E-01	FE 1.81583E-08				
LAVES_PHASE_C14#1	STATUS ENTERED		Driving force 0.0000E+00		
Number of moles 4.5653E-03, Mass 2.9448E-01					
Mass fractions:					
FE 4.93198E-01	TI 2.31349E-02	C 0.00000E+00			
NB 4.35098E-01	CR 1.36910E-02				
SI 3.48726E-02	MN 5.46999E-06				

Figure 14. Single equilibrium calculations for Ferritic steel 441 at 1073°F (800°C).

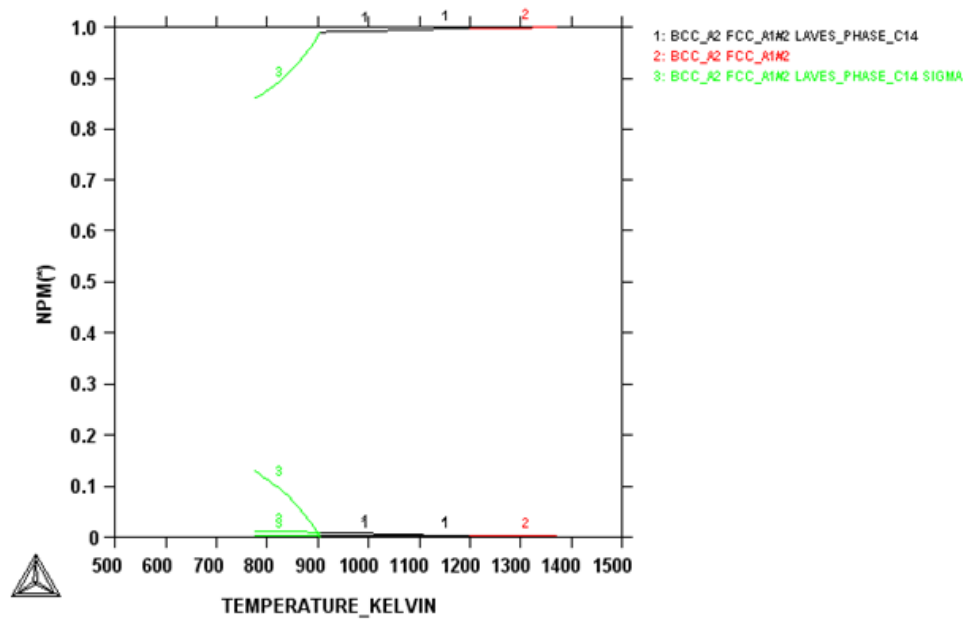


Figure 15. Mass-fractions of equilibrium phases in steel 441 as a function of temperature.

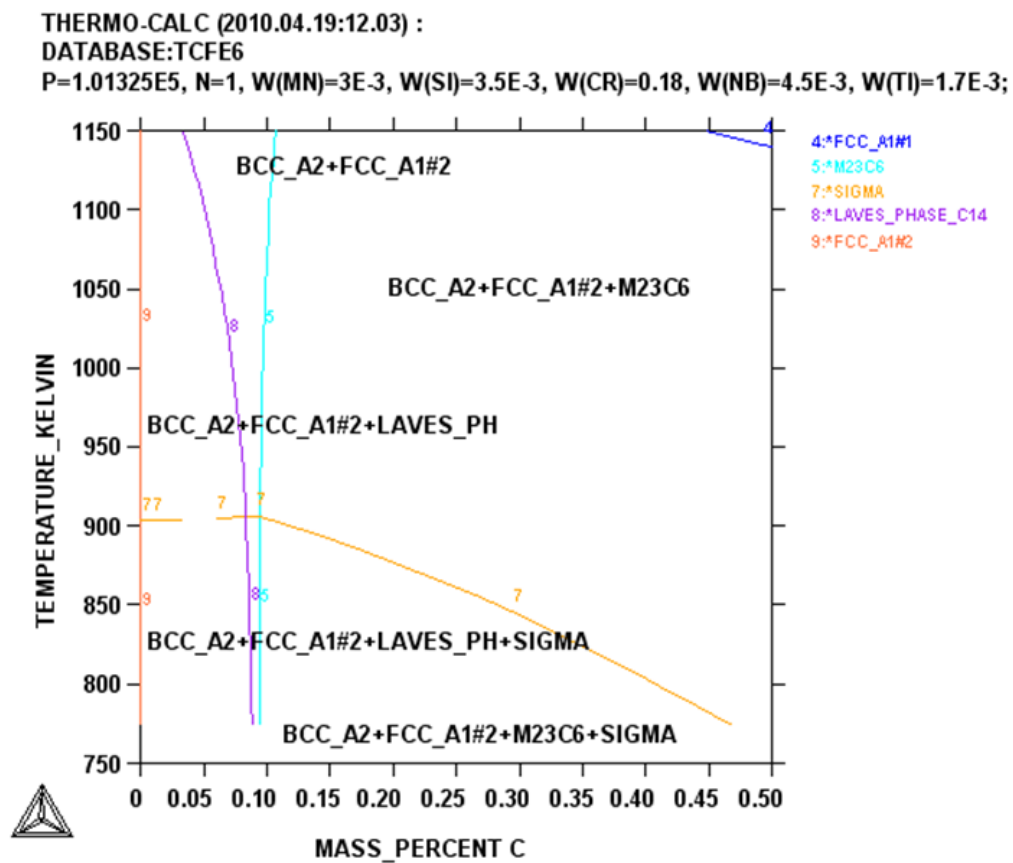


Figure 16. Carbon-isopleths for stainless steel 441, confirming that the equilibrium phase composition of 441 steel at 800°C is body centered cubic (bcc)-matrix, face-centered cubic (fcc)-strengthening precipitates, and a small amount of the Laves phase.

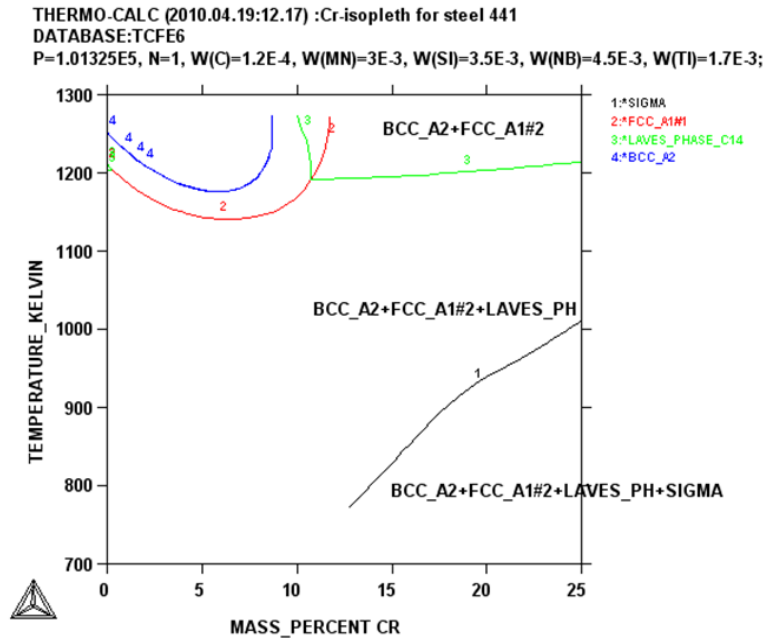


Figure 17. Chromium isopleths for steel 441, confirming the results shown in Figures 15 and 16.

Understanding of phase composition and microstructure of stainless steel was obtained using Thermo-Calc codes, then proceeded to diffusion calculations with DICTRA codes. First, it was decided to study the 441/Ni system, based on the results obtained in the literature; also this was the simplest possible case for a computational study. However, even in this case, numerical instabilities arose resulting from the need to describe the fcc/bcc contact between Ni and 441. The modeled configuration represented a slab comprised of 200 μm of 441 and 50 μm of Ni.

Figure 18 represents a chromium concentration profile obtained after 10 hours of diffusion time at 800°C.

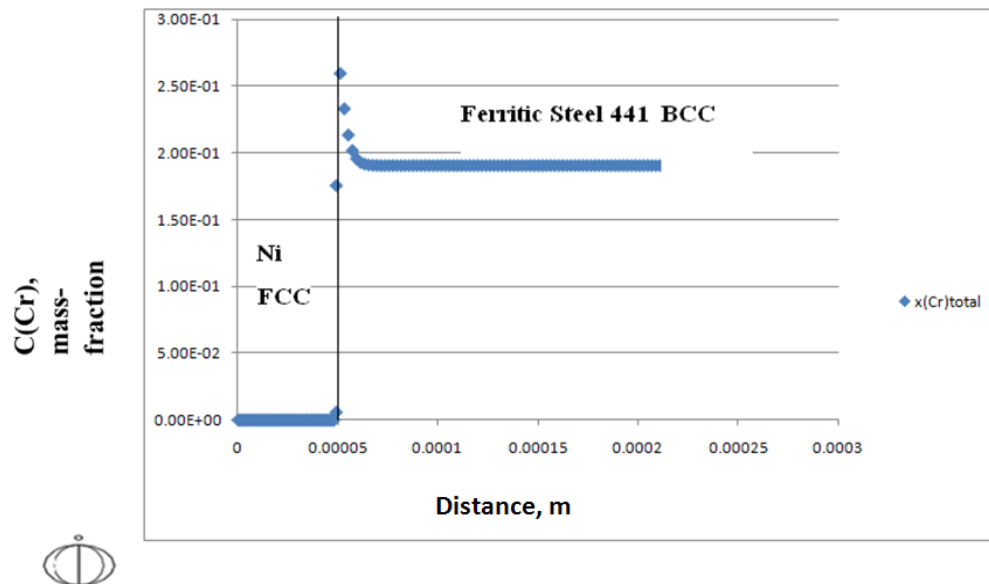


Figure 18. Concentration profile of Cr computed across the 441/Ni interface.

The rise of Cr concentration at the front of the 441/Ni interface is typical for diffusion couples comprised of dissimilar materials with different crystalline lattices. This figure illustrates how a thin layer of Ni may significantly slow down Cr diffusion into the SOEC electrolyte. Future plans are to perform such calculations for longer diffusion times, in order to understand how the Cr concentration profile will evolve after a larger interconnect operation time. Although some amount of Cr is expected to diffuse through the Ni film, there is no doubt that a presence of such a film should significantly diminish the Cr poisoning effects in SOEC devices.

First-principles, density-functional based calculations were also performed for a large periodic supercell that consists of a Ni (fcc) layer on top of an Fe (bcc) layer and with different distribution of Cr impurities within the system. Preliminary results indicate that the most energetically favorable configuration corresponds to the case when a monolayer of Cr is positioned at the interface between the Ni and Fe slabs (Figure 19). The configurations corresponding to the same amount of Cr within the supercell, but homogeneously distributed within the Fe or Ni layers have higher total energies than the segregational configuration shown above. The reason for such a segregational behavior of Cr at the Fe-Ni interface at the electronic structure level still needs to be understood. All of the preliminary first-principle calculations were performed at zero temperature, where the spin variables for all of the included atoms could not be ignored. However, the SOEC operational temperatures ($\sim 800^{\circ}\text{C}$) should properly take into account the entropy terms that may significantly change the results.⁷⁰ Other issues are related to high concentration of interfacial defects (e.g., stacking faults and/or dislocations) at the Ni (fcc)-Fe (bcc) interface because of a significant lattice mismatch between these two phases. These interfacial defects should also cause redistribution of Cr atoms and formation of Cr rich areas at the Fe-Ni boundary layer. Although these problems will be addressed in the future, it is already clear that the unique combination of modeling tools used here is very useful in understanding the qualitative and quantitative behavior of different real materials that could be used in SOEC devices.

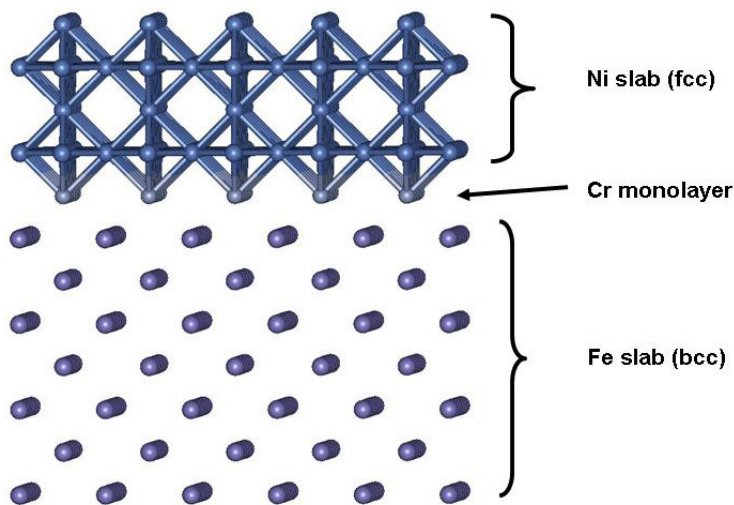


Figure 19. Relaxed structure for a large periodic Ni-Cr-Fe supercell obtained from self-consistent density-functional theory calculations. A Ni (fcc) slab is positioned on top of a Fe (bcc) slab, and a Cr monolayer is located at the Ni-Fe interface.

First-principle calculations were also performed for the so-called Mn-Co spinels, which are also prospective materials for stainless steel interconnects coatings.⁶⁹ In particular, a disordered $(\text{Mn},\text{Co})_3\text{O}_4$ spinel with a nominal composition of $\text{Mn}_{1.5}\text{Co}_{1.5}\text{O}_4$ demonstrates excellent electrical conductivity (3 to 4 orders of magnitude higher than the conductivity of the Cr_2O_3 oxide), satisfactory thermal and structural stability, as well as good thermal expansion that match the Ferritic stainless steel interconnects as shown in Figure 20. Thermally grown layers of this material act as a mass barrier to inhibit the Cr_2O_3 scale growth (by at least 1 to 2 orders of magnitude compared to a free surface) on the stainless steel and to prevent Cr outward migration through the coating as shown in Figure 21. Although Cr oxide scales still grow at the interface between the steel slab and Mn-Co spinel layer (caused by migration of oxygen from spinel into the stainless steel surface layer), Cr becomes sealed by the spinel layer. Atomic-scale modeling shows that the most likely mechanism of Cr migration through the spinel occurs through the exchange between Co atoms in the spinel layer and Cr atoms in the Cr oxide layer (all the other possible mechanisms have a higher migration barrier). However, such an exchange mechanism is endothermic, and a single atom exchange event costs about +1.2 eV of energy. Therefore, Cr migration through the spinel film is thermodynamically unfavorable, which explains the Cr sealing phenomenon.

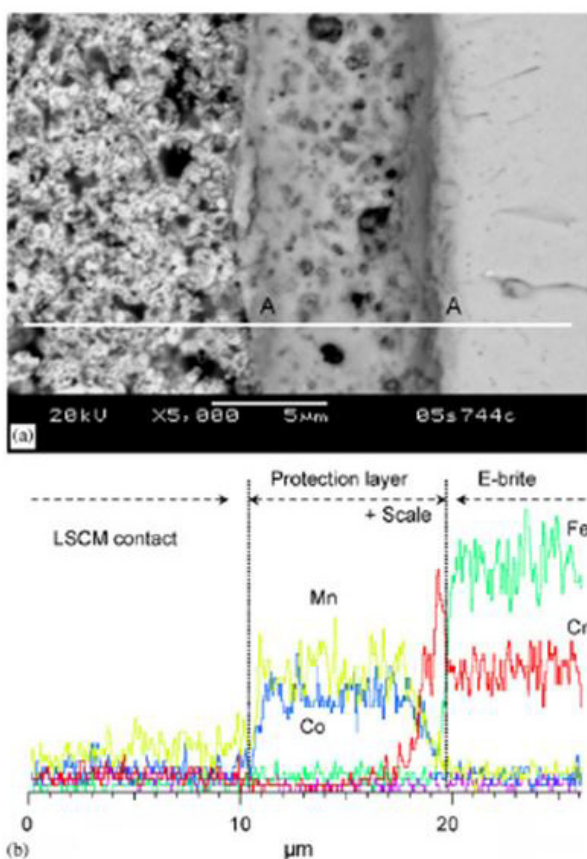


Figure 20. SEM/energy dispersive x-ray spectroscopy (EDS) analysis on E-brite stainless steel (with a relatively high Cr concentration of 27 wt%) with $\text{Mn}_{1.5}\text{Co}_{1.5}\text{O}_4$ protection layer after the contact ASR measurement between the cathode ((La,Sr)CrO₃) and the interconnect at 800°C in air for about 400 h: (a) SEM cross-section and (b) EDS line scan along line A–A in (a). The E-brite coupon spray-coated with spinel precursor was heat-treated in Ar + 2.75% H₂ + 3% H₂O for 4 h prior to the measurement.⁶⁹

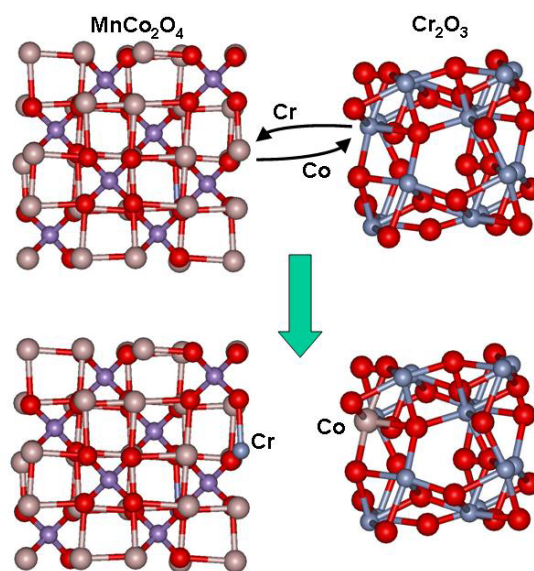


Figure 21. Schematics of the Cr migration mechanism across the interface between MnCo_2O_4 spinel (cubic structure) and Cr_2O_3 oxide (hexagonal structure). Co atoms are shown in brown, O in red, Mn in purple, Cr in blue.

The above examples illustrate how the unique combination of atomic-scale, thermodynamic, and diffusion modeling used in this work allows an understanding of different phenomena for metal and spinel coatings. In perspective, this combined multiscale, interdisciplinary approach will be used to rationally design interconnects for the SOEC devices that will minimize the Cr poisoning effects of electrodes and their interfaces.

4.3.2 Delamination Processes in SOEC

SOECs degradation issues are closely related to diffusion of atoms between the device components. At SOEC operating temperatures ($\sim 800^\circ\text{C}$), all the diffusion processes become very active, and different atoms migrate across interfaces, penetrate into initially clean materials, form new phases, and modify the device functionality. Recent post test examinations of the existing SOEC devices examined at Massachusetts Institute of Technology indicated that transport of Cr containing species from steel interconnects into the oxygen electrode and LSC bond layer and cation segregation and phase separation in the bond layer provide major contributions to the overall SOEC degradation.⁷¹

Our previous experience with first-principle calculations and atomic-scale modeling for different defects in different oxides and ceramics indicates that atomic migration processes can significantly affect the local crystal structure of the material. In particular, migrating hydrogen species in alumina may accumulate in some spatial regions (typically, around aluminum vacancies), break surrounding interatomic bonds, and eventually, create large voids in alumina.⁷² Such a phenomenon will eventually cause mechanical degradation (breakdown) of the alumina film that protects aluminum metal from aggressive chemical environment and initiate pitting corrosion. It was also demonstrated that hydrogen atoms can combine with vacancies in bulk Al and play a crucial role in the embrittlement of this prototypical ductile solid.⁷³

Recent experiments confirm that similar diffusion related phenomena should occur in different components of the SOEC devices (Figure 22). It is apparent that Zr penetrates into the LSM material while La and Mn penetrate into the YSZ electrolyte. A presence of preexisting interfacial defects and granulated structure should even accelerate such a mixing-up process, resulting in appearance of different new phases at the interface including LaZrO_3 , SrZrO_3 , La_2O_3 , Mn_2O_3 , $\text{La}_2\text{Zr}_2\text{O}_7$, etc., which results in the decline of the functionality of both electrode and electrolyte.⁷⁴

In both SOEC and SOFC systems, the LSM electrode is porous while the YSZ electrolyte is dense. Therefore, at their interface, oxygen gases accumulated in porous LSM material should be in dynamic equilibrium with free electrolyte surfaces, which affects the vacancy concentration in YSZ (Figure 23). It is therefore natural to start atomic-scale modeling of the processes at the LSM-YSZ interface considering two models: a free YSZ surface (first consider just a cubic ZrO_2 phase, the role of Y impurities will be discussed later), and a smooth LSM-YSZ interface (Figure 24).

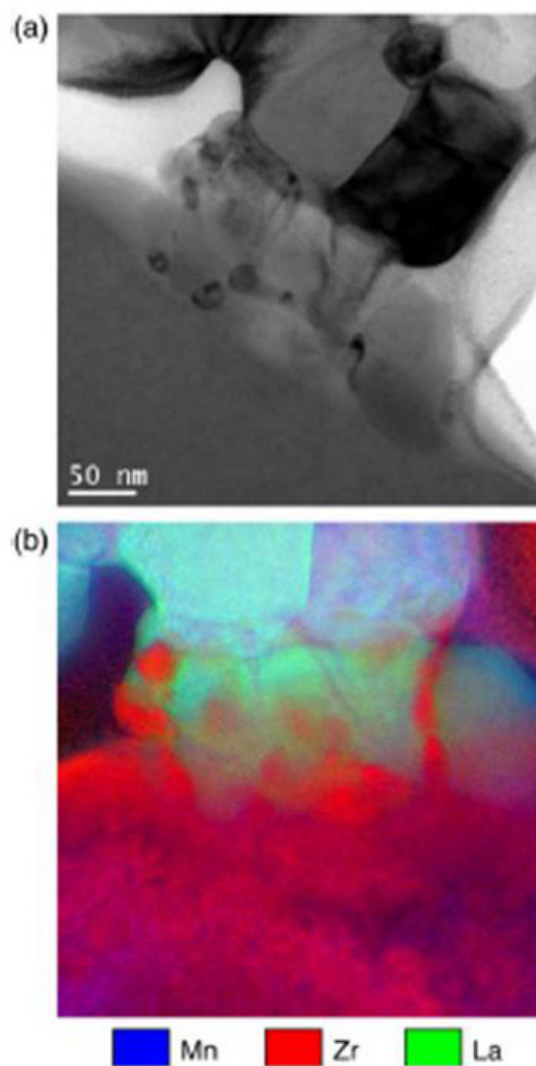


Figure 22. (a) Bright-field temperature electron microscopy image of the SOFC cathode/electrolyte interface, where LSM grains are in contact with the YSZ electrolyte, and (b) EFTEM image combining Zr, Mn, and La map of the same area as in (a).⁷⁴

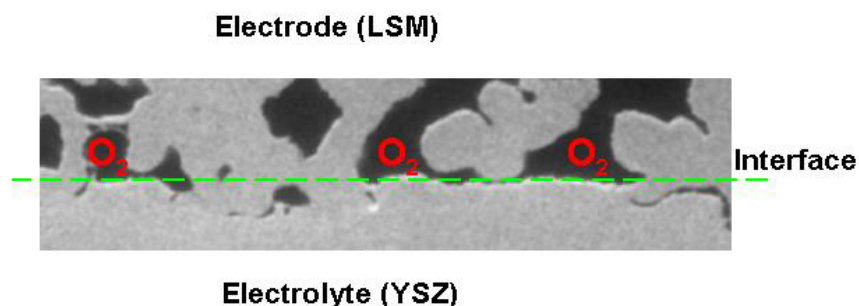


Figure 23. SEM image of the electrode (LSM) and electrolyte (YSZ) interface.⁷⁵

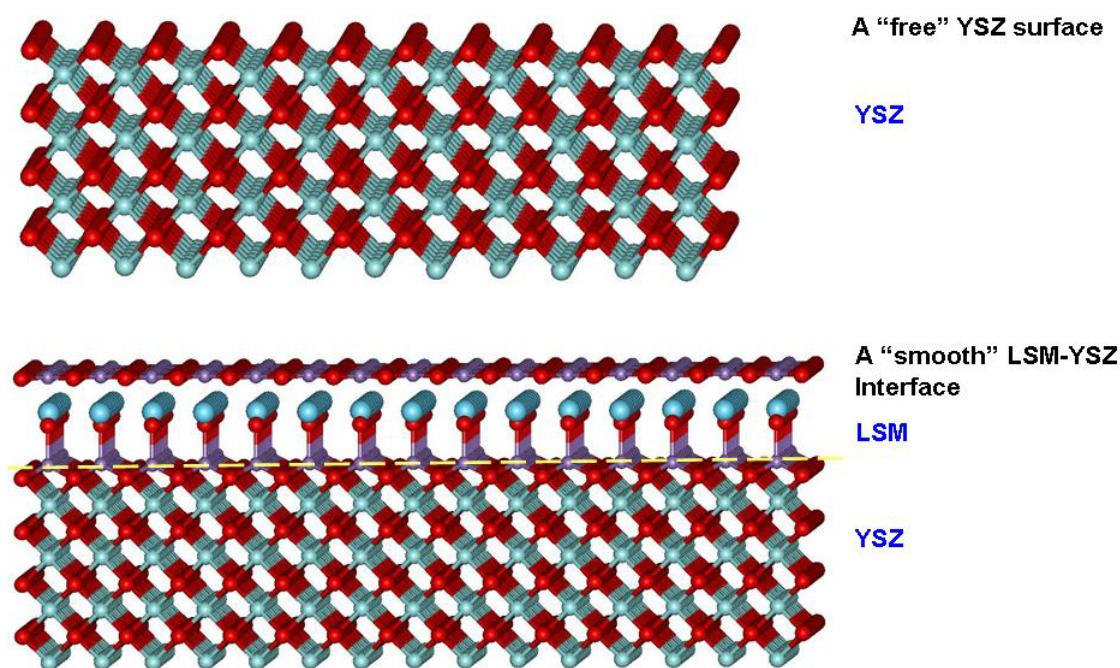


Figure 24. Atomic-scale models for LSM-YSZ interface: a free YSZ surface (top), a smooth LSM-YSZ interface (bottom). Both interfaces have the (001) orientation. Oxygen atoms are shown in red, Zr in small light blue balls, La in big cyan balls, and Mn in purple.

First-principles self-consistent electronic structure calculations show that these two materials may indeed form very high quality interfaces. However, it is possible that different interfacial point and extended defects (stacking faults, steps, dislocations, etc.) could be formed at high temperatures. These defects may accumulate forming oxygen molecules, therefore serving as precipitates for the formation of cracks that will result in the O₂-delamination.

First-principles calculations were performed of the formation energies and migration barriers for different atoms (Sr, La, Mn, Zr, O) migrating across the LSM-YSZ interface. Such a migration at operating temperatures of SOEC and SOFC systems is a well-known fact that has been investigated for SOFCs several times.^{74,76}

Calculations were performed for different possible interstitial and substitutional defects near the LSM-YSZ interface. Typically, substitutional defects for metal impurities have much lower total energies than interstitials. However, at high temperatures, one could expect a significant number of oxygen

vacancies in both LSM and YSZ materials. Therefore, many other low-energy atomic configurations with different local structures are possible. Some metal impurities (e.g., La and Sr) migrating across the interface within the electrolyte may significantly change the YSZ local structure near the interface (subsurface). In particular, La and Sr atoms generate a significantly larger damage in the electrolyte than Mn (Figure 25), simply because the La-O and Sr-O atomic bonds are longer than the Zr-O and Mn-O bonds, causing increased local strain in the electrolyte. In particular, it explains why La penetration into YSZ occurs much slower than Mn migration across the interface.⁷⁶

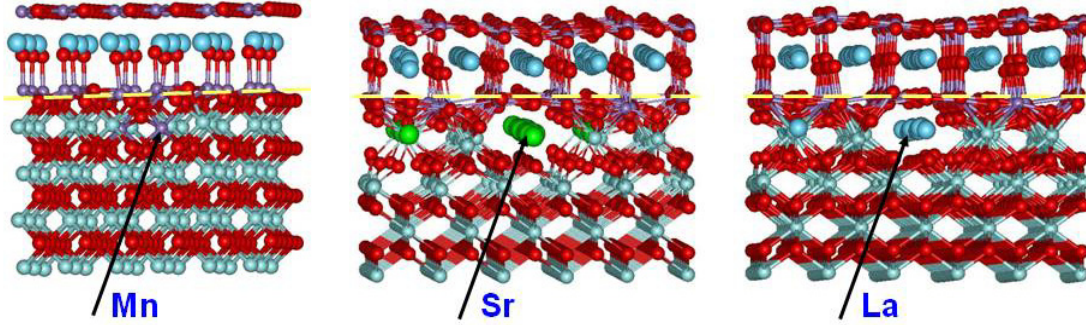


Figure 25. Schematics for substitutional Mn, Sr, and La impurity defects in subsurface area of YSZ near the LSM-YSZ interface. Sr atoms are shown in green.

An accumulation of La and/or Sr in the interfacial region may generate the conditions for the formation of oxygen O-O peroxy bonds, which are precursors of oxygen molecules that will be accumulated within the strained region or void and subsequently initiate the delamination crack formation. Preexisting defects in the bulk of the electrolyte and at the interface between the electrolyte and porous perovskite electrode (oxygen vacancies, voids, grain boundaries, interfacial stacking faults, etc.) may facilitate the La migration and the formation of delamination voids. Estimation of the characteristic time of the migration of different impurities to a certain distance from the interface (within the electrolyte) as well as the characteristic time for the O₂- filled voids growth is under investigation.

Although Mn dopants do not produce any significant damage to the LSM-YSZ interface (like La and Sr dopants), Mn is a mixed valence transition metal and its accumulation within the electrolyte in the vicinity of the interface may significantly increase the electronic conductivity (e.g., through the Mn³⁺ - Mn⁴⁺ transitions). This may also cause a premature conversion of oxygen ions O²⁻ within the electrolyte into neutral oxygen atoms and subsequently, into O₂ molecules that will be accumulated within voids and other defects and accelerate the crack formation.

Therefore, our calculations showed that migration of La, Sr, and Mn atoms from porous LSM anode into YSZ electrolyte may cause a significant damage at the interface between these materials and initiate the O₂ delamination process. Although La, Sr, and Mn atoms behave differently, all of them may participate in degradation mechanisms. Most likely, degradation occurs as a collective effect of all the atoms mixing-up processes at the interface and one should inhibit or mitigate migration of all of these elements across the LSM-YSZ interface.

In order to understand the initiation of cracking at the LSM-YSZ interface, the following simple thermodynamic equation was written for the change of the pressure- and temperature- dependent Gibbs potential at the free YSZ surface (or at the surface within a void in the electrolyte):

$$\Delta G(p, T) = E^{surface-2O^{2-}} - E_{mol}^{O_2} - E^{surface} + \mu_{O_2}^{(0)} + kT \cdot \ln \frac{p_{O_2}}{p_{O_2}^{(0)}}, \quad (4-1)$$

where the first three terms in the right hand side of the Equation 4-1 correspond to the O_2 formation energy at the surface, $\mu_{O_2}^{(0)}$ and $p_{O_2}^{(0)}$ are chemical potential and pressure at normal condition (1 atm), and p_{O_2} is the partial pressure of the O_2 gas, which is in an equilibrium condition with the surface of the electrolyte.

First-principle calculations indicate that the surface of the electrolyte is intrinsically unstable, the O_2 formation energy is negative as shown in Figure 26, and low-valence impurities positioned into subsurface region increase the surface instability even further. It means that the YSZ surface always has a tendency to evaporate oxygen gas and form oxygen vacancies at the surface which later may drift into the bulk. Such evaporation will stop only when the pressure term will make ΔG positive. This phenomenon is not surprising, otherwise, this material could not be a good oxygen ion conductor.

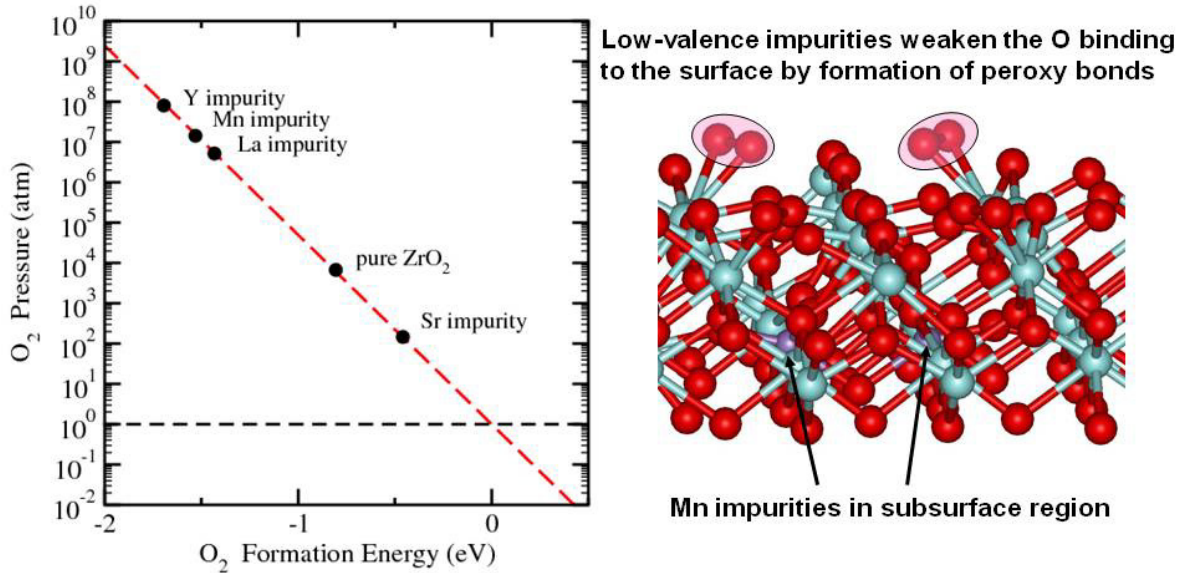


Figure 26. Equilibrium pressure of O_2 gas on top of the YSZ electrolyte at $T = 800^\circ C$ as a function of O_2 formation energy; black points correspond to different impurities positioned in the YSZ subsurface region below the surface (left). Schematics of the formation of peroxy O-O bonds at the surface (precursors of O_2 molecules) caused by substitutional Mn impurities in the subsurface region (right).

However, the formation of neutral oxygen gas molecules is possible only if the O^{2-} ion loses its two electrons and becomes neutral, i.e., the regions where O_2 molecules are created should exhibit electronic conductivity in order to take these electrons away from oxygen ions. Neutral oxygen gas is therefore not expected to accumulate in a closed void inside the electrolyte because there is no place for oxygen ions to drop their electrons without accumulating electric charge. However, the formation of oxygen gas is possible in subsurface voids below a free electrolyte surface doped with Mn, which increases the electronic conductivity, and/or at the LSM-YSZ interface, which contains a lot of different structural defects and grain boundaries that exhibit electron conductivity. In these conditions, a very high pressure of O_2 in such a void may be reached and a preexisting void with radius above some critical value will tend to grow spontaneously, i.e., the O_2 -electrode delamination process will be initiated. A simple estimate that used parameters obtained from first-principles calculations shows that for Mn-doped YSZ surface, the critical radius for such an unstable void should be of the order of 10 Å, which corresponds to several Zr-O bond lengths in YSZ.

The qualitative arguments considered above provided us an opportunity to make some comparison between the SOEC and SOFC devices. In the SOFC devices, the porous LSM electrode plays the role of

cathode and the O_2 gas is coming into this electrode. In the SOEC devices, the LSM electrode is an anode that collects only those oxygen species that came through the YSZ electrolyte. A higher partial O_2 pressure can thus be expected in the LSM pores near the LSM-YSZ interface in SOFC, but not in the SOEC. According to Equation 4-1, the higher oxygen gas pressure will inhibit the oxygen vacancy formation process in the electrolyte, and the lower concentration of O vacancies in YSZ will slow down the diffusion of Mn, La, and Sr into the electrolyte from the LSM electrode. Such a qualitative argument may explain why the O_2 delamination processes in the SOFC devices are developing slower than in the SOEC devices, i.e., why the SOFC devices have a longer lifetime.

5. MODELING BASED ENGINEERING SOLUTIONS THAT HELP IMPROVE OPERATION OF THE SOECS

A natural way of mitigating and/or slowing down the degradation mechanisms described above is to stop the undesirable migration of atoms between different SOEC components. In particular, the goal was to add an additional thin layer between the YSZ electrolyte and LSM anode that would slow down the migration of La, Mn, Sr, and Zr across the interface without reducing the oxygen transport. Several complex oxides may be considered as candidates for such a thin film. The characteristics that may be crucial in choosing this material are: (a) the lattice constants should match to both YSZ and LSM crystal structure; (b) the thermal expansion coefficients should be compatible; (c) the tendency to form interfacial defects should be minimal; (d) the diffusivity of La, Mn, Sr, and Zr atoms through this material should be low. Before reaching any practical recommendations, atomic-scale modeling will be used to estimate the change in diffusivity matrix across the interface because of the presence of this additional layer. This will give a set of important parameters that will be used in the DICTRA codes to model the time evolution of the concentration of different elements in the interfacial region. At the same time, the Thermo-Calc equilibrium thermodynamics calculations will provide the picture of the phase formation in the same region. The complementary atomic-scale, thermodynamics, and kinetics modeling will provide a detailed analysis of the degradation mechanisms in the electrode-electrolyte interfacial region. A similar analysis will be performed for other interfaces in the SOEC devices that may exhibit degradation because of the migration of atoms between different components of the system. The ultimate goal of this simulation work is to provide considerations for rational design of coating for the interconnect electrode.

As mentioned above, one of the main mechanisms of the electrolyte degradation is related to the diffusion of relatively large La and Sr cations into the electrolyte. This may create structural discontinuities at the electrolyte/electrode interfaces resulting in deterioration of the SOEC properties. While continuous search for new and improved materials in this field continues, our preliminary calculations indicate that the degradation resistance of existing materials could be improved substantially using such techniques as coating and diffusion barriers. In the case of the LSM-YSZ interface, a simple additional layer of 0.1 to 1.0 μm of CeO_{2-x} oxide positioned between the LSM and YSZ layers could work efficiently, preventing diffusion of large La and Sr cations.

Ceria is a well-known O^{2-} ion conductor and may be used as an electrolyte for SOFC devices itself. The Ce-O phase diagram is presented in Figure 27. When the oxygen content x of CeO_{2-x} varies between 0 and 0.5, ceria may exhibit different unstable and metastable phases, and its ability to change the structure with variations of oxygen concentration is the key to understanding the ion conductivity mechanism in this material. In particular, ceria may be doped with some three-valent element (e.g., gadolinium), which increases its conductivity because of the formation of larger numbers of oxygen vacancies. The cerium-gadolinium oxide (CGO) with chemical formula $\text{Ce}_{0.8}\text{Gd}_{0.2}\text{O}_{1.9}$, was shown to be a good barrier to stop the diffusion of Y and Zr from the YSZ electrolyte (Figure 28) and improve the SOFC performance.⁷⁷ Actually, a 1.4 μm layer of CGO is sufficient to stop the diffusion, but the CGO film used in these experiments was porous, and it may happen that a better quality film may be even be thinner. Other experiments on samaria doped ceria indicate that this film may stop the diffusion of Mo, Mn, and Sr.⁷⁸

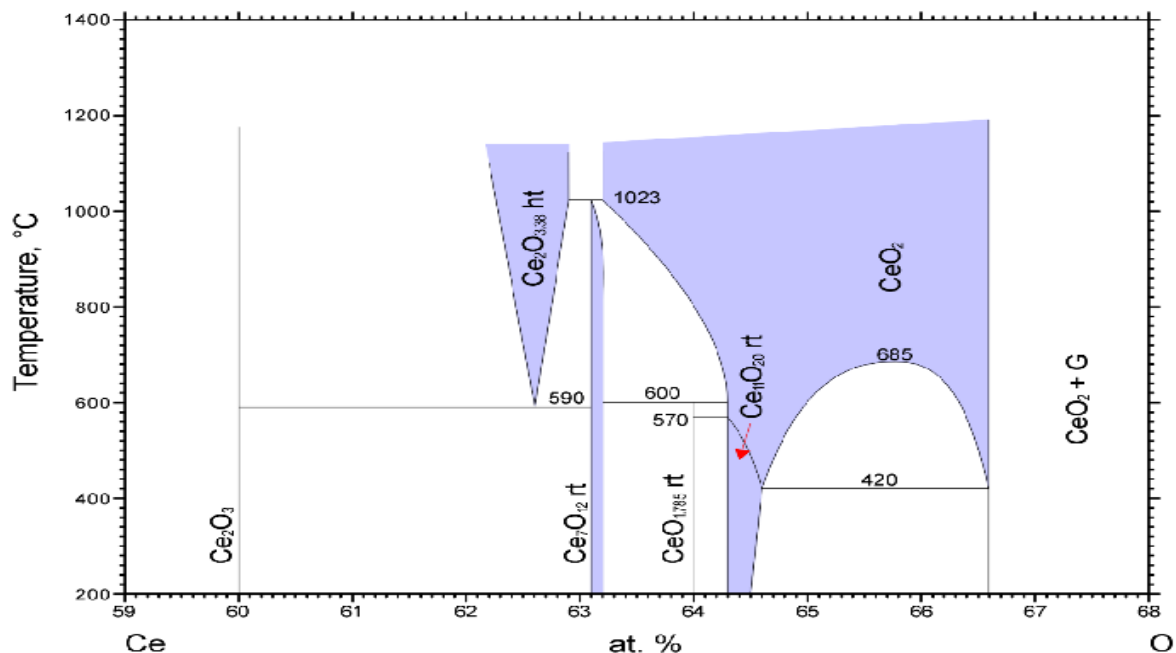


Figure 27. The cerium-oxygen phase diagram.⁷⁹

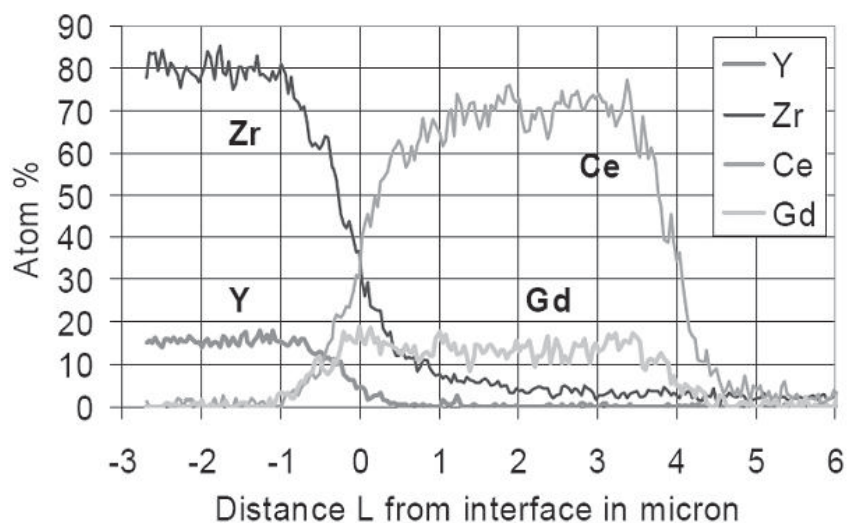


Figure 28. EDX-line scans of zirconia-ceria-fracture interface of 4-micron-thick CGO barrier layer sample. The origin of the x-axis is located at the zirconia-ceria interface, which is defined as the location where the amount of Zr equals Ce.⁷⁷

In order to better understand the diffusion of La and Sr cations across a ceria film, a first-principles calculations and the nudge elastic band method⁸⁰ was used to calculate migration barriers of La impurity across the ceria film. The self-diffusion migration barrier for Ce atom in pure ceria was found to be about 4.5 eV (the diffusion occurs through the vacancy mechanism). Such a high diffusion barrier explains why no self-diffusion of Ce was experimentally observed at temperatures below 900°C.⁷⁸ The migration of oxygen, however, starts at much lower temperatures (~5000°C) which means that new mechanisms for Ce self-diffusion through ceria may open as well. At any rate, migration of Ce in ceria at the SOEC working temperatures (~800°C) are not expected.

For a substitutional La impurity defect, the migration barrier through ceria is even higher (~ 6.5 eV). Therefore, one cannot expect any significant migration of La across the ceria barrier layer, even at 800°C . Indeed, a substitutional La defect produces a significant distortion of the local crystal structure in ceria by pushing surrounding oxygen atoms away as shown in Figure 29, and it may be expected that migration of such a big cation will be suppressed. Such a behavior of La cation in ceria is very similar to the lanthanum behavior in γ -alumina described in our previous publication.⁸¹ La never goes into the bulk of the aluminum oxide and stabilizes its surface by attaching to it with a very high binding energy, which prevents any surface reconstructions and improves the catalytic behavior of γ -alumina often used as a support for catalytic nanoparticles. The ceria barrier between the YSZ electrolyte and LSM anode may thus be a good option to reduce the formation of oxide phases with high resistivity and to avoid oxygen delamination.

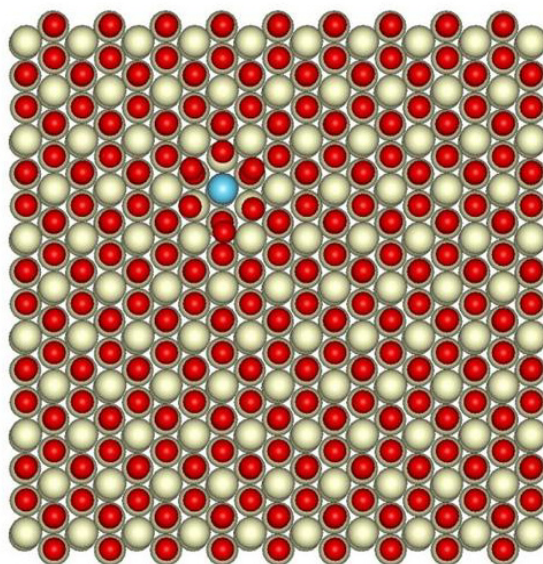


Figure 29. Schematics of substitutional La defect on top of CeO_2 surface. Ce atoms are shown in gray, O in red, and La in blue.

Another idea that naturally comes from the discussion of the previous section is to reduce the degradation processes at the LSM-YSZ interface leading to oxygen delamination by controlling the gas pressure in the porous SOEC anode. From Equation 4-1 it follows that increasing the oxygen pressure one could decrease the vacancy concentration in the regions of the electrolyte adjacent to the LSM-YSZ interface. This should slow down the migration of large cations (especially, La and Sr) into the electrolyte, thereby increasing the lifetime of the SOEC device. The complete understanding of this phenomenon needs more modeling efforts completed in a close collaboration with experimental activities.

6. SUMMARY AND CONCLUSIONS OF ATOMISTIC MODELING

An effort was made to identify, understand, and consequently propose different ways to mitigate a number of problems that reduce the lifetime of existing SOEC devices developed and tested at INL. A uniqueness of this approach was using a powerful combination of equilibrium thermodynamics, non-equilibrium (diffusion) modeling, and first principles atomic-scale calculations to understand the degradation mechanisms and provide practical recommendations on how to inhibit and/or completely mitigate them.

To continue this multiscale, interdisciplinary modeling of the SOEC system, thermodynamics and kinetic modeling databases are needed for each of the oxides. As mentioned above, both thermodynamic and diffusion databases are readily available for steels, while mobility databases are absent and need to be developed for oxides and perovskites used in the SOEC devices. Because of insufficient experimental data for these materials, the only way to develop such databases is to use first-principles density functional calculations and atomic-scale modeling. The diffusivity matrices should be constructed through combined efforts of searching existing literature on oxides and perovskites and by performing atomic-scale modeling (MD and KMC) of these ceramics. Based on these databases, extended kinetic modeling will also help to optimize the real life materials and coatings by minimizing all the undesirable transport processes (including Cr transport from steel interconnects, La and Sr across the electrode-electrolyte interface, etc.) in the SOEC systems. This goal bridges both problems of SOEC development and diffusion bonding of superalloys in primary and secondary circuits of nuclear reactors. Databases for complex oxide structures will be developed using an ab initio physical approach through a collaboration with Prof. Zi-Kui Liu of Pennsylvania State University. His group has extensive experience in developing such databases for different materials (including perovskites).

6.1 Future Work

The multiscale, interdisciplinary approach and preliminary results described in this report are just the first step in the planned future modeling/simulation efforts. This approach is a proven tool in developing real life materials and coatings for the SOEC devices. In a long run, this approach will be used for rational design of the materials and systems that exhibit the best functionality for the SOECs. In particular, work on the following topics is planned:

1. Thermodynamic and diffusion modeling for steel SOEC interconnects and their coatings. The target of this thrust is to significantly inhibit and/or mitigate the Cr poisoning in the SOEC devices. Consideration of other alloys for these purposes is also possible.
2. Understanding of atomic mechanisms of oxygen delamination and studying different ways for its mitigation (coatings, increasing pressure in the devices, etc.).
3. Investigating (by modeling/simulation) the catalytic activity of the nickel-zirconia cermet cathodes. The target is to increase the efficiency of the cathode in producing hydrogen and to avoid the degradation (by different mechanisms) of catalyst working under extreme conditions (temperature, water vapor, etc.).
4. Considering possibilities of using other materials for electrodes, electrolyte, and interconnects.
5. Identifying modeling based engineering solutions that will help improve operation of the SOEC devices up to the point when they will become economically feasible.

The experimental work on improving the SOEC devices will be accompanied by the post-mortem morphological analysis of features existing on the surfaces of different device components in order to quantify optimal conditions for their functioning inside the cell and their minimal structural degradation. A powerful code is available for performing such a morphological study. An example of such analytical work is presented in a recent paper.⁸²

7. SUMMARY OF DEGRADATION MODELING IN SOEC

The non-equilibrium model shows that the degradation/failure of SOEC is primarily the result of delamination along the oxygen electrode/electrolyte interface. Oxygen electrode delamination occurs as a result of the formation of high internal oxygen pressure within the electrolyte, just near the oxygen electrode/electrolyte interface.

Preliminary calculations show that modest changes in electronic conduction can cause orders of magnitude changes in oxygen pressure. Thus, the present analysis shows that a small amount of electronic conduction through the electrolyte is actually preferred for its stability. This is a significant result as it suggests that an oxygen ion conductor of the highest possible ionic transport number (negligible electronic transport number) may be more prone to oxygen electrode delamination and is thus not as desirable a material as an electrolyte. In this context, YSZ may not be the ideal material as electrolyte for SOEC, especially at temperature of 800°C and lower.

The addition of a small amount of a transition metal oxide or other oxides with cations exhibiting multiple valence states, such as ceria, to the electrolyte should increase its electronic conductivity and decrease the tendency for delamination of the oxygen electrode. It should be possible to suitably tailor electronic transport through the cell to minimize the tendency for high pressure buildup and simultaneously ensure a relatively high ionic transport number for the cell and thus a high electrolyzer efficiency. This can be achieved by depositing a very thin layer of a purely oxygen ion conductor with a high electronic resistance on the base electrolyte on the oxygen electrode side.

The overall propensity for oxygen electrode delamination can be described by a parameter given in terms of the various transport parameters, namely, $\frac{r_e^a R_i}{r_i^a R_e}$. The higher the $\frac{r_e^a R_i}{r_i^a R_e}$, the smaller is the propensity for oxygen electrode delamination. In terms of the operating parameters, delamination should not occur as long as $\frac{E_A - E_N}{E_A} < \frac{r_e^a R_i}{r_i^a R_e}$ or $E_A < \frac{E_N}{\left(1 - \frac{r_e^a R_i}{r_i^a R_e}\right)}$.

A unique combination of equilibrium thermodynamics, non-equilibrium (diffusion) modeling, and first-principles, atomic-scale calculations was used to understand the degradation mechanisms in the SOEC devices and provide recommendations on how to inhibit and/or completely mitigate them. In particular, some practical recommendations were provided on how to modify the SOEC multicomponent systems to minimize Cr transport and to inhibit oxygen delamination processes. These conclusions will help to increase the lifetime of SOEC devices and make it possible to use them in industrial and/or commercial applications.

Understanding electrochemical phenomena is essential for developing a model of a SOEC stack. With a suitable model, various stack characteristics and operating parameters such as materials of composition and operational transients can be modeled to understand the impact of a single or several parameters on stack degradation. It can also help to understand the relative importance of various cell/stack parameters. A functioning model could thus be used to improve the material composition of cell components. As a general rule, any process model is used to plan for experimental testing and improve operation. If the coupling of various electrochemical phenomena are too complex, as a minimum, single phenomenon models should be developed that can also be verified by experimentation.

8. REFERENCES

1. Guan J., et al., "High performance flexible reversible solid oxide fuel cell," GE Global Research Center Report DE-FC36-04GO14351, May 15, 2007.
2. Carter, D. et al., "Determining Causes of Degradation in High Temperature Electrolysis Stacks," Presented at the Workshop on Degradation in Solid Oxide Electrolysis Cells and Strategies for its Mitigation, October 27, 2008, *Fuel Cell Seminar & Exposition, Phoenix, AZ*.
3. Gazzarri, J. I., "Impedance Model of a Solid Oxide Fuel Cell for Degradation Diagnosis," Ph. D. Thesis, University of British Columbia, Vancouver, Canada, 2007.
4. Ivers-Tiffée, E., and A. V. Virkar, "Electrode Polarisation," Chapter 9 in *High Temperature Solid Oxide Fuel Cells: Fundamentals, Design and Applications*, (Edited by) S. C. Singhal and K. Kendall Elsevier, Oxford, U.K., 2003.
5. Akkaya, A. V., "Electrochemical Model for Performance Analysis of a Tubular SOFC," *Int. J. Energy Research*, Vol. 31, 2007, pp. 79–98.
6. Windisch, C. F., J. W. Stevenson, S. P. Simner, R. E. Williford, and L. A. Chick, "Experimentally-Calibrated Spreadsheet-based SOFC Unit-Cell Performance Model," Pacific Northwest National Laboratory, PNNL-SA-37014, presented at *2002 Fuel Cell Seminar: Fuel Cells-Reliable, Clean Energy for the World, Palm Springs, CA*, 21 November 2002
7. Virkar, A. V., "A Model for Solid Oxide Fuel Cell (SOFC) Stack Degradation," *J. Power Sources*, Vol. 172, 2007, pp. 713–724.
8. Ni, M., M. K. H. Leung, and D. Y. C. Leung, "A Modeling Study on Concentration Overpotentials of a Reversible Solid Oxide Fuel Cell," *J. Power Sources*, Vol. 163, 2006, pp. 460–466.
9. Noren, D. A. and M. A. Hoffman, "Clarifying the Butler-Volmer Equation and Related Approximations for Calculating Activation Losses in Solid Oxide Fuel Cell Models," *J. Power Sources*, Vol. 152, 2005, pp. 175–181.
10. Gemmen, R. S., M. C. Williams, and K. Gerdes, "Degradation Measurement and Analysis for Cells and Stacks," *J. Power Sources*, Vol. 184, 2008, pp. 251–259.
11. Doenitz W., R. Schmidberger, E. Steinheil, and R. Streicher, "Hydrogen production by high temperature electrolysis of water vapour," *Int. J. Hydrogen Energy*, Vol. 5, 1980, pp. 55–63.
12. Doenitz W., G. Dietrich, and R. Streicher, "Electrochemical high temperature technology for hydrogen production or direct electricity generation," *Int. J. Hydrogen Energy*, Vol. 13, Issue 5, 1988, pp. 283–287.
13. Doenitz and E. Erdle, "High-temperature electrolysis of water-vapour – status of development and perspectives for application," *Int. J. Hydrogen Energy*, Vol. 10, 1985, pp. 291–295.
14. Isenberg, A. O., "Energy conversion via solid oxide electrolyte electrochemical cells at high temperatures," *Solid State Ionics*, Vol. 3, Issue 4, pp. 431–437.
15. Jensen, S. H., P. H. Larsen, and M. Mogensen, "Hydrogen and synthetic fuel production from renewable energy sources," *Int. J. Hydrogen Energy*, Vol. 32, 2007, pp. 3253–3257.
16. Herring, J. S., et al., "Progress in high-temperature electrolysis for hydrogen production using planar SOFC technology," *Int. J. Hydrogen Energy*, Vol. 32, 2007, pp. 440–450.
17. Momma A, T. Kato, Kaga, Y. S. Nagata, "Polarization behavior of high temperature solid oxide electrolysis cells (SOEC)," *J. Ceram. Soc. Japan.*, Vol. 105, 1997, pp. 369–373.

18. O'Brien, J. E., C. M. Stoots, J.S. Herring, K. G. Condie, and G. K. Housley, "The high-temperature electrolysis program at the Idaho National Laboratory: observations on performance degradation," OSTI ID: 961915, DE-AC07-99ID-13727, Report No. INL/CON-09-15564.
19. Mawdsley, J. R., J. D. Carter, A. J. Kropf, B. Yildiz, and V. A. Maroni, "Post-test evaluation of oxygen electrodes from solid oxide electrolysis stacks," *Int. J. of Hydrogen Energy*, Vol. 34, 2009, pp. 4198–4207.
20. Doenitz, W., and Schmidberger, "Concepts and design for scaling up high temperature water vapour electrolysis," *Int. J. Hydrogen Energy*, Vol. 7, 1982, pp. 321–330.
21. Quandt, K. H. and R. Streicher, "Concept and design of a 3.5 MW pilot plant for high temperature electrolysis of water vapor," *Int. J. Hydrogen Energy*, Vol. 11, 1986, pp. 309–315.
22. Maskalick, N. J., "High temperature electrolysis cell performance characterization," *Int. J. Hydrogen Energy*, Vol. 11, 1986, pp. 563–570.
23. Iwahara, H., H. Uchida, and I. Yamasaki, "High-temperature steam electrolysis using SrCeO₃-based proton conductive solid electrolyte," *Int. J. Hydrogen Energy*, Vol. 12, 1987, pp. 73–77.
24. Kreuter, W., and H. Hofmann, "Electrolysis: The important energy transformer in a world of sustainable energy," *Int. J. Hydrogen Energy*, Vol. 23, 1998, pp. 661–666.
25. Shin, Y., W. Park, J. Chang, and J. Park, "Evaluation of the high temperature electrolysis of steam to produce hydrogen," *Int. J. of Hydrogen Energy*, Vol. 32, 2007, pp. 1486–1491.
26. Erdle, E., W. Doenitz, R. Schamm, and A. Koch, "Reversibility and polarization behavior of high temperature solid oxide electrochemical cells," *Int. J. Hydrogen Energy*, Vol. 17, 1992, pp. 817–819.
27. Virkar, A. V., "Theoretical analysis of the role of interfaces in transport through oxygen ion and electron conducting membranes," *J. Power Sources*, Vol. 147, 2005, pp. 8–31.
28. Kondepudi, D., and I. Prigogine, *Modern Thermodynamics: From Heat Engines to Dissipative Structures*, John Wiley & Sons, New York, 1998.
29. Tennebaum, A., G. Ciccotti, and R. Gallico, "Stationary non-equilibrium states by molecular dynamics: Fourier's law," *Phys. Rev. A*, Vol. 25, No. 5, 1982, pp. 2778–2787.
30. Rosjorde, A., D. W. Fossmo, D. Bedeaux, S. Kjelstrup, and B. Hafskjold, "Nonequilibrium molecular dynamic simulations of steady-state heat and mass transport in condensation," *J. Colloid and Interface Science*, Vol. 232, 2000, pp. 178–185.
31. Bedeaux, D., S. Kjelstrup, and J. M. Rubi, "Nonequilibrium translational effects in evaporation and condensation," *J. Chem. Phys.*, Vol. 119, No. 17, 2003, pp. 9163–9170.
32. Armstrong, R. D., M. Todd, p. 264, in Bruce PG (Ed.), *Solid State Chemistry*, Cambridge University Press, Cambridge, UK, 1995.
33. Wagner, C., "Equations of transport in solid oxides and sulfides of transition metals," *Prog. Solid-State Chem.*, Vol. 10, No. 1, 1975, pp. 3–16.
34. Heyne, L., Mass Transport in Oxides, *NBS Special Publication 296*, 1968, pp. 149–164.
35. Hebb, M. H., "Electrical conductivity of silver sulfide," *J. Chem. Phys.*, Vol. 20, 1952, pp. 185–190.
36. Kofstad, P., *Nonstoichiometry, Diffusion, and Electrical Conductivity in Binary Metal Oxides*, John Wiley & Sons, New York, 1972.
37. Virkar, A. V., "Theoretical analysis of solid oxide fuel cells with two-layer, composite electrolytes: electrolyte stability," *J. Electrochem. Soc.*, Vol. 138, No. [5] 1481–1487 (1991).

38. Virkar, A. V., J. Nachlas, A. V. Joshi, and J. Diamond, "Internal precipitation of molecular oxygen and electromechanical failure of zirconia solid electrolytes," *J. Am. Ceram. Soc.*, Vol. 73, No. 11, 1990, pp. 3382–90.
39. Lim, H-T., and A. V. Virkar, "Measurement of oxygen chemical potential in thin electrolyte film, anode-supported solid oxide fuel cells," *J. Power Sources*, Vol. 180, 2008, pp. 92–102.
40. Kjelstrup, S., and D. Bedeaux, "Non-Equilibrium Thermodynamics of Heterogeneous Systems," Series on Advances in Statistical Mechanics, Volume 16, *World Scientific*, New Jersey, 2008.
41. Virkar AV, "A model for internal pressurization in cationic solid electrolytes," *J. Mater. Sci.*, Vol. 20, 1985, pp. 552–562.
42. Barin, I., *Thermochemical Data on Pure Substances: Parts I and II*, VCH Publication, Weiheim, Germany, 1993.
43. Lim, H-T., and A. V. Virkar, "A study of solid oxide fuel cell stack degradation by inducing abnormal behavior in a single cell test," *J. Power Sources*, Vol. 185, 2008, pp. 790–800.
44. Hauch, A., S. D. Ebbesen, S. H. Jensen, and M. Mogensen, "Solid oxide electrolysis cells: Microstructure and degradation of the Ni/yttria-stabilized zirconia electrode," *J. Electrochem. Soc.*, Vol. 155, No. 1, 2008, pp. B1184–B1193.
45. Brisse, A., J. Schefold, and M. Zahid, "High temperature water electrolysis in solid oxide fuel cells," *Int. J. Hydrogen Energy*, Vol. 33, 2008, pp. 5375–5382.
46. Doenitz, W., E. Erdle, R. Streicher, "Electrochemical Hydrogen Technologies. Electrochemical Production and Combustion of Hydrogen," edited by H. Wendt, Elsevier, Amsterdam, 1990. Chapter 3, pp. 213–259.
47. Lim, H-T., "Ionic and electronic transport across interfaces in thin electrolyte film, anode-supported solid oxide fuel cells," PhD dissertation, University of Utah, 2009.
48. Sohal, M. S., et al., "Critical Causes of Degradation in Integrated Laboratory Scale Cells during High-Temperature Electrolysis." INL/EXT-09-16004 Report, May 2009.
49. Stoots, C. M., et al., "Integrated Laboratory Scale Test Report." INL/EXT-09-15283 Report, February 2009.
50. Sushko, P. V., A. L. Shluger, and C. R. A. Catlow. "Relative energies of surface and defect states: *Ab initio* calculations of the MgO (001) surface," *Surf. Sci.* Vol. 450, p. 153, 2000.
51. Frisch, M. J., et al., Gaussian 09 Reference Manual, Revision A-1, Gaussian, Inc., Wallingford CT, 2009.
52. Kresse, G., and J. Hafner, "*Ab initio* molecular dynamics for liquid metals," *Phys. Rev. B*, Vol. 48, p. 13115, 1993.
53. Kresse, G., and J. Furthmüller, "Efficient iterative schemes for *ab initio* total-energy calculations using a plane-wave basis set," *Phys. Rev. B*, Vol. 54, p. 11169, 1996.
54. Kresse, G., and J. Hafner, "*Ab initio* simulation of the metal/nonmetal transition in expanded fluid mercury," *Phys. Rev. B*, Vol. 55, p. 7539, 1997.
55. Gibbs, J. W., "The Collected Works," Vol.1, New Haven, Yale University Press, 1948.
56. Hillert, M., "Phase Equilibria, Phase Diagrams, and Phase Transformations: Their Thermodynamic Basis," 2nd edition, Cambridge University Press, Cambridge, 2008.
57. Saunders, N., and A. P. Miodownik, "CALPHAD: Calculation of Phase Diagrams," Pergamon Press, New York, 1998.

58. Andersson, J. O., et al., "A New Method of Describing Lattice Stabilities," CALPHAD 11, 93-98, 1987.
59. Liu, Z.-K., "First-Principles Calculations and CALPHAD Modeling of Thermodynamics," *Journal of Phase Equilibria and Diffusion*, Vol. 30, No. 5, p. 517, 2009.
60. Glazoff, M. V., F. Barlat, and H. Weiland, "Continuum physics of phase and defect microstructures: Bridging the gap between physical metallurgy and plasticity of aluminum alloys," *International Journal of Plasticity*, Vol. 20, No. 3, pp. 363-402, 2004.
61. Engstrom, A., J. E. Morral, and J. Agren, "Computer simulations of Ni-Cr-Al diffusion couples," *Acta Materialia*, Vol. 45, pp. 1189-1199, 1997.
62. Sundman, B., B. Jansson, and J.-O. Andersson, CALPHAD, Vol. 9, p. 153, 1985.
63. Borgenstam, A., A. Engstrom, L. Hoglund, and J. Agren, "DICTRA: A tool for simulation of diffusional transformations in alloys," *Journal of Phase Equilibria*, Vol. 21, No. 3, pp. 269-280, 2000.
64. Association of Iron and Steel Engineers (AISE), "The Making, Shaping, and Treating of Steel," AISE, Pittsburgh, PA, 1985.
65. Williams, D. N., R. H. Ernst, J. J. English, and E. S. Bartlett, "Oxidation protection of a chromium alloy by nickel-alloy claddings," *Journal of the Less-Common Metals*, Vol. 24, p. 41, 1971.
66. Ogasawara, K., et al., "Chemical stability of ferritic alloy interconnect for SOFCs," *Journal of the Electrochemical Society*, Vol. 154, No. 7, B657-B663, 2007.
67. Ebrahimifar, H., M. Zandrahimi, and H. Habibifar, "Improved electrical conductivity of coated ferritic stainless steel used in SOFC as interconnect at 700°C," *International Journal of Electronic Engineering Research*, Vol. 2, No. 4, p. 519, 2010.
68. Chen, X., P. Y. Hou, C. P. Jacobson, S. J. Visco, and L. C. De Jonghe, "Protective coating on stainless steel interconnect for SOFCs: Oxidation kinetics and electrical properties," Lawrence Berkeley National Laboratory Preprint, Publication date: April 1, 2004.
69. Yang, Z., G.-G. Xia, X.-H. Li, and J. W. Stevenson, "(Mn,Co)3O4 spinel coatings on ferritic stainless steels for SOFC interconnect applications," *International Journal of Hydrogen Energy*, Vol. 32, pp. 3648-3654, 2007.
70. Geng, W. T., "Cr segregation at the Fe-Cr surface: A first-principles GGA investigation," *Phys. Rev. B*, Vol. 68, p. 233402, 2003.
71. Sharma, V. I., and B. Yildiz, "Degradation mechanism in La_{0.8}Sr_{0.2}CoO₃ as contact layer on the solid oxide electrolysis cell anode," *J. Electrochem. Soc.*, Vol. 157, B441-B448, 2010.
72. Rashkeev, S. N., K. W. Sohlberg, S. Zhuo, and S. T. Pantelides, "Hydrogen-induced initiation of corrosion in aluminum," *J. Phys. Chem.*, Vol. C 111, p. 7175, 2007.
73. Lu, G., and E. Kaxiras, "Hydrogen embrittlement of aluminum: The crucial role of vacancies," *Phys. Rev. Lett.*, Vol. 94, p. 155501, 2005.
74. Liu, Y. L., et al., "Microstructural studies on degradation of interface between LSM-YSZ cathode and YSZ electrolyte in SOFCs," *Solid State Ionics*, Vol. 180, pp. 1298-1304, 2009.
75. Singhal, S. C., "Advances in solid oxide fuel cell technology," *Solid State Ionics*, Vol. 135, pp. 305-313, 2000.
76. Mori, M., et al., "Reaction mechanism between lanthanum manganite and yttria doped cubic zirconia," *Solid State Ionics*, Vol. 123, pp. 113-119, 1999.

77. van Berkel, F. P. F., Y. Zhang-Steenwinkel, G. P. J. Schoemakers, M. M. A. van Tuel, and G. Rietveld, "Enhanced ASC performance at 600°C by ceria barrier layer optimization," *ECS Transactions*, Vol. 25, No. 2, pp. 2717-2726, 2009.
78. Chang, H.-C., D.-S. Tsai, W.-H. Chung, Y.-S. Huang, and M.-V. Le, "A ceria layer as diffusion barrier between LAMOX and lanthanum strontium cobalt ferrite along with the impedance analysis," *Solid State Ionics*, Vol. 180, pp. 412-417, 2009.
79. Subramanian, P. R., "Ce-O Phase Diagram," in *Binary Alloy Phase Diagrams*, Massalski, T. D. (ed.), Materials Park, OH, 1990.
80. Mills, G., H. Jonsson, and G. K. Schenter, "Reversible work based transition state theory: Application to H₂ dissociative adsorption," *Surface Science*, Vol. 324, pp. 305-337, 1995.
81. Wang, S., A. Y. Borisevich, S. N. Rashkeev, M. V. Glazoff, K. Sohlberg, S. J. Pennycook, and S. T. Pantelides . "Dopants adsorbed as single atoms prevent degradation of catalysts," *Nature Materials*, Vol. 3, pp. 143-146, 2004.
82. Glazoff, M. V., S. N. Rashkeev, Y. P. Pyt'ev, J.- W. Yoon, and S. Sheu. "Interplay between plastic deformations and optical properties of metal surfaces: A multiscale study," *Applied Physics Letters*, Vol. 95, No. 8, p. 084106, 2009.